Thesis

The Development of the Faraday Tomography, and its Application to Probe Intergalactic Magnetic Fields

KOHEI KUMAZAKI

Division of Particle and Astrophysical Science

Graduate School of Science

Nagoya University

March 2015

Abstract

It is observationally known that there exist magnetic fields in galaxies and clusters of galaxies. The understanding of evolution mechanism is proceeding. For example, their strength and coherent length can be reproduced by numerical simulations although generation of seed magnetic fields is yet to be studied. On the other hand, until recently, there were very few observational clues of magnetic fields in the filamental structure of galaxy distribution and voids where galaxies are sparsely distributed. However, situation is drastically changing after recent claims of setting lower bounds $> 10^{-16}$Gauss on Inter-Galactic Magnetic Fields (IGMFs) from the non observation of lower energy gamma-rays from a high energy gamma ray source.

Now detection of IGMFs becomes an urgent and important task for modern cosmology and astrophysics. For example, attempts will be made by forthcoming large radio telescopes to detect synchrotron emission in order to reveal IGMFs. It is known that polarization is one of important probes of synchrotron radiation. The polarization plane rotates when radiation travel through the magneto-ionic media due to the Faraday rotation effect. The rotation angle depends on the strength of magnetic fields and wavelength of radiation. Therefore, a wide band observation allows us to investigate IGMFs. The Faraday tomography is a method by which we can estimate distribution of structure associated with magnetic fields on the line of sight. However, conventional radio telescopes could not cover wide frequency range which the Faraday tomography requires. Thus, the availability of the method was not examined very much. In this thesis, we construct a scheme utilizing the Faraday tomography that can be applied to newly built radio telescopes operating over a wide range of frequencies. Additionally, we propose strategies for exploring the cosmic magnetic fields by applying our scheme and verify its detectablity of the existence of magnetic fields associated with the filaments or voids by future radio telescopes.

First, we study a quality of Faraday tomography that is called the rotation measure (RM) ambiguity, whose mechanism was not revealed. The Faraday tomography possibly indicates false signals in some specific situation. We systematically investigate the condition of the appearance of such false signals. We consider observations of two sources in a single beam with various characters of sources, e.g., intensities, field orientation of sources and magnetic field strength in medium between sources. We find that false signals arise when the difference between the angles of rotated polarization of the far side source and the near side source is within $\sim \pm 10^{\circ}$. Moreover, we propose a new deconvolution method, in which we take the phase term into account. With this method, we can significantly

reduce this ambiguity.

Secondly, we discuss observational strategies to probe the IGMFs by means of Faraday tomography. Here we consider an observation of a single radio source such as a radio galaxy or a quasar, looking through the Galaxy. Our simulation with a simple model of sources suggests that cosmic magnetic fields with strength 1–3 rad m^{-2} in units of the Faraday rotation measure can be detected by future radio telescopes. Since IGMFs typically cause a few rad m^{-2} of the Faraday rotation according to theoretical and numerical studies, it is likely IGMFs to be detected by our scheme. Moreover, we evaluate whether IGMFs can be detected by not future but ongoing telescopes. Our analysis indicates that combination of ongoing telescopes can determine IGMFs with up to 3 rad m^{-2} if one observes a compact source with intensity of 20μJy.

Acknowledgment

First of all, I would like to express my sincere gratitude to my supervisor Naoshi Sugiyama for comprehensive discussions and insightful suggestions. Under his heartful and active tutelage over the past six years, I could touch a lots of interesting topics and broaden my outlook.

I am so greatful to my collaborators; Keitaro Takahashi at Kumamoto University and Takuya Akahori at Kagoshima University, for agressive monthly discussions. Whenever I encountered with some difficulties or obstacles, I could councel and start arguments without any hasitations. There is no doubt that I could not carry out my work and complete this thesis without them and their supports. Also, I wish to thank to all members of sub-science working group "cosmic magnetism" in SKA JP science working group. The incisive comments upgraged quality of my work and extensive discussions with experts in this field always realize me what a resercher should be.

I wish to thank to Saleem Zaroubi at Kapteyn Astronomical Institute and Sarod Yatawatta at ASTRON, Netherlands for giving me an oppotunity to study radio astronomy and techniques for radio observation as well as great hospitality. The stay in Netherlands with them is valuable experience for my life. I am so regretful that I could not contribute as they had hoped, in spite of their devoted supports.

I deeply thank to staff member in Cosmology laboratory, Takahiko Matsubara, Kiyotomo Ichiki, Chiaki Hikage, Hiroyuki Tashiro, Yuko Urakawa, Atsushi Nishizawa and Daisuke Nitta for constractive comments and advices in daily life. I received a lots of inspirations from their discussions and opinions. Also, I should thank to Shohei Aoyama and Yuri Fujii for impressive discussions about many science topics. This discussions always have motivated my research. Furthermore, I wish to thank to all menbers in Cosmology laboratory, Ω laboratory, TA laboratory, Kapteyn Astronomical Institute and Takahashi laboratory at Kumamoto University for daily thoughtfulness and great hospitality.

Finally, I would like to give my sincere gratitude to my family for supports and encouragements entire my life. They allow me to do everything I want with their courteous supports. It makes my decision to try for research life. Most importantly, I must acknowledge my wife Miki for her understanding and encouragement during the past few years. I became cheerful by her smile and love whenever she is around.

My work has been supported by Grants-in-Aid for Japan Society for the Promotion of Science (JSPS) Fellows for three years. Thanks to this support, I never concern about

financial issues in my research life. My work is also partialy supported by the JSPS Strategic Young Researcher Overseas Visits Program for Accelerating Brain Circulation from the Ministry of Education, Culture, Sports, Science and Technology (MEXT).

Contents

Chapter 1

Cosmic Magnetism

In recent years, the cold dark matter model with a cosmological constant, i.e., the ΛCDM model has been regarded as a standard model of cosmology. For the temperature fluctuations of the cosmic microwave background (CMB) radiation, theoretical predictions and all sky observations with high angular resolution by WMAP and PLANCK are remarkably matched. Moreover, a comparison of those makes it possible to determine cosmological parameters to describe evolution of the Universe with high precision [1, 2]. Large cosmological N-body simulations based on the ΛCDM model have been carried and succeeded to reproduce observed large scale structure (LSS) of the universe, e.g., [3]. It often says, therefore, that we are in the era of precision cosmology. However, there are still numerous open issues such as what are dark energy and dark matter, how the inflation in the early Universe can be directly probed, when the first stars and quasars are formed, and so on.

The magnetic field in the Universe can be also one of the main topics in the era of precision cosmology. Although existence of cosmic magnetic fields associated with astronomical objects of various scales, such as planets, stars, galaxies and clusters of galaxies, have been confirmed, their origin and detailed property are still unknown. There are two possibilities for the origin, astronomical or cosmological. One of the most famous astronomical mechanisms for generation of magnetic fields is the Biermann battery effect [4]. It is suggested that this mechanism can work in various systems, e.g. supernova explosions and star forming regions [5, 6], gamma–ray bursts [7], galaxy clusters [8], and LSS [9, 10, 11]. As for the cosmological origin, on the other hand, a lot of mechanisms are proposed, e.g., cosmic inflation with a term which breaks conformal invariance, second order density perturbations, phase transition, and so on [12, 13, 14], although non of them can succeed to produce strong enough magnetic fields.

Cosmological magnetic fields which pervade entire the Universe have not been detected so far. It may have affected to a number of processes in the history of the Universe (e.g. Ref. [15, 16]). For example, Tashiro and Sugiyama have investigated the influence of existence of cosmological magnetic fields on the reionization process of the intergalactic medium [15]. After recombination, additional density perturbations can be generated by cosmological magnetic fields due to the Lorentz force. These additional perturbations induce the structure formation at the mass scale $\leq 5.0 \times 10^6 \mathrm{M}_\odot$, which corresponds to

the Population Ⅲ star. Since the Population Ⅲ stars are considered as the main sources of reionization, existence of the cosmological magnetic fields leads early reionization. If the field strength is within 0.7-1.5nG, reionization process completes by $z \sim 15$. Another example is Rodrigues et al. in which they investigated the minimum baryonic mass that can accrete into dark matter halos [16]. It is believed that ultraviolet heating of the neutral interstellar gas is the main source of pressure based on semi-analytic models. They add the magneconvtic field as another important source of pressure. This additional pressure leads to less accretion of gas especially in smaller halos. Accordingly the formation of small galaxies is suppressed. Therefore earlier epochs of formation for low mass galaxies than the case without magnetic fields are required in order to assure enough accretion of gas onto galaxies. For example, they indicate that galaxies of $M \sim 5 \times 10^8 M_\odot$ need to form by $z \sim 2.2$ if the field strength is 1nG and the reionization epoch continues for $7 < z < 11$.

In this thesis, we focus on magnetic fields relevant to cosmology, i.e., magnetic fields associated with LSS or pervading the whole Universe, and discuss possible detection of them. Therefore we review observational and theoretical evidences of magnetic fields in LSS as well as observational constraints on cosmological magnetic fields in following sections.

1.1 Magnetic fields in the Large Scale Structure

The magnetic fields associated with the LSS of the Universe are referred as the intergalactic magnetic fields (IGMFs). The LSS is considered to have been formed via the hierarchical clustering process in the ΛCDM cosmology. In this process, small size objects collapse first, then grow through mergers with each other and eventually form large size objects. This scenario brings a picture of a multi phase intergalactic medium (IGM), hot and warm-hot medium. A hot medium has a temperature $T > 10^7$ K, which is observable by X–ray. Because this phase is found inside or around galaxy clusters, it is generally called the intercluster medium (ICM). On the other hand, a warm-hot medium has a temperature $T = 10^5$–10^7 K and distributes in a region between galaxy clusters, which is called a filament. The magnetic fields associated with these mediums could be a fossil of an origin of galactic magnetic fields.

1.1.1 Observational suggestions

Some evidences of existence of magnetic fields associated with the ICM are derived from observations of synchrotron emission, Faraday rotation measures and inverse Compton X-ray emission [17, 18]. The first discovery of diffuse synchrotron emission from a galaxy cluster was reported by Large et al. who observe the Coma cluster [19]. They estimated 2μG of the field strength with the assumption of energy equipartition [20]. After this discovery, the number of clusters with diffuse emission was increased by radio survey projects in various wavelength ranges [21, 22]. These surveys confirmed the existence of

magnetic fields in the LSS and provide the Faraday rotation measures. With Faraday rotation measure, we can obtain information of not only strength but also geometry of magnetic fields.

In radio halos, which is mainly located in a cluster, no polarized emission has been detected. The depolarization is caused by several mechanisms, e.g. mixture of thermal gas and relativistic plasma and/or disordered magnetic fields within a single observing beam. This fact could indicate existence of turbulent magnetic fields in ICM. In fact, a Kolmogorov-like spectrum in Abell 2382 and Coma cluster were reported [23, 24]. Exploring properties of the turbulent fields can lead hints of merger history of galaxies and galaxy clusters and origin of magnetic fields in clusters.

On the other hand, the magnetic fields in radio relics, which are diffuse synchrotron sources found in the peripheral regions of clusters, seem to act differently with the fields in radio halos. Highly polarized synchrotron emissions, such as several 10% of polarization degree, are observed from various radio relics [25, 26, 27, 28]. The direction of magnetic fields points along the long axis of relics and their strength lies within the range 0.5–2μG. Since the relics are believed to be formed by shocks due to cluster merger events [29, 30, 31], the magnetic fields could be generated or amplified at shock surface.

Unlike radio halos and relics, observations of synchrotron emission from outside of clusters are still sparse. Some authors claimed slight detection of radio emission between clusters [32, 33]. They concluded that what they found was a 'bridge' connecting both two clusters. They estimated 0.1–2.0μG of strength under the assumption of energy equipartition.

Some constraints on IGMFs are obtained from observations of ultrahigh energy cosmic rays (UHECRs) and very high energy (VHE) γ-rays [34, 35, 36, 37]. Charged UHECRs are deflected by magnetic fields during its propagation. This deflection leads to arrival time dispersion of UHECRs. The induced time delay for cosmic rays with 10^{20} eV energy, which is originated at 100 Mpc away, is estimated by Waxman and Miralda–Escudé [34] as

$$t_{\rm delay} \sim 50 \left(\frac{L}{100{\rm Mpc}} \right) \left(\frac{B}{5 \times 10^{-10}} \right)^2 \quad {\rm years}. \tag{1.1}$$

However, the origin of UHECRs is still an open problem. It could be local sources, or cosmological sources. If it turns out to be a cosmological origin, the time delay may become too long to be observed.

Recent progress of IGMF study is made in the use of observations of high energy gamma rays. Neronov and Vovk have reported a lower bound on the strength of the cosmological magnetic field. It is known that γ-rays with energy $E_{0\gamma}$ above TeV cannot travel over cosmological distance because of the interaction with infrared-UV photons in extragalactic background light. This interaction generates electron-positron pair and they emit secondary γ-rays via inverse Compton scattering with CMB photons. The secondary γ-rays have energy$\sim 88\,(\,E_{0\gamma}/10{\rm TeV}\,)^2$ GeV. If the magnetic fields exist, it deviates electron-positron trajectories then secondary γ-ray appears as extended emission around the source. The angle of extension is related with strength of the fields. Furthermore, the delay of secondary γ-ray causes spectral deviation (pair echo) [37]. A lower

bound estimated by analysis of High Energy Stereoscopic System (HESS) data is [36],

$$B \geq 3 \times 10^{-16} \quad \mathrm{G}, \tag{1.2}$$

which performs a good agreement with the result by the Major Atmospheric Gamma-ray Imaging Cherenkov (MAGIC) telescope [35]. Please note that this estimation is based on an uncertain assumption about continuous emission of γ-rays. The lower bound could be relaxed to $B \geq 10^{-18}$ G by employing a different model for the continuous emission [38]. Estimations from the pair echo suggested $B \geq 10^{-20}$ G [39, 40].

1.1.2 Theoretical suggestions

Observationally, the extended magnetic fields are shown in the clusters of galaxies. However it is unknown how the magnetic fields permeate the cluster while various diffusion processes have been proposed. The injection via galactic winds during a starburst phase of galaxies was considered in [41]. They assume 1μG magnetic fields in galaxies at the early starburst phase. Galactic winds extend to an intergalactic distance then re-compress by contraction of the cluster to the present size. This scenario can fill the ICM by the magnetic fields with 0.1μG which is consistent with estimation of X-ray and synchrotron emissions. The energy injection from black hole accretion disk, as well as turbulent motions caused by mergers of small objects, may also lead diffusion of magnetic fields [42, 43]. In [42], they estimated energy in radio robes of radio galaxies and found that 10-100 AGNs are needed in lifetime of the cluster in order to provide enough magnetic energy into ICM. In [43], the authors mainly argued how the magnetic fields in ICM have been maintained for long time >Gyr. Their scenario is as follows: (1) Fluctuation dynamo during cluster formation and major mergers produces μG level strength of magnetic fields. (2) Turbulence decays after the end of merger mergers. (3) Small mass sub-clusters and galaxies of the cluster produce turbulent wakes where magnetic fields were generated. They carried out MHD simulations and found 300 km s^{-1} turbulent speed, then 2μG strength of the fields are expected. These values correspond to 100-200 rad m^{-2} of Faraday rotation measure and are in good agreement with observations.

Ryu et al. proposed a scenario based on cosmological hydrodynamic simulations [44]. They found that turbulence is originated by cascade of vortices produced at cosmological shocks during the cluster formation epoch. External shocks form around the LSS by accretion of gases into a void region. Internal shocks are produced by infall of previously shocked gases and by chaotic flow motions or mergers of small size objects [45]. Then turbulence amplifies seed magnetic fields through three stages. (1)Exponential growth stage, (2) linear growth stage and (3) saturation stage. First stage is terminated when the back reaction effect becomes significant. During this stage, information of seed fields is disappeared. Thus evolution of magnetic fields does not depend on strength of the seed field if $> 10^{-20}$G. Turbulence also diffuses the magnetic fields to the LSS. The sub-sonic speed in the cluster or tran-sonic speed in the filament is enough to fill the magnetic fields in the LSS. They expect 1μG in ICM, 0.1μG around clusters and 10nG in filaments at present.

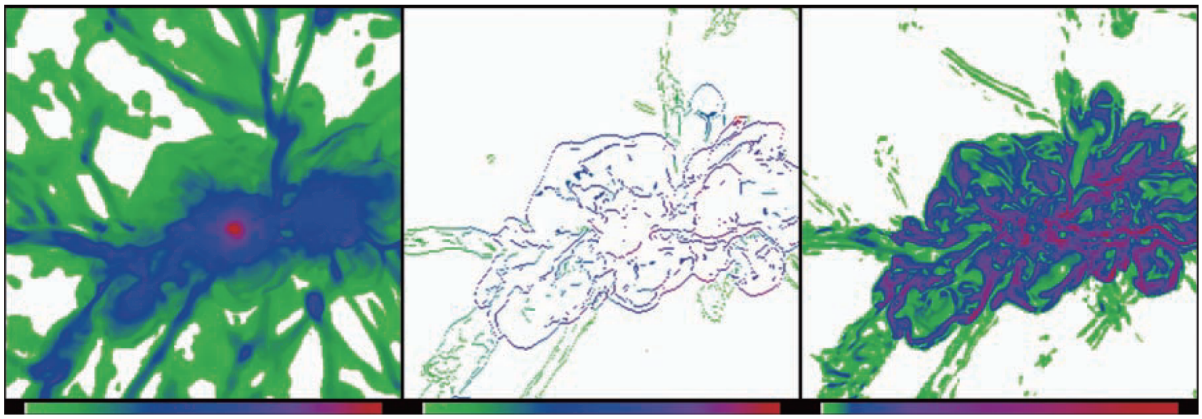

Figure 1.1: The gas density images(left panel), location of shocks (center) and magnitude of vorticity (right). This shows the existence of numerous shocks in the LSS and they closely match with the distribution of vorticity.

1.2 Cosmological Magnetic Fields

Generally speaking, cosmological magnetic fields are magnetic fields which are not associated with any virialized structure and whose coherent lengths can exceed the largest structure in the Universe. These magnetic fields are obviously the cosmological origin and can be generated before the epoch of structure formation, or even before the epoch of recombination or big bang nucleosynthesis (BBN). The existence of cosmological magnetic fields is, however, not confirmed by an observations so far. However, cosmological magnetic fields may play a significant role in structure formation of the Universe and possibly act as seed fields of galactic or intergalactic magnetic fields, if they exist. Therefore detection of cosmological magnetic fields is possibly crucial to understand structure formation and the origin of magnetic fields in the Universe while only upper bounds are obtained from cosmic microwave background and BBN as are shown below.

1.2.1 Observational constraints

A wide-spreading homogeneous or coherent magnetic field, i.e., a unidirectional field with spatially uniform strength, provides us a special direction parallel or orthogonal to the field. The influence of this effect on cosmic expansion is well studied by Madson ([46]). Since the expansion along the field stretches the field, which requires work against tension. Accordingly the expansion speed is slowed down. On the other hand, the expansion orthogonal to the field is speeded up by the magnetic pressure. Madsen obtained the constraint on the strength of cosmic magnetic fields from this effect on temperature fluctuations of CMB as

$$B \leq 2 \times 10^{-4} h \left(\frac{\delta\Omega}{1+z_d} \right)^{1/2} \quad \mathrm{G}, \tag{1.3}$$

where $\delta = \Delta T/T$ is temperature fluctuation, z_d is redshift at decoupling, Ω is cosmological density parameter and h is the Hubble parameter in unit of 75 km s^{-1} [46]. Barrow et al. took the cosmological evolution of the fields into account and derived a stronger upper limit from analysis of 4-year Cosmic Background Explore (COBE) data [47] as

$$B \leq 5 \times 10^{-9} h \sqrt{\Omega} \quad \text{G}. \tag{1.4}$$

Note that above constraints are given for the comoving value of the field strength. At the epoch of recombination $z_{\rm rec} = 1100$, the field strength is $(1 + z_{\rm rec})^2 = 1.2 \times 10^6$ larger than the comoving value.

The effect on BBN can also provide an upper bound for the field strength. BBN takes place between 10^{-2} to 200 sec after the big bang and generates light elements such as ^{2}H, ^{3}He, ^{4}He and ^{7}Li in the Universe. The match between theoretical prediction and observation constitutes one of the big successes of standard big bang cosmology. Since the existence of magnetic fields alters the theoretical prediction, limits can be set on their strength. O' Connell and Matese showed that the neutron should decay more rapidly in very strong magnetic fields $\geq 10^{13}$ G [48]. Reduction of the number of neutrons leads to decrease in light elements. Therefore magnetic fields should be limited by $\leq 10^{12}$ G at the epoch of BBN, which corresponds to $\leq 10^{-6}$ G at present (for the comoving value) [49, 50].

We can find an influence of cosmological magnetic fields not only in the early stage but later stage of the Universe. Polarized radio emission from the cosmological distance can be affected by cosmological magnetic fields due to Faraday rotation. Let us suppose existence of homogeneous electron and magnetic field distributions. In this case, all sky RM map contains dipole component along the cosmological magnetic field [51, 52, 53]. Vallée investigated this dipole from 309 galaxies and quasars [54]. He couldn't find any dipole signal and set an upper bound of 2 rad m^{-2} in RM out to $z \sim 3.6$, which corresponds to 6×10^{-12}G for 10^{-5} cm^{-3} of the thermal electron density.

1.3 Development of Radio Observatory

As we have shown above sections, observations of synchrotron emission and Faraday rotation in the radio band plays an important role for detection of magnetic fields in the Universe. We are expecting significant improvement of observations by ongoing and future radio telescopes such as Australian SKA Pathfinder (ASKAP), the South African Karoo Array Telescope (MeerKAT), Low Frequency Array (LOFAR), Murchison Widefield Array (MWA) and the Square Kilometre Array (SKA). In particular, SKA, which is planed to cover 10GHz - 70MHz and reaches 8 μJy beam^{-1} noise level with just 1 minute, is expected to probe numerous polarized sources by wide and deep survey. R. Beck and B. M. Gaensler have estimated the distribution of extragalactic source counts in both total intensity and linear polarization [55]. The left panels in Figure 1.2 show the number distribution of extragalactic sources as a function of source flux density at 1.4 GHz. The top panel plots the differential number distribution calculated using Ref. [56]. Solid and dashed line show the expected distribution of total intensity and linear polarization, respectively.

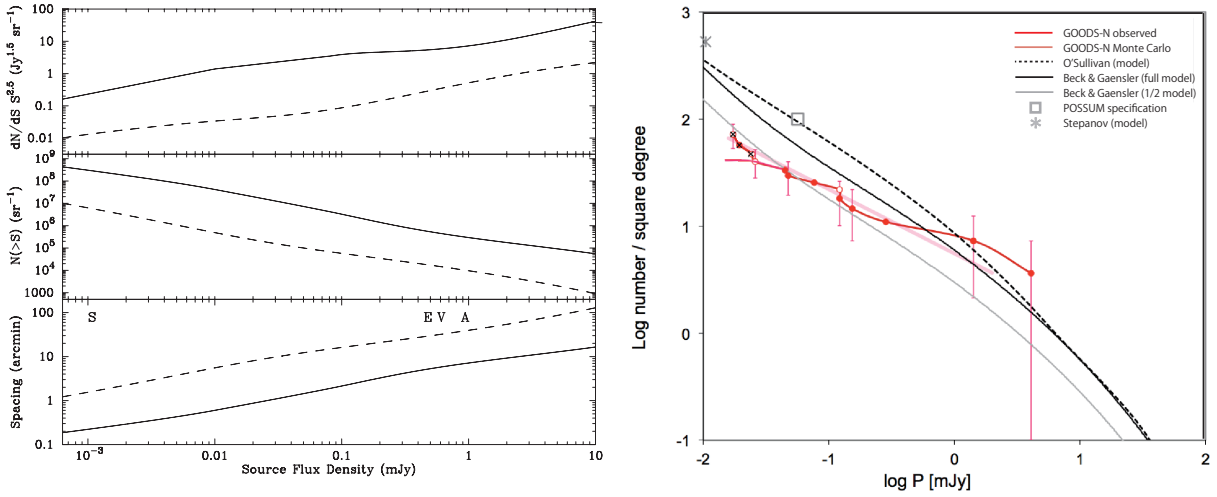

Figure 1.2: Left panels: Number distribution of extragalactic sources. Solid and dashed lines show the distribution of total intensity and linear polarization, respectively. The top and middle panel plots the differential number distribution and expected source density brighter than given flux (value of x-axis). The bottom panel indicates the averaged spacing between sources as a function of detectable flux. The symbols "A", "V", "E" and "S" show the typical detectable flux of linear polarized flux, for Australia Telescope Compact Array (ATCA), Very Large Array (VLA), Expanded VLA (EVLA) and SKA, respectively [55]. Right panel: Comparison between the number distributions of models and observations by the NRAO VLA Sky Survey [58].

The middle panel shows the expected number count of sources within 1 square degree which are brighter than the detection limit (value of x-axis). This value is evaluated by integration of top panel down to detection limit. This plot indicates that over 10 million polarized sources can be detected by SKA. Lower panel shows the mean angle separation between sources as a function of detectable flux. A source density of currently most extensive rotation measure map which contains 37,543 polarized sources is almost 1 per square degree [57]. This value was enough for probing structure of Galactic magnetic fields but insufficient for studies of even nearby galaxies. Almost 100 times dense source density by SKA enables us to investigate magnetic field structures in galaxies or galaxy clusters. Accordingly, we can start to study morphology of magnetic fields.

A comparison with the actual observation (NVSS) is shown in the right panel of Figure 1.2 [58]. The red line with points is the number count of detected sources in the GOODS-N field by NVSS. The black and gray lines plot the estimation of the full model and the 50% model of the left panels, respectively. The predicted number of polarized sources seems to be 2 or 3 times higher than the actual observation.

1.4 The motivation and outcomes of this thesis

In this thesis, we study the possibility of detecting IGMFs by ongoing and future radio telescopes and interferometers. The magnetic fields in the intergalactic medium are expected to contain information of primordial magnetic fields since they are not much processed in the history of the Universe. These information help us to understand the origin of ubiquitous magnetic fields associated with all astronomical objects and detailed history of structure formation in the Universe.

Based on these motivations, we develop a new method for exploring the cosmic magnetic field, which is called Faraday tomography and investigate the ability to measure the IGMF by this method.

First, we develop a systematic scheme utilizing Faraday tomography. Since no radio telescope has satisfied requirements of Faraday tomography so far, i.e., wide band radio observations, Faraday tomography has not been utilized so much. We first time study this method in great detail and evaluate systematics of the method. In particular, we find that reduction of both effects by incompleteness of observable wavelength range and ambiguity which generates false signal is essential for actual data processing [59].

Next, we investigate the ability of constructed scheme to explore the IGMF. We always suffer from the contribution of Galactic magnetic fields when we try to observe the magnetic fields outside the Galaxy. Therefore, we introduce two strategies which enable us to measure both the IGMF and the Galactic magnetic field [60]. Although both strategies require somewhat special systems, next generation radio telescopes can realize both strategies. Additionally, we investigate how well ongoing and future projects can constrain the strength of IGMF by utilizing the Fisher analysis [61].

1.5 Outline of this thesis

This thesis is organized as follows. We first introduce the physical phenomena associated with magnetic fields, synchrotron radiation and Faraday rotation in Chapter 2. In Chapter 3 and 4, we arrange the basic idea and strategy for applying Faraday tomography to real observations. Then we apply the Faraday tomography for exploring the IGMF to the pseudo observation then investigate the possibility of the measurement in Chapter 5. Finally, we devote pages to discussion and summary in Chapter 6 and 7.

Chapter 2

Observational methods

2.1 Synchrotron radiation

When a charged particle with relativistic velocity $\vec{v}$ moves in magnetic fields $\vec{B}$, it radiates an electromagnetic wave, which is called the synchrotron radiation. Cosmic rays (mainly electrons) which are accelerated by supernova remnants or jets from active galactic nuclei could be the origins. Since the synchrotron radiation provides us meaningful information of magnetic fields, it is very important to know its mechanism and properties.

We start from the equation of motion (EoM) for a charged particle at position $\vec{r}$ in magnetic fields. Introducing $\vec{\beta} = \vec{v}/c = (d\vec{r}/dt)/c$, EoM can be written as

$$\frac{d}{dt}(\gamma m_0 \vec{\beta}) = e(\vec{\beta} \times \vec{B}) \ , \tag{2.1}$$

where $\gamma \equiv (1-\beta^2)^{-1/2}$ is the Lorenz factor, m_0 is a rest mass of the particle and e is the electrical charge. Since charged particles always accelerate perpendicular to its motion, the left hand of the EoM can be rewritten by $\gamma m_0 \dot{\vec{\beta}}$. Dividing $\vec{\beta}$ into parallel $\vec{\beta}_{\parallel}$ and perpendicular component $\vec{\beta}_{\perp}$ to $\vec{B}$, EoMs for each component reduce to

$$\gamma m_0 \dot{\vec{\beta}}_{\parallel} = 0, \qquad \gamma m_0 \dot{\vec{\beta}}_{\perp} = e(\vec{\beta}_{\perp} \times \vec{B}) \ , \tag{2.2}$$

then they can be resolved as,

$$\frac{\vec{r}(t)}{c} = \frac{|\vec{\beta}|}{\omega_s} \left[\left(\vec{e}_x \cos(\omega_s t) + \vec{e}_y \sin(\omega_s t) \right) \sin\alpha + \vec{e}_z \omega_s t \cos\alpha \right] \ , \tag{2.3}$$

$$\vec{\beta}(t) = |\vec{\beta}| \left[\left(\vec{e}_x \sin(\omega_s t) + \vec{e}_y \cos(\omega_s t) \right) \sin\alpha + \vec{e}_z \cos\alpha \right] \ , \tag{2.4}$$

where α is the pitch angle between the magnetic field and the direction of motion of the charged particle, i.e. $\cos\alpha = (\vec{\beta} \cdot \vec{B})/(\beta B)$. $\vec{e}_{x,y,z}$ are unit vectors toward x, y and z axes (see in Figure 2.1), respectively. The EoMs indicates that the charged particle advances with constant velocity along the magnetic field and act the circular motion with angular

velocity $\omega_s = e\vec{\beta}_\perp B/\gamma m_0$ and radius $v_\perp/\omega_s$. The frequency ν_s, which is the number of rotation around the magnetic field per second, can be written with the angular frequency,

$$\nu_s = \frac{\omega_s}{2\pi} = \frac{1}{2\pi}\frac{eB}{\gamma m_0} \ . \tag{2.5}$$

The electric $\vec{E}_{\rm sync}$ and the magnetic field $\vec{B}_{\rm sync}$ radiated from the charged particle toward the observer during the time $dt = t_2 - t_1$ are given by

$$\vec{E}_{\rm sync} = \frac{e}{4\pi\varepsilon_0}\frac{\vec{n}\times[\,(\vec{n}-\vec{\beta})\times\dot{\vec{\beta}}\,]}{R(1-\vec{\beta}\cdot\vec{n})^3}, \quad \vec{B}_{\rm sync} = \frac{1}{c}\,\vec{n}\times\vec{E}_{\rm sync}, \tag{2.6}$$

where $\vec{n}$ is a unit vector toward observer and R is distance between the observer and the particle (see the left panel in Figure 2.1). Then, the average radiant energy flux density $\vec{I}$ in one rotation is

$$\vec{I} \ = \ \nu_s^{-1}\int_0^{1/\nu_s}\vec{S}dt = \frac{1}{\nu_s\mu_0}\int_0^{1/\nu_s}\vec{E}_{\rm sync}\times\vec{B}_{\rm sync}\,dt = \frac{\vec{n}}{c\nu_s\mu_0}\int_0^{1/\nu_s}|\vec{E}_{\rm sync}|^2\,dt \ , \tag{2.7}$$

where the radiant energy in unit time,

$$\frac{1}{c\nu_s\mu_0}|\vec{E}_{\rm sync}|^2 \ = \ \frac{1}{c\nu_s\mu_0}\frac{\dot{\beta}^2}{(1-\beta S)^3}\left(1-\frac{(1-\beta^2)\sin^2\theta\cos^2\phi}{(1-\beta S)^2}\right) \ , \tag{2.8}$$

$$S \ = \ \sin\alpha\sin\theta\sin\phi + \cos\alpha\cos\theta \ , \tag{2.9}$$

which shows strong directivity toward $\vec{\beta}$ as $\beta = v/c$ approaches to unity (see the right panel in Figure 2.1). The radiation from a charged particle consists of a superposition of harmonics of the fundamental frequency ν_s because it is acting a periodic motion. Therefore, frequency profile can be obtained by the Fourier transform. Then frequency profile of the total radiated energy from a charged particle can be derived by integration over the solid angle $d\Omega = \sin\theta d\theta d\phi$. There is no simple way to follow all derivations, so we just mention the results here (detail derivations are shown in Ref. [62]),

$$I(\nu) = \ I^+(\nu) \ + I^-(\nu) \tag{2.10}$$

$$I^\pm(\nu) \ = \frac{\sqrt{3}}{2}\mu_0 e^2 c\nu_s\sin\alpha F^\pm\left(\frac{2\gamma^2\nu}{3\nu_s\sin\alpha}\right) \tag{2.11}$$

$$F^\pm(x) \ = \frac{1}{2}x\left[\int_x^\infty K_{5/3}(\eta)d\eta \pm K_{2/3}(x)\right] \ , \tag{2.12}$$

where $K_j(x)$ is the modified Bessel function. The components $I^\pm$ correspond to contributions from the direction parallel or perpendicular to the projected magnetic field. The frequency profile is shown in the left panel of Figure 2.2.

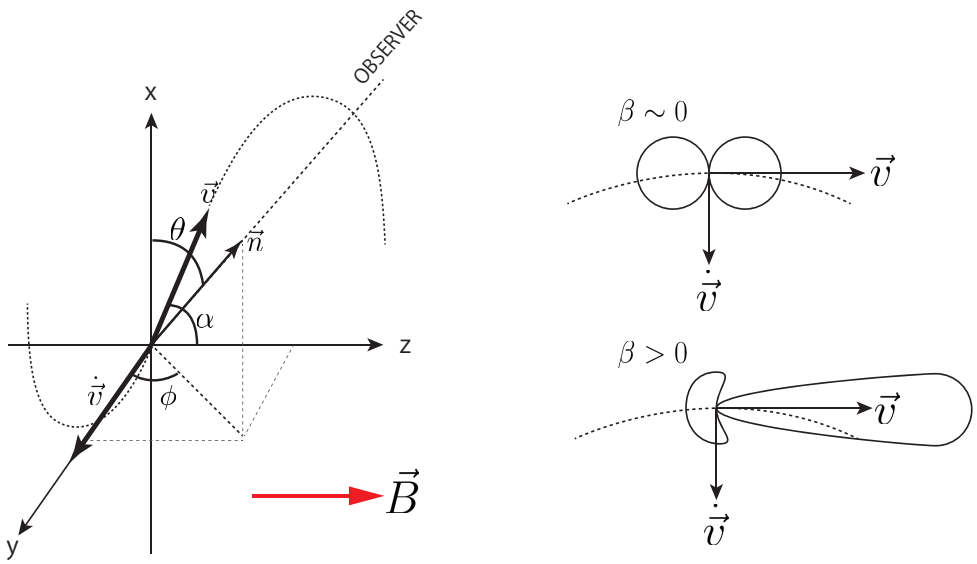

Figure 2.1: The directions of motion and magnetic field (the left panel) and the directivity of the radiant energy (the right panel).

Next, we consider the total synchrotron radiation from distributed charged particles. Assuming the power low energy distribution function for charged particles,

$$N(\varepsilon)d\varepsilon = N_0\varepsilon^{-p}d\varepsilon \quad \text{for} \quad \varepsilon_{\rm min} < \varepsilon < \varepsilon_{\rm max} \ , \tag{2.13}$$

the total emissivity can be written by

$$j(\nu)^{\pm} = \frac{1}{4\pi}\int_0^\infty N(\varepsilon)I^{\pm}(\nu)d\varepsilon \tag{2.14}$$

$$= \frac{N_0\mu e^2 c}{8\sqrt{2}}\left(\frac{3}{2}\right)^{p/2}\frac{(\nu_s\sin\alpha)^{(p+1)/2}}{\nu^{(p-1)/2}}\left[G^{\pm}\left(\frac{\nu}{\nu_{\rm min}}\right) - G^{\pm}\left(\frac{\nu}{\nu_{\rm max}}\right)\right] \ , \tag{2.15}$$

where

$$G^{\pm}(x) = \int_x^\infty \eta^{(p-3)/2}F^{\pm}(\eta)d\eta, \quad \nu_i = \frac{3}{2}\varepsilon_i^2\nu_s\sin\alpha \ (i = \min,\ \max). \tag{2.16}$$

In the simplest expression, it would be clear that the total emissivity of the synchrotron radiation reflects the strength of magnetic fields and the energy distribution of charged particles,

$$j(\nu) \propto C\, B^{(p+1)/2}\nu^{(p-1)/2}, \tag{2.17}$$

where C is a constant and $(p-1)/2$ is called the spectral index. Generally speaking, the emissivity becomes stronger at lower frequency range $\sim$ GHz, while it is defeated by the thermal emission from dusts at higher frequency, $\sim$ 100 GHz.

Additionally, the synchrotron radiation holds important property, which is the polarization. The polarization is yielded by differential of emissivity between parallel and

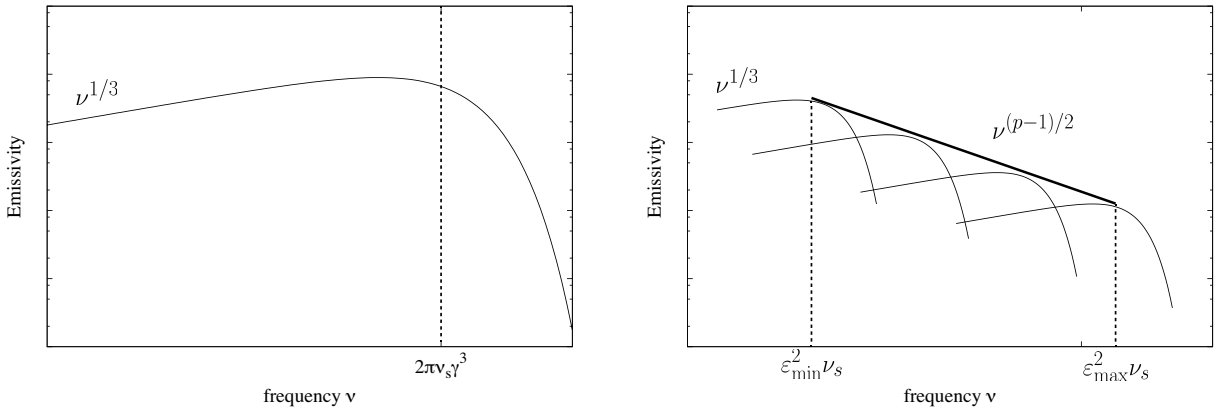

Figure 2.2: The frequency profiles of synchrotron radiation from a charged particle (left) and distributed charged particles (right).

perpendicular to the projected magnetic field as we saw at Equation (2.10). The component perpendicular to the magnetic field is stronger than parallel component. Therefore, the direction of polarization tells us the orientation of the magnetic field.

Generally speaking, we can observe the electric field vector $\mathbf{E} = (E_x, E_y)$ by arbitrary two orthogonal axes (see the left panel of Figure 2.3). Then, each component can be written by

$$E_x(t) = E_{0x}\cos(\omega t + \phi_x)\ , \quad E_y(t) = E_{0y}\sin(\omega t + \phi_y)\ , \tag{2.18}$$

where $\omega = 2\pi\nu$ is the angular frequency and $\phi_{x,y}$ are the phases at $t = 0$. Then, the electric field vector traces an ellipse over time. Introducing a new coordinate along the axes of a ellipse x' and y', the equation of the ellipse can be derived as

$$E_{x'}(t) = E_0\cos\beta\cos(\omega t)\ , \quad E_{y'}(t) = E_0\sin\beta\sin(\omega t)\ , \tag{2.19}$$

where β is an angle deriving the ratio between the major and minor axis of the ellipse, i.e. $\tan\beta = E_{0y'}/E_{0x'}$, and E_0 is an amplitude of the electric field vector. E_0, β and the tilt angle ψ uniquely determine the state of polarization. Deriving four parameters with observed parameters by arbitrary axes, i.e. E_{0x}, E_{0y}, ϕ_x and ϕ_y,

$$\begin{aligned} I &= E_{0x}^2 + E_{0y}^2 && (2.20)\\ Q &= E_{0x}^2 - E_{0y}^2 && (2.21)\\ U &= 2E_{0x}E_{0y}\cos(\phi_x - \phi_y) && (2.22)\\ V &= 2E_{0x}E_{0y}\sin(\phi_x - \phi_y)\ , && (2.23) \end{aligned}$$

E_0, β and ψ can be easily evaluated by

$$E_0 = \sqrt{I}, \quad \beta = \frac{1}{2}\arcsin\left(\frac{V}{I}\right) \quad \text{and} \quad \psi = \frac{1}{2}\arctan\left(\frac{U}{Q}\right). \tag{2.24}$$

I, Q, U and V are well known as Stokes parameters and can well describe the status of polarization (see the right panel of Figure 2.3). Using Stokes parameters, the degree of

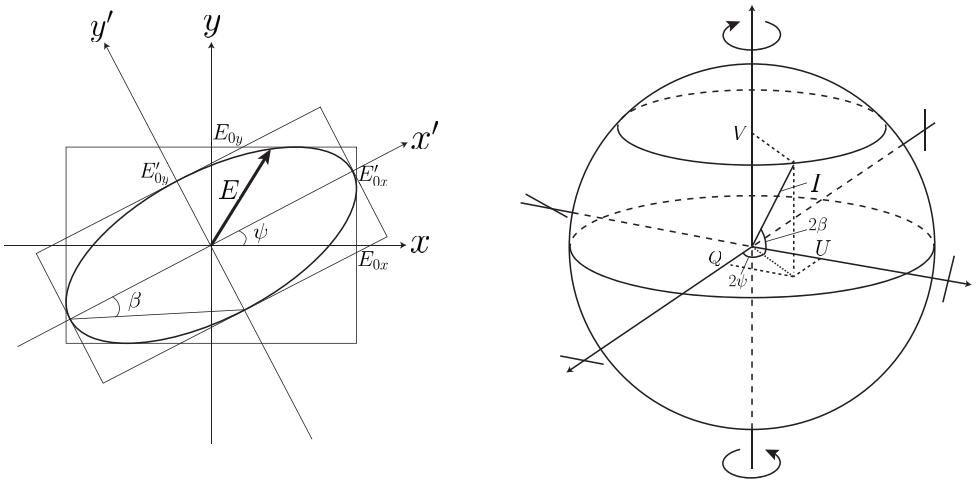

Figure 2.3: Schematic diagram of polarized electric field vector (left) and Poincare sphere (right).

polarization Π is defined as

$$\Pi \equiv \frac{\sqrt{Q^2 + U^2 + V^2}}{I} \ . \tag{2.25}$$

For the case of synchrotron radiation, degree of polarization becomes

$$\Pi = \frac{3p+3}{3p+7} \ . \tag{2.26}$$

2.2 Faraday Rotation

The Faraday rotation is well known as rotation of polarization planes when polarized emission travels thorough the magneto-ionic medium. We start from explanation of its mechanism for showing its property.

Let us consider the linear polarized emission $\vec{E}$ traveling in plasma associating with the uniform magnetic field $\vec{B} = (0, 0, B)$. Then the EoM for an electron located at $\vec{x} = (x, y, z)$ is

$$m_e \ddot{\vec{x}} = -e\left(\vec{E} + \frac{\dot{\vec{x}} \times \vec{B}}{c}\right) - \omega_{ep}^2 m_e \vec{x} \ , \tag{2.27}$$

where ω_{ep} is the plasma frequency and m_e is the electron mass. The first term on the right side is a term of Lorenz force and second is the restoring force by plasma oscillation which pulls the electron back in order to make plasma neutral when the electron moves

locally. Assuming ω for frequency of $\vec{E}$, Equation (2.27) can be solved

$$(\omega_{ep}^2 - \omega^2)x - i\Omega\omega y = -\frac{e}{m_e}E_x \tag{2.28}$$

$$(\omega_{ep}^2 - \omega^2)y + i\Omega\omega x = -\frac{e}{m_e}E_y \ , \tag{2.29}$$

where $\Omega = \frac{eB}{m_e c}$ is the cyclotron frequency. Using

$$E_\pm = E_x \pm iE_y \quad \text{and} \quad r_\pm = x \pm iy \ , \tag{2.30}$$

the solution in terms of $r_\pm$ can be written as

$$(\omega_{ep}^2 - \omega^2 - \Omega\omega)r_+ = -\frac{e}{m_e}E_+ \tag{2.31}$$

$$(\omega_{ep}^2 - \omega^2 + \Omega\omega)r_- = -\frac{e}{m_e}E_- \ . \tag{2.32}$$

The electric dipole moment $P_\pm = P_x \pm iP_y$ and the permittivity in the plasma $\varepsilon_\pm$ can be written by

$$P_\pm = -n_e e r_\pm = \frac{n_e e^2 E_\pm}{m_e(\omega_{ep}^2 - \omega^2 \mp \Omega\omega)} \tag{2.33}$$

$$\epsilon_\pm = 1 + \frac{P_\pm}{\epsilon_0 E_\pm} \tag{2.34}$$

$$= 1 + \frac{n_e e^2}{m_e\epsilon_0(\omega_{ep}^2 - \omega^2 \mp \Omega\omega)} \equiv \alpha_\pm^2 \ , \tag{2.35}$$

where ϵ_0 is the permittivity of vacuum. Finally, we follow the propagation of the polarized emission traveling through this plasma. From the wave equation, dispersion relation

$$k^2 = \alpha_\pm^2 c^{-2}\,\omega^2 \tag{2.36}$$

can be introduced. According to this relation, $\vec{E}$ can be divided into two components having different wavenumber. First component,

$$E_x^+ = E_0 \cos\left(\frac{\omega}{c}(\alpha_+ z - ct)\right), \ E_y^+ = E_0 \sin\left(\frac{\omega}{c}(\alpha_+ z - ct)\right) \ , \tag{2.37}$$

has refractive index α_+. It corresponds to the left hand circular polarization having phase velocity $\alpha_+\omega/c$. Another is

$$E_x^- = E_0 \cos\left(\frac{\omega}{c}(\alpha_- z - ct)\right), \ E_y^- = -E_0 \sin\left(\frac{\omega}{c}(\alpha_- z - ct)\right) \tag{2.38}$$

having refractive index α_- and corresponds to the right hand circular polarization with phase velocity $\alpha_-\omega/c$. Since the linear polarization is superposition of left and right hand circular polarizations, the propagating linear polarization becomes

$$E_x = 2E_0 \cos\left(\frac{\omega}{c}(\alpha z - ct)\right)\cos\left(\frac{\omega}{2c}(\alpha_+ - \alpha_-)z\right) \tag{2.39}$$

$$E_y = 2E_0 \cos\left(\frac{\omega}{c}(\alpha z - ct)\right)\sin\left(\frac{\omega}{2c}(\alpha_+ - \alpha_-)z\right) \ , \tag{2.40}$$

where $\alpha \equiv (\alpha_+ - \alpha_-)/2$. Looking at the polarization angle χ,

$$\chi = \frac{1}{2}\arctan\left(\frac{E_y}{E_x}\right) = \frac{\omega}{4c}(\alpha_+ - \alpha_-)z \ , \tag{2.41}$$

it is clear that the polarization angle is proportional to z. In a word, the polarization plane rotates as it propagates in magneto-ionic medium.

2.2.1 Rotation measure

Generally speaking, the frequency of the electromagnetic field and plasma frequency are adequately larger than the cyclotron frequency ($\omega \gg \omega_{ep} \gg \Omega$). Therefore, $\alpha_\pm$ can be approximately written as

$$\alpha_\pm \sim 1 + \frac{n_e e^2}{m_e \epsilon_0(\omega_{ep}^2 - \omega^2)} \pm \frac{n_e e^2 \omega \Omega}{2m_e \epsilon_0(\omega_{ep}^2 - \omega^2)^2} \ . \tag{2.42}$$

Then, the polarization angle per unit distance $d\chi/dz$ is described as

$$\frac{d\chi}{dz} = \frac{\omega}{2c}(\alpha_+ - \alpha_-) = \frac{n_e e^2 \omega^2 \Omega}{2cm_e \epsilon_0(\omega_{ep}^2 - \omega^2)^2} \ . \tag{2.43}$$

Furthermore, using $\omega \gg \omega_{ep}$ and $\omega = 2\pi c/\lambda$,

$$\frac{d\chi}{dz} = \frac{n_e e^3 B \lambda^2}{16\pi^2 m_e^2 c^4} \tag{2.44}$$

$$\Delta\chi = \frac{e^3 \lambda^2}{16\pi^2 m_e^2 c^4} \int_{LoS} n_e(z) B(z) dz \ . \tag{2.45}$$

It shows that the rotated angle is proportional to λ^2. The proportional coefficient is well known as the Rotation Measure (RM),

$$\mathrm{RM} \equiv \frac{e^3}{16\pi^2 m_e^2 c^4} \int_{LoS} n_e(z) B(z) dz \tag{2.46}$$

$$= 0.81 \int_{LoS} \frac{n_e(z)}{\mathrm{cm}^{-3}} \frac{B(z)}{\mu\mathrm{G}} \frac{dz}{\mathrm{pc}} \quad [\,\mathrm{rad\,m^{-2}}\,] \ . \tag{2.47}$$

The RM is commonly used as one of physical quantities containing information of magnetic fields on the LoS. It provides us just integrated magnetic fields multiplied by the thermal electron density. The information of magnetic fields can be estimated by combining with measurements of the dispersion measure (DM),

$$B \sim 1.232 \frac{\mathrm{RM}}{\mathrm{DM}} \, [\mu G] \ , \quad \text{for} \quad \mathrm{DM} = \int_{LoS} n_e(z) \frac{dz}{\mathrm{pc}} \ [\mathrm{cm}^{-3}] \ . \tag{2.48}$$

The RM is traditionally estimated as the slope of the observed polarization angle as a function of λ^2,

$$\chi(\lambda^2) = \frac{1}{2}\arctan\left(\frac{U(\lambda^2)}{Q(\lambda^2)}\right) = \chi_0 + \mathrm{RM}\,\lambda^2 \ , \tag{2.49}$$

where Q and U are the Stokes parameters and χ_0 is the intrinsic polarization angle.

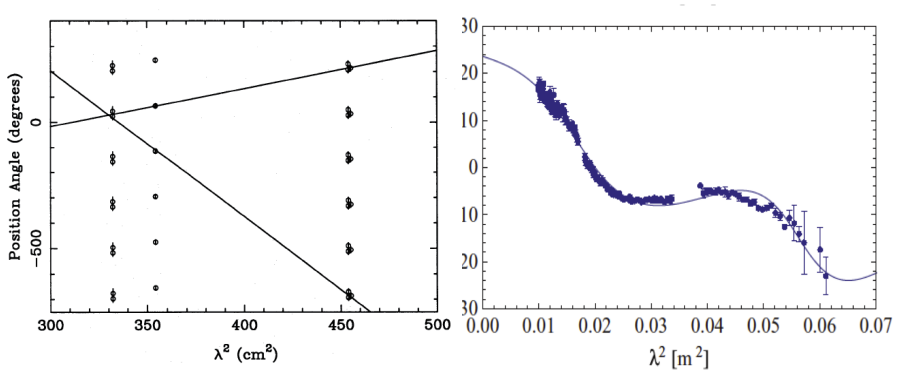

Figure 2.4: Left panel: Plots of the polarization angles as a function of λ^2 showing $n\pi$ ambiguity [63]. Right panel: the non-linear behavior of the polarization angle [65].

2.2.2 Difficulties of RM estimation

The estimation of RM from the slope of the polarization angle as a function of λ^2 is not straightforward. For instance, Rand and Lyne have encountered with various possible RMs for a pulsar observation (see left panel in Figure 2.4) [63]. It is well known as the $n\pi$ ambiguity, which is caused by the small number of data samples and large λ^2 separation. This ambiguity is normally solved by choice of RM which minimizes the mean square error between model and data. If various RMs provide the small mean square error, observations with other wavelength is needed.

Brentjens and de Bruyn have reported another problem. For the case of multiple sources or diffuse source on a LoS, the relationship between the polarization angle and λ^2 is not linear anymore [64]. Actually, O'Sullivan et al. have reported the non-linear behavior of the polarization angle by observations of AGNs (see the right panel in Figure 2.4), in which multiple regions emitting polarization are suggested [65]. It means that RM estimations by the linear fitting of the polarization angle can be reliable only the case with a single source on LoS, otherwise the estimated RM depends on the observed wavelength range.

Chapter 3

Faraday Tomography

In general, we only obtain the RM integrated over the LoS which can contain RM due to IGMF, extragalactic magnetic fields as well as GMF, $\mathrm{RM_{GMF}}$. Therefore, we always suffer with the huge $\mathrm{RM_{GMF}}$ whenever we observe outside of Galaxy. Moreover $\mathrm{RM_{GMF}}$ sometimes makes RM estimation difficult because it can cause the non-linear relation between the polarization angle and λ^2. We showed the inflexibility of linear fit RM estimation at previous section. Thus we need any other RM estimation method which can deal flexibly with various situations.

Burn (1966) has suggested a quantity which is called the Faraday dispersion function (FDF) for describing the Faraday rotation effect on the LoS [66]. The FDF allows us to depict the distribution of RM contributions on a LoS, although it is not real space distribution but RM–space distribution that we will show more detail in this Chapter. Ideally, we can divide RM into each component. In this chapter, we first show the derivation of FDF and its surroundings in detail. Then, we finally show the method by which we can estimate FDF from polarized intensity data.

3.1 Faraday dispersion function

Let us start from the observable complex polarization vector which can be written as the integration of the polarization along the LoS,

$$P(\lambda^2) \equiv Q(\lambda^2) + iU(\lambda^2) = \int_{\mathrm{LoS}} pI(z) e^{2i\chi(z,\lambda^2)} dz \ , \tag{3.1}$$

where p represents the polarization fraction, instead of Π in Section 2.1 and $I(z)$ is the intensity emitted at regions between $z \sim z + dz$. $\chi(z, \lambda^2) = \chi_0 + d\chi(z, \lambda^2)$ is the polarization angle, in which the first term is the intrinsic polarization angle and second term is the rotated angle due to Faraday rotation during propagation of polarization from position z to observer. The relation between the rotated angle and squared wavelength can be written by $d\chi(z, \lambda^2) = \phi(z)\lambda^2$. Here $\phi(z)$ resembles RM but integrated up to distance z,

$$\phi(z) = 0.81 \int_0^z \frac{n_e(z)}{\mathrm{cm^{-3}}} \frac{B(z)}{\mu\mathrm{G}} \frac{dz}{\mathrm{pc}} \quad [\,\mathrm{rad\,m^{-2}}\,] \ , \tag{3.2}$$

which is called Faraday depth. We will refer to this quantity in detail at next subsection. In order to easily understand a given expression, we use Faraday depth ϕ as a variable of integration in Equation (3.1) instead of distance z. Since the possible value for Faraday depth is from $-\infty$ to ∞, the polarization vector can be rewritten as

$$P(\lambda^2) = \int_{-\infty}^{\infty} pI(\phi)e^{2i(\chi_0+\phi\lambda^2)}d\phi \tag{3.3}$$

$$= \int_{-\infty}^{\infty} F(\phi)e^{2i\phi\lambda^2}d\phi \tag{3.4}$$

$$F(\phi) \equiv pI(\phi(z))e^{2i\chi_0} \ . \tag{3.5}$$

Here, the Faraday dispersion function $F(\phi)$ is defined. Please note that this quantity indicates the polarized flux distribution on the LoS as a function of Faraday depth ϕ. The FDF is the most important quantity to understand the discussion in this thesis. Therefore, we devote considerable space for explanation of the FDF.

3.1.1 Faraday depth and Faraday dispersion function

We start from the simplest case that a single radio emitter on the LoS. We describe the cartoon sketches of Faraday depth ϕ and FDF in Figure 3.1. At the left side, the schematic images of the LoS and the path of Faraday depth from observer to distance z are shown. At the right side, the simplified FDFs as a function of Faraday depth are shown.

If there is not any magnetized medium on the LoS (case (a), see (a) in Figure 3.1), the Faraday depth never changes along the LoS. Then the source would be appeared at $\phi = 0$ with amplitude corresponding to the source intensity integrated over observed frequency range. The intrinsic polarization angle can be estimated by

$$\chi_0 = \frac{1}{2}\arctan\left(\frac{\mathrm{Im}\left[F(\phi)\right]}{\mathrm{Re}\left[F(\phi)\right]}\right) \ . \tag{3.6}$$

In the case (b), we assume a magneto-ionic medium between the source and observer, (see (b) in Figure 3.1). White box shows the medium with thermal electrons, whose thermal electron density and physical size are n_e and L, respectively. Arrows above the white box represent the direction and strength of magnetic fields parallel to the LoS. Here strength is B_1. The blue color indicates the direction toward observer. Then, the Faraday depth increases as a function of z and finally it reaches

$$\phi = \phi_1 = K\int_{\text{near side}}^{\text{far side}} n_e B_1 dz = K n_e B_1 L, \quad K = 0.81 \tag{3.7}$$

under assuming the uniform distribution of thermal electron (see blue path with (1) in (b)), which corresponds to the total RM along the LoS. Thus, the FDF of the source is shifted to $\phi = \phi_1$ due to the RM due to the foreground magneto-ionic medium. If the magnetic fields in the foreground magneto-ionic medium point to opposite direction (the red arrow), the FDF is shifted to $\phi = -\phi_1$ (see red path with (2) in (b)).

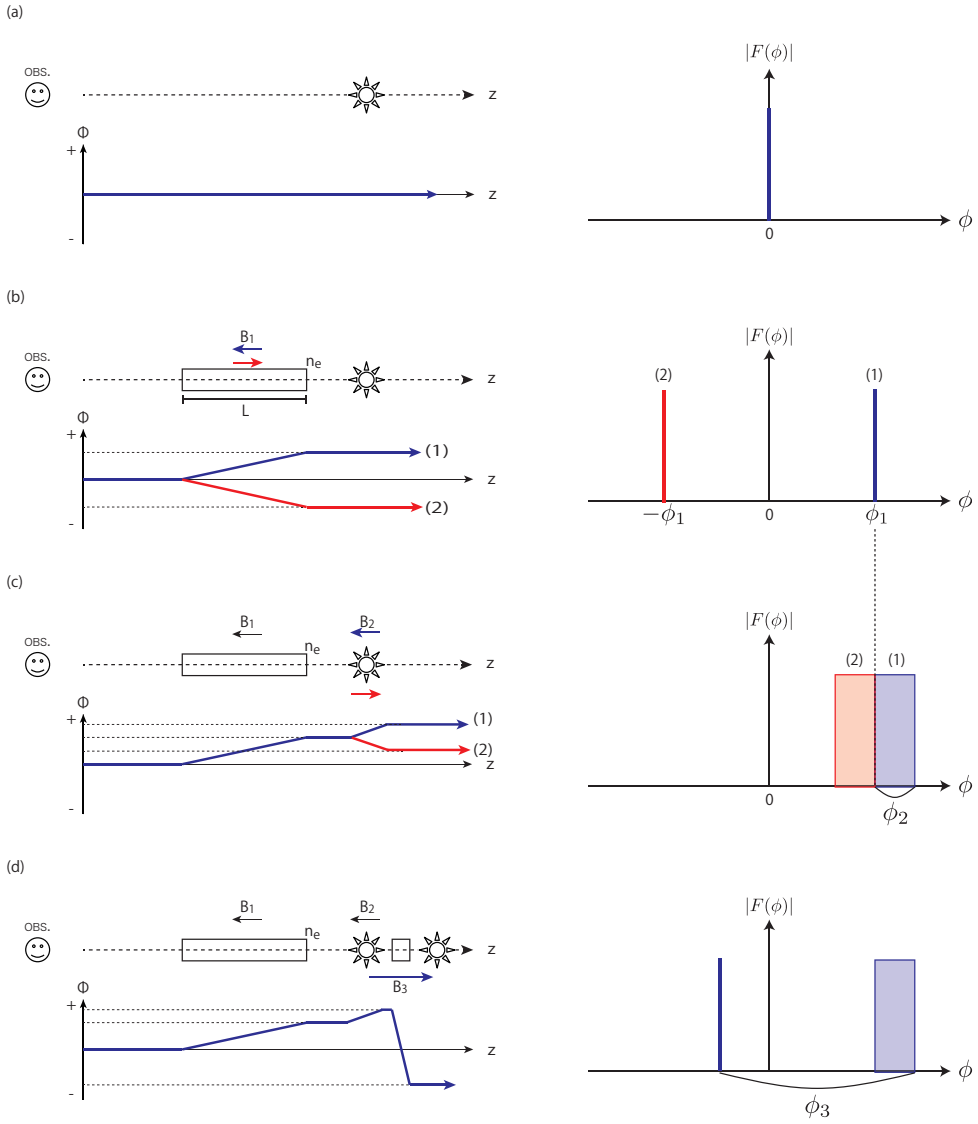

Figure 3.1: The cartoon sketch how the FDF is constructed. At left side, schematic image on the LoS and Faraday depth as a function of z. The arrow from a face shows LoS. White boxes represent the medium containing thermal electrons whose density is n_e. The arrows by objects display the direction and strength of magnetic fields associated with the object. Blue and red color just highlight the direction of magnetic fields, in order to help for tracing the Faraday depth path. At right side, the simplified FDF is shown.

Furthermore, we assume the magnetic fields in the radio emitter with strength B_2 (case (c), see (c) in Figure 3.1). As with case (b), the RM due to magneto-ionic medium reaches ϕ_1. From ϕ_1, the RM is accumulated more due to the magnetic fields in the radio emitter. Thus the total RM along the LoS would be $\phi_1 + \phi_2$ where $\phi_2 = Kn_eB_2d$, where d is the physical size of the radio emitter. The effect of ϕ_2 is seen as thickness of the FDF because the Faraday depth does change at inside of radio emitter. The FDF having thickness in the Faraday depth space is called **Faraday thick source**, otherwise **Faraday thin source**. Generally speaking, polarized radio emitters associating with magnetic fields and thermal electron are shown as Faraday thick source. Although we represent the Faraday thick source like top hat function here, the feature of the Faraday thick source depends on the geometry of the emitter and property of magnetic fields. The simple models are shown in Section 3.2.2 and models based on numerical simulation will be discussed in Chapter 6.

Finally, we assume a little complex case that two radio emitters exist on a LoS (case (d), see (d) in Figure 3.1). Between two emitters, the magneto-ionic medium with strong magnetic fields are assumed, whose strength is B_3. Then the Faraday depth would be $\phi_3 = Kn_eB_3l$, where l is the physical size of the medium. Due to the effect of this medium, the further emitter can be seen away from the nearer source. This separation of the emitters is the most important benefit for using FDF, because the FDF allow us to obtain RMs of each component on the LoS. For example, ϕ_3 corresponding to the RMs between radio emitters can be estimated from distance between FDFs in the Faraday depth space. Also, ϕ_2 corresponding to the RMs of inside of nearer radio emitter can be estimated from thickness of FDF. The matter is how the FDF can be reconstructed from the observed polarization vector.

3.2 Model fitting

One of the simplest methods for FDF reconstruction is to make some models and find best fit parameters in these models. This method is widely used [65, 67, 68] and provides relatively robust results (performance will be shown at Section A.4). However, it should be noticed that one should know the distribution of magnetic fields and thermal electron and geometry of the source or correct model function describing FDF. In this subsection, we introduce polarization vectors for various types of FDF for understanding the behavior and its dependence on model.

3.2.1 Faraday thin source

The FDF written by Dirac delta function is one of the simplest model and only the way to describe the Faraday thin source.

$$F(\phi) = F_0\delta(\phi - \phi_s)e^{2i\chi_0} \ , \tag{3.8}$$

where F_0, ϕ_s and χ_0 represent the intensity, Faraday depth and the intrinsic polarization angle of source, respectively. Nonetheless, this model well describes quasars or some

extragalactic radio sources. Under this FDF, the Stokes Q and U behave oscillating function as a function of λ^2,

$$P(\lambda^2) = Q(\lambda^2) + iU(\lambda^2) = F_0 e^{2i(\chi_0 + \phi_s \lambda^2)} \ , \tag{3.9}$$

for the case of single source. The frequency of $Q(\lambda^2)$ and $U(\lambda^2)$ corresponds to the Faraday depth of source ϕ_s. Then, polarization intensity $P(\lambda^2)$ will take constant value along λ^2. It means that this type of FDF can be detected at any wavelength ranges.

3.2.2 Faraday thick source

Next, we mention about Faraday thick source, which has thickness in Faraday depth domain. Unlike Faraday thin source, numerous types of function can be considered and they perform unique behavior. Here, we just introduce simple functions which are commonly used or discussed in previous works.

Uniform slab screen

The simplest function is the top hat function,

$$F(\phi) = \begin{cases} (2\phi_w)^{-1} e^{2i\chi_0} & \text{for} \quad -\phi_w \leq \phi \leq \phi_w \\ 0 & \text{for} \quad \text{otherwise} \end{cases} \ . \tag{3.10}$$

Then the polarized intensity can be led to

$$\begin{aligned} P(\lambda^2) &= \int_{-\phi_w}^{\phi_w} (2\phi_w)^{-1} e^{2i\chi_0} e^{2i\phi\lambda^2} d\phi \\ &= \frac{1}{4\phi_w \lambda^2} \left[e^{2i\phi_w\lambda^2} - e^{-2i\phi_w\lambda^2} \right] e^{2i\chi_0} \\ &= \frac{\sin(2\phi_w\lambda^2)}{2\phi_w\lambda^2} e^{2i\chi_0} \ . \end{aligned} \tag{3.11}$$

This type of FDF is well known as Burn's slab [66]. The behavior and dependence on thickness can be seen in the left panels of Figure. 3.2. Top and bottom panel show the FDF and the polarized intensity, respectively. The most important behavior is attenuation of the polarized intensity at long wavelength. It is caused by the Faraday depolarization which we will discuss in next section.

Uniform sphere function

It seems to be more realistic assumption that the source does not have sharp cut off at its edges. A uniform sphere function with radius ϕ_w, which is represented by

$$F(\phi) = \begin{cases} \frac{3}{2\phi_w} \left[1 - \left(\frac{\phi}{\phi_w} \right)^2 \right] e^{2i\chi_0} & \text{for} \quad -\phi_w \leq \phi \leq \phi_w \\ 0 & \text{for} \quad \text{otherwise} \end{cases} \ , \tag{3.12}$$

is one of the suitable functions. Then, the polarization intensity can be analytically written as

$$\begin{aligned} P(\lambda^2) &= \int_{-\phi_w}^{\phi_w} \frac{3}{2\phi_w}\left[1-\left(\frac{\phi}{\phi_w}\right)^2\right] e^{2i\chi_0} e^{2i\phi\lambda^2} d\phi \\ &= 3\int_{-\phi_w}^{\phi_w} (2\phi_w)^{-1} e^{2i\chi_0} e^{2i\phi\lambda^2} d\phi - \int_{-\phi_w}^{\phi_w} \frac{3}{2\phi_w^{-3}} \phi^2 e^{2i\chi_0} e^{2i\phi\lambda^2} d\phi \\ &= \frac{3}{2\phi_w^{-3}} \int_{-\phi_w}^{\phi_w} \frac{\phi}{i\lambda^2} e^{2i\phi\lambda^2} d\phi \\ &= \frac{3}{2\phi_w}\left[\frac{\sin(2\phi_w\lambda^2)}{2\phi_w^2\lambda^6} - \frac{\cos(2\phi_w\lambda^2)}{\phi_w\lambda^4}\right] e^{2i\chi_0} \ . \end{aligned} \tag{3.13}$$

Gaussian function

It is also relatively realistic assumption that the source can be described by Gaussian function with variance ϕ_w,

$$F(\phi) = \frac{1}{\sqrt{2\pi}\phi_w} \exp\left(-\frac{\phi^2}{2\phi_w^2}\right) e^{2i\chi_0} \ . \tag{3.14}$$

Then,

$$\begin{aligned} P(\lambda^2) &= \int_{-\infty}^{\infty} \frac{1}{\sqrt{2\pi}\phi_w} \exp\left(-\frac{\phi^2}{2\phi_w^2}\right) e^{2i\phi\lambda^2} e^{2i\chi_0} d\phi \\ &= e^{2\phi_w^2\lambda^4} e^{2i\chi_0} \int_{-\infty}^{\infty} \frac{1}{\sqrt{2\pi}\phi_w} \exp\left[-\frac{(\phi - 2i\phi_w^2\lambda^2)^2}{2\phi_w^2}\right] d\phi \\ &= e^{-2\phi_w^2\lambda^4} e^{2i\chi_0} \ . \end{aligned} \tag{3.15}$$

3.3 Depolarization

As we have shown in Figure 3.2, the polarized intensity is obviously reduced with wavelength for the case of Faraday thick source, which is called depolarization commonly. In this case, the depolarization scale depends on the thickness of FDF. Hence the behavior of depolarization can be utilized for understanding the properties of source. Simply speaking, depolarization is caused by blending polarization planes which have different polarization angles. Various mechanisms which provide different polarization angles can be considered (e.g. turbulent magnetic fields inside/outside of sources or instrumental problems). In this section, we refer to some depolarization mechanisms which are worthy to be mentioned. Hereafter, we assume that the magnetic fields $\mathbf{B} = (B_x, B_y, B_z)$ consist of two

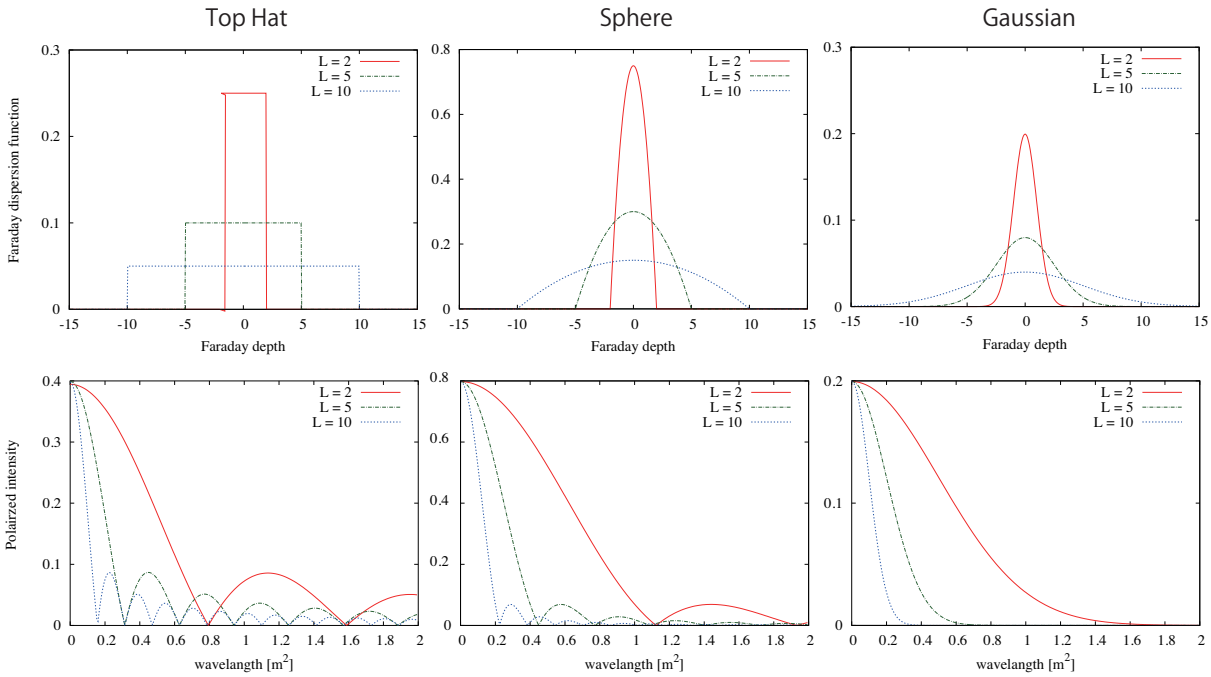

Figure 3.2: The polarized intensities as a function of λ^2 (bottom panels) with various parameters describing thickness of FDF (top panel), $L = \phi_w$=1.0 (red), 5.0 (green) and 10.0 (blue).

components, regular $\mathbf{B}^0 = (B^0_x, B^0_y, B^0_z)$ and turbulent magnetic fields $\mathbf{B}' = (B'_x, B'_y, B'_z)$,

$$\mathbf{B} = \mathbf{B}^0 + \mathbf{B}' \ . \tag{3.16}$$

The statistical quantities are $\langle B_i \rangle = B^0_i$ and $\langle B^2_i \rangle = {B^0_i}^2 + \sigma^2_i$ where σ_i is the standard deviation of B'_i and $\langle \ldots \rangle$ represent the average over the source.

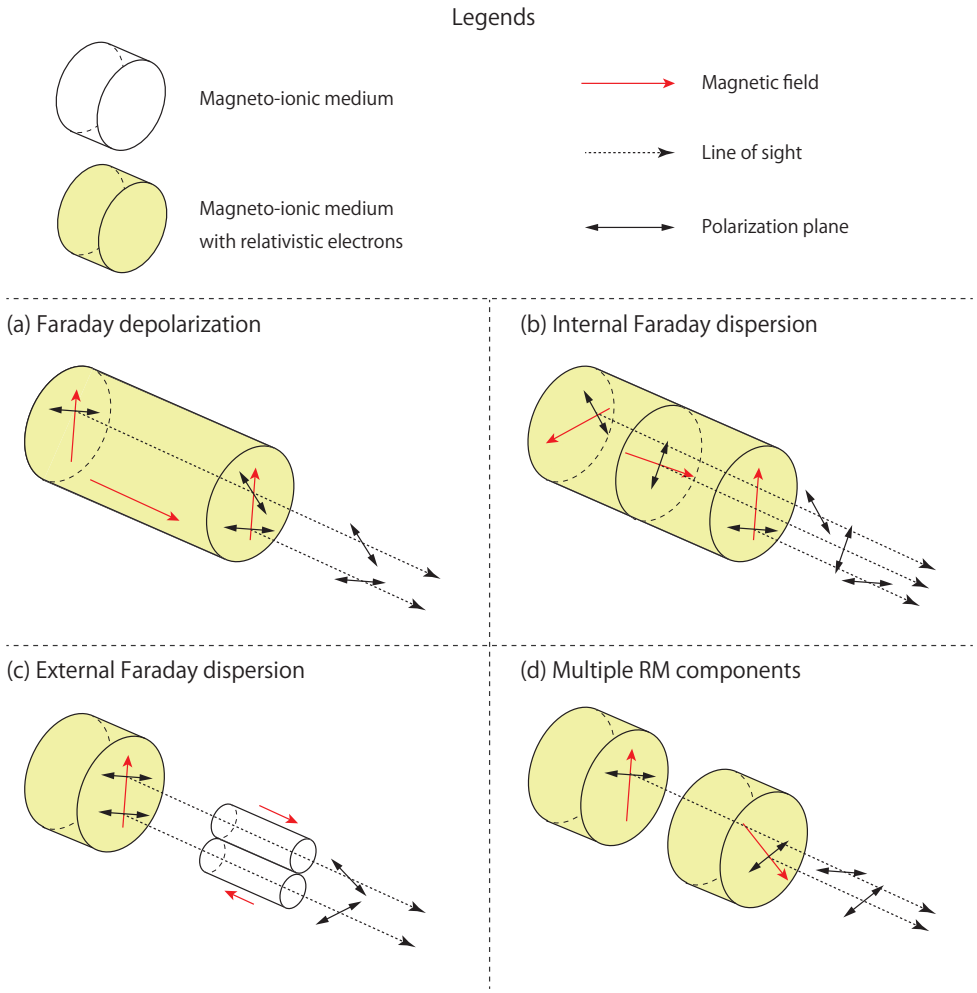

Figure 3.3: Sketches of depolarization mechanisms. (a) Faraday depolarization, (b) internal Faraday dispersion, (c) external Faraday dispersion and (d) Multiple RM components. A legend in sketches is shown above.

3.3.1 Faraday depolarization

We start from the Faraday depolarization which can be seen in Fig. 3.2. This is also called differential Faraday rotation (DFR). When the source emitting synchrotron radiation is surrounding by magneto-ionic medium, the polarization plane emitted at deeper region rotates by Faraday effect in the source. After observing the integrated polarization angles from surface to far side of the source, the degree of polarization would be reduced (see (a) in Figure 3.3). Since the longer wavelength is strongly affected by Faraday effect, the Faraday depolarization would be serious at longer wavelength. For the case of Burn's slab, the behavior of polarization intensity can be written by sinc function (see Equation (3.11)) which would be zero at $\phi_w \lambda^2 = n\pi/2$ for $n = 1, 2, \ldots$. For $0 < \phi_w \lambda^2 < \pi/2$, the

polarization plane from far side of the source rotates less than 180 degrees, thus the blended polarization planes partially cancel out each other. At $\phi_w \lambda^2 = \pi$ the polarization plane rotates just 180 degrees, then blended polarization planes completely cancel out. Please note that the Faraday depolarization does keep the linear relation between the polarization angle and squared wavelength. That means that rotation measure averaged over the source can be estimated by $d\chi(\lambda^2)/d\lambda^2$ at any wavelength.

3.3.2 Internal Faraday dispersion

The turbulent magnetic fields yield the depolarization, which is called Faraday dispersion. The intrinsic polarization angle is perpendicular to direction of projected magnetic fields,

$$\chi_0(z) = \frac{\pi}{2} + \arctan \frac{B_y(z)}{B_x(z)} \ , \tag{3.17}$$

and rotates by magnetic fields toward us. Thus, if the turbulent magnetic fields exist in emitter, the intrinsic polarization angle is determined randomly then blended each other. This fact leads depolarization, especially it is called internal Faraday dispersion (IFD) (see (b) in Figure 3.3). The polarization angle is simply random when the number of cells accumulated on the LoS is small, but otherwise, we can predict the properties of polarized intensity under some assumptions.

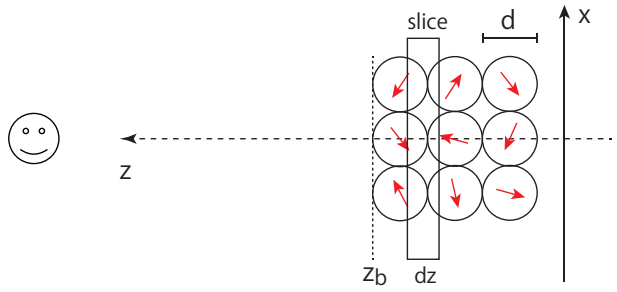

Figure 3.4: Schematic description of turbulent cell in a source.

The observed polarized intensity would be the sum of contributions from all slices. The contribution of each slice is an average of polarization intensities in each cell in the slice. Here the size of cell corresponds to coherent length of turbulent magnetic fields d, i.e.

$$P(\lambda^2) = p \int_{\text{slice}} \left\langle I(\vec{x}) e^{2i(\chi_0(\vec{x}) + \phi(\vec{x})\lambda^2} \right\rangle_{\text{slice}} dz \ , \tag{3.18}$$

where x and z are coordinates projected on the sky and along the LoS, respectively (see Figure 3.4). $\langle \ldots \rangle_{\text{slice}}$ represents an average over the slice. The Faraday depth at point $\vec{x} = (x, y, z)$ can be written by $\phi(\vec{x}) = 0.81 \int_z^{z_b} n_e(\vec{x}) B_z(\vec{x}) dz$, where z_b is the point of closest cell. We set $z = 0$ at the point of deepest call, then z_b corresponds to the size of source. It is convenient to separate intrinsic polarized intensity term as P_0. This division

can be done because $B_\perp$ and $B_\parallel$ do not have correlation which are related with χ_0 and ϕ, respectively. If they are correlated each other, the magnetic field is solenoidal. We believe that the effect is not significant [69]. Then, $P(\lambda^2)$ reduces to

$$P(\lambda^2) = \int P_0 \left\langle I(\vec{x}) \right\rangle_{\rm slice} \left\langle e^{2i\phi(\vec{x})\lambda^2} \right\rangle_{\rm slice} dz, \quad P_0 = p \frac{\left\langle I(\vec{x}) e^{2i\chi_0} \right\rangle_{\rm slice}}{\left\langle I(\vec{x}) \right\rangle_{\rm slice}} \ . \tag{3.19}$$

Substituting Equation (3.17) to P_0, the intrinsic polarized intensity can be written by

$$\begin{aligned} P_0 &= \frac{p}{\langle B_\perp^2 \rangle_{\rm slice}} \left\langle B_\perp^2 \exp\left[2i \left(\frac{\pi}{2} + \arctan \frac{B_y(z)}{B_x(z)} \right) \right] \right\rangle_{\rm slice} \\ &= \frac{p}{\langle B_\perp^2 \rangle_{\rm slice}} \left\langle B_\perp^2 \left(\frac{B_x}{B_\perp} + i \frac{B_y}{B_\perp} \right)^2 \right\rangle_{\rm slice} \\ &= p \frac{\left\langle B_x^2 - B_y^2 + 2i B_x B_y \right\rangle_{\rm slice}}{\langle B_\perp^2 \rangle_{\rm slice}} \\ &= P_{\rm IFD} e^{2i\chi_0^{\rm IFD}}. \end{aligned} \tag{3.20}$$

where

$$P_{\rm IFD} = p \frac{\sqrt{(B_x^{0\,2} - B_y^{0\,2} + \sigma_x^2 - \sigma_y^2)^2 + 4\langle B_x \rangle^2 \langle B_y \rangle^2}}{\langle B_\perp^2 \rangle} \tag{3.21}$$

$$\chi_0^{\rm IFD} = \frac{\pi}{2} + \frac{1}{2} \arctan \left(\frac{2\langle B_x B_y \rangle}{B_x^{0\,2} - B_y^{0\,2} + \sigma_x^2 - \sigma_y^2} \right) \ . \tag{3.22}$$

Assuming isotropic turbulence, i.e. $\sigma_x \sim \sigma_y \sim \sigma$, Equation (3.21) gives a simple result

$$P_{\rm IFD} = p \frac{B_\perp^{0\,2}}{B_\perp^{0\,2} + 2\sigma^2} \ . \tag{3.23}$$

This result clearly shows that the intrinsic polarization intensity P_0 is weakened by strong turbulent magnetic fields and this depolarization does not depend on wavelength. Thus, it also called *wavelength independent depolarization*. However, in many cases, IFD occurs with Faraday depolarization due to B_z' even if regular magnetic fields do not exist. It brings the dependency on wavelength. In order to derive the Faraday depolarization effect by turbulent magnetic fields, we next focus on the rotation term. For simplification, equal emissivity in entire the source $I(\vec{x}) = I$ and homogeneous electron density distribution $n_e(\vec{x}) = n_e$ are assumed. The Faraday depth $\phi(\vec{x})$ also contains of the regular part

$$\phi^0(\vec{x}) = \int_z^{z_b} K n_e B_z^0 dz \ , \tag{3.24}$$

and the turbulent part

$$\phi'(\vec{x}) = \int_z^{z_b} K n_e B'_z(\vec{x}) dz \ . \tag{3.25}$$

Then Equation (3.19) reduces to

$$P(\lambda^2) = \int P_0 I(\vec{x}) e^{2i \int_{z'}^{z_b} K n_e B_z^0 dz' \lambda^2} \langle e^{2i\phi'(\vec{x})\lambda^2} \rangle_{\text{slice}} \, dz. \tag{3.26}$$

If numerous number of cells are contained in a slice, the probability density function of $2\phi'(\vec{x})\lambda^2$ will be approximately Gaussian distribution function by central limit theorem. The variance $\sigma^2_{\phi'}$ is derived by

$$\begin{aligned} \sigma^2_{\phi'} &= \left\langle (2\phi(\vec{x})\lambda^2)\,(2\phi(\vec{x}')\lambda^2) \right\rangle \\ &= \iint_z^{z_b} 4K^2 n_e^2 \lambda^4 \left\langle B'(\vec{x}) B'(\vec{x}') \right\rangle dz\, dz' \ . \end{aligned} \tag{3.27}$$

Fixing z, $\langle B'(\vec{x})B'(\vec{x}')\rangle$ has a value $\langle {B'_z}^2 \rangle = \sigma_z^2$ when $|z' - z|$ is smaller than coherent length of turbulent fields d, otherwise zero because $B'(\vec{x})$ varies randomly at outside of cell. Then, Equation (3.27) reduces to

$$\sigma^2_{\phi'} = 4\lambda^4 K^2 n_e^2 \int_{z'}^{z_b} \sigma_z^2 d \, dz' \ . \tag{3.28}$$

The expected value of $\langle e^{2i\phi'(\vec{x})\lambda^2} \rangle$ can be estimated with this probability distribution function, introducing $X = 2\phi'(\vec{x})\lambda^2$,

$$\langle e^{2i\phi'(\vec{x})\lambda^2} \rangle = \int_{-\infty}^{\infty} e^{iX} \exp\left(-\frac{X^2}{2\sigma^2_{\phi'}} \right) dX = \exp\left(-\frac{\sigma^2_{\phi'}}{2} \right) \ . \tag{3.29}$$

Finally, substituting Equation (3.29) to (3.26), the polarization intensity can be led as

$$\begin{aligned} P(\lambda^2) &= P_0 I \int_0^{z_b} \exp\left(2i\lambda^2 \int_z^{z_b} K n_e B_z^0 dz' - 2\lambda^4 K^2 n_e^2 \int_z^{z_b} \sigma_z^2 d \, dz' \right) dz \\ &= P_0 I \int_0^{z_b} \exp\left[(2iK n_e B_z^0 \lambda^2 - 2K^2 n_e^2 \sigma_z^2 d \, \lambda^4)(z_b - z) \right] dz \\ &= P_0 I \, \frac{1 - e^{-S}}{S} \ , \end{aligned} \tag{3.30}$$

where $S = 2K^2 n_e^2 \sigma^2_{\phi'} d \, \lambda^4 z_b - 2iK n_e B_z^0 \lambda^2 z_b$.

3.3.3 External Faraday dispersion

Only the case with larger beam size than coherent scale of the fields , turbulent fields in non-emitting magneto-ionic medium in front of emitter can be a cause of depolarization.

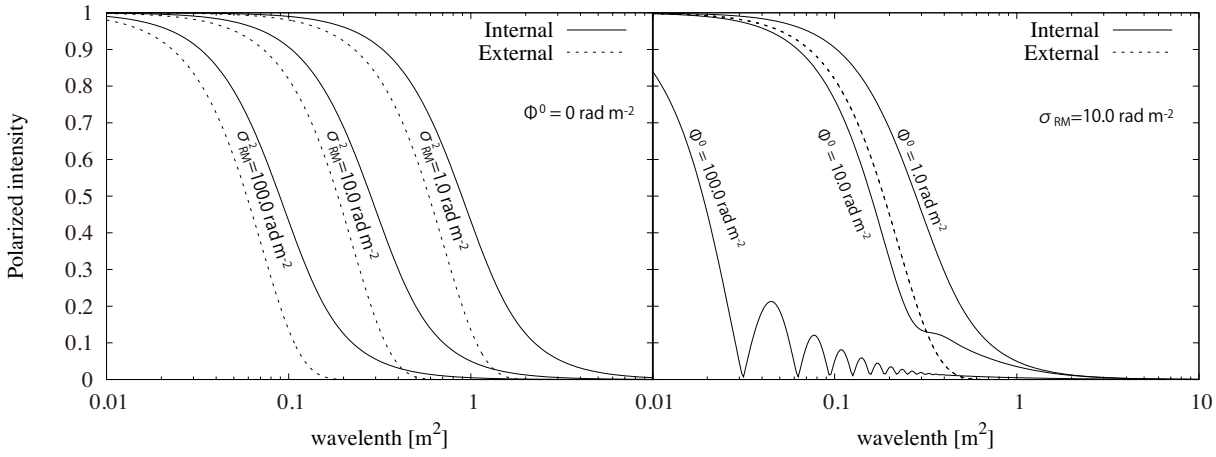

Figure 3.5: The depolarization behavior of internal (solid) and external Faraday dispersion (dashed). In left panel, we fix the regular field equal to zero and vary variance of Faraday depth due to turbulent fields, $\sigma^2_{\rm RM} = K^2 n_e^2 \sigma_z^2 L$ where $L = z_b$ for IFD while $L = R$ for EFD. In right panel, we vary the regular field and fix $\sigma^2_{\rm RM} = 10.0$ rad m^{-2}.

It is called external Faraday dispersion (EFD) which is one of the beam depolarizations. If a telescope beam contains some cells inside, the polarization planes passing through different turbulent magnetic fields blend each other, which cause the depolarization (see (c) in Figure 3.3). This effect occurs at regions without any polarized radiation. Therefore, only the rotation term in Equation (3.19) is needed for consideration. Faraday rotation by each regular and turbulent can be rewritten by just replacing the interval of integration from $z \to z_b$ to $z_b \to$ observer $z_{\rm obs}$ in Equation (3.24) and (3.25). Then the λ^2 dependency is derived as

$$\begin{aligned} P(\lambda^2) &= p \exp\left(2i\lambda^2 \int_{z_b}^{z_{\rm obs}} K n_e B_z^0 dz - 2\lambda^4 K^2 n_e^2 \int_{z_b}^{z_{\rm obs}} \sigma_z^2 d\, dz \right) \\ &= p \exp\left(-2K^2 n_e^2 \sigma_z^2 \lambda^4 R + 2iK n_e B_z^0 \lambda^2 R \right) \ , \end{aligned} \tag{3.31}$$

where $R = z_{\rm obs} - z_b$ is the distance between observer and the emitter. We should emphasize that the regular fields affect only the phase term for changing the Faraday depth of emitter, while turbulent fields change the amplitude of the polarized intensity.

We summarize depolarization behavior caused by Faraday dispersion in Figure 3.5. In the left panel, the dependency on the variance of turbulent fields is shown. The solid and dashed lines represent the IFD and EFD, respectively. The large variance of turbulent fields works more significant. The EFD decomposes the polarization at smaller wavelength. In the right panel, the dependency on the regular field is shown. As seen above, the behavior of the EFD does not change by regular field at all. On the other hand, behavior of IFD approximates to that of the Faraday depolarization when the regular field is strong.

3.3.4 Multiple RM components

The mechanism of this depolarization resembles to the internal Faraday dispersion. Supposing multiple sources in a beam, the polarization planes from the far source and the near source blend each other. If magneto-ionic medium exists between them, the polarized intensity oscillates along λ^2.

$$\begin{aligned} |P(\lambda^2)| &= |e^{2i\chi_{0,1}} + e^{2i(\chi_{0,2}+\phi_s\lambda^2)}| \\ &= 2 + 2\cos(2(\Delta\chi_0 + \phi_s\lambda^2)) \ , \end{aligned} \tag{3.32}$$

where $\Delta\chi_0 = \chi_{0,2} - \chi_{0,1}$ is the intrinsic polarization angle difference between sources and ϕ_s is the integrated RM between sources. The *frequency* of this oscillation is determined by the integrated RM between sources.

3.4 Faraday tomography

From Equation (3.4), it should be noted that the relation between polarized intensity and FDF is similar to the Fourier transform. Therefore, FDF can be reconstructed by the inverted Fourier transform of polarization intensity, i.e.

$$F(\phi) = \frac{1}{\pi}\int_{-\infty}^{\infty} P(\lambda^2)e^{-2i\phi\lambda^2}d\lambda^2 \ . \tag{3.33}$$

However, we can only observe $P(\lambda^2)$ within the observable wavelength range, especially negative λ^2 is never observed. Thus, we introduce the window function $W(\lambda^2)$ which has nonzero value at observable wavelength, otherwise zero. By this function, the observed polarized intensity $\tilde{P}(\lambda^2)$ can be rewritten as

$$\tilde{P}(\lambda^2) = W(\lambda^2)P(\lambda^2) \tag{3.34}$$

Then, reconstructed FDF from incomplete polarized intensity $\tilde{F}(\phi)$ can be rewritten by

$$\tilde{F}(\phi) = \frac{1}{\pi}\int_{-\infty}^{\infty} W(\lambda^2)P(\lambda^2)e^{-2i\phi\lambda^2}d\lambda^2 \ , \tag{3.35}$$

$$= R(\phi) * F(\phi) \ , \tag{3.36}$$

with convolution theorem, where $*$ represents convolution symbol and $R(\phi)$ is known under the name of the rotation measure spread function (RMSF),

$$R(\phi) = K\int_{-\infty}^{\infty} W(\lambda^2)e^{-2i\phi\lambda^2}d\lambda^2 \ , \tag{3.37}$$

$$K = \left(\int_{-\infty}^{\infty} W(\lambda^2)\,d\lambda^2\right)^{-1} \ . \tag{3.38}$$

$R(\phi = 0)$ becomes unity by K.

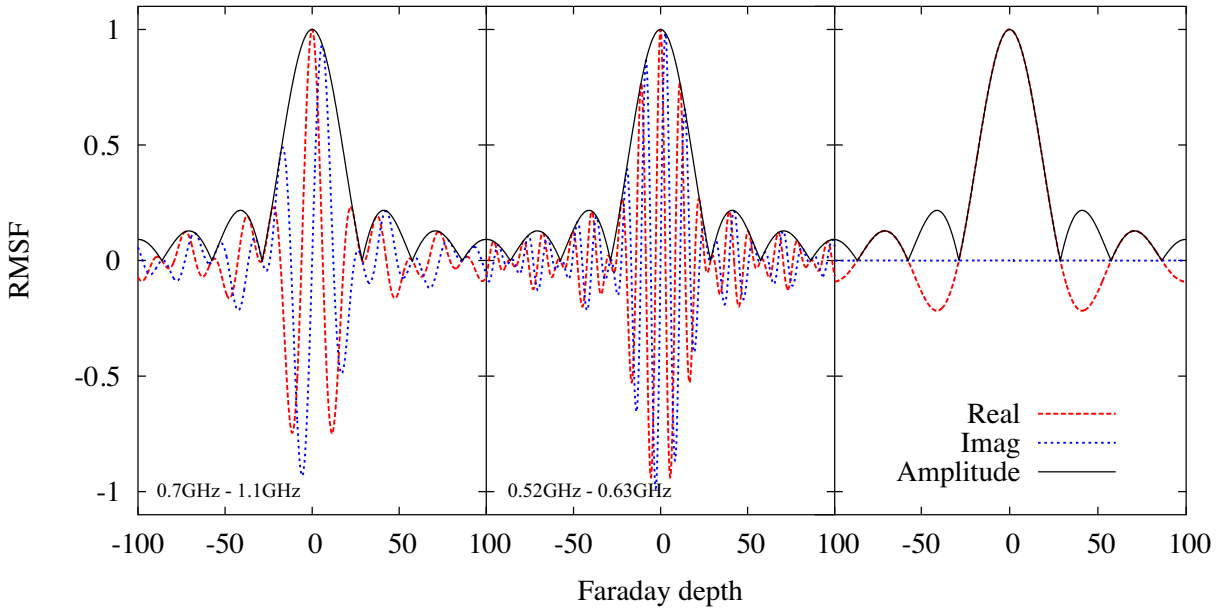

Figure 3.6: The RMSF for the case of ASKAP observing range (700MHz–1800MHz), but the center panel displays the case that observing wavelength range is shifted to longer wavelength. The red dashed and the blue dotted line represent the real and imaginary part, respectively. The black solid line represents the amplitude of the RMSF.

3.4.1 The reference wavelength

Equations (3.36) and (3.37) are not yet the final expressions. At the left panel of Figure 3.6, the RMSF corresponding to ASKAP observing range (700MHz–1.8GHz) is displayed. The real and imaginary part oscillate rapidly. This violent oscillation of phases makes it difficult to estimate the polarization angle of sources correctly, because one can sample Faraday depth space with finite intervals. Furthermore, since the phases of RMSF are proportional to not only ϕ but also λ^2, this difficulty would be serious at long wavelength observation. This fact is clearly shown at the center panel in Figure 3.6, which displays the RMSF with the case that observed range is shifted to longer wavelength than ASKAP.

In order to defeat this difficulty, Brentjens and Bruyn (2005) have proposed an idea. They reconstruct the FDF after the derotation of the rotated angle,

$$\tilde{F}(\phi) = \frac{1}{\pi}\int_{-\infty}^{\infty} \tilde{P}(\lambda^2) e^{-2i\phi(\lambda^2-\lambda_0^2)} d\lambda^2 \ , \tag{3.39}$$

$$R(\phi) = K\int_{-\infty}^{\infty} W(\lambda^2) e^{-2i\phi(\lambda^2-\lambda_0^2)} d\lambda^2 \ , \tag{3.40}$$

where λ_0^2 is called reference wavelength which provides us an optimal derotation angle. Of course, the angle of polarization vectors at $\lambda^2 = 0$ does directly relate with the intrinsic property of the source. However, derotation never losses the information. They also

discuss what λ_0^2 is optimal to defeat difficulty. Ideally, the phase in the main lobe should be corresponds to the actual polarization angle at $\lambda^2 = \lambda_0^2$. Therefore, the best way is to keep the imaginary part as close to zero as possible within the main lobe of the RMSF.

$$0 = \left.\frac{\partial \mathcal{I}[R(\phi)]}{\partial \phi}\right|_{\phi=0} = \left. -K\frac{\partial}{\partial \phi}\int_{-\infty}^{\infty} W(\lambda^2)\, \sin 2\phi(\lambda^2 - \lambda_0^2) d\lambda^2 \right|_{\phi=0}$$

$$\longrightarrow \quad \lambda_0^2 = \frac{\int_{-\infty}^{\infty} W(\lambda^2)\lambda^2\, d\lambda^2}{\int_{-\infty}^{\infty} W(\lambda^2)\, d\lambda^2}\ . \tag{3.41}$$

It shows that the weighted average of observable λ^2 is optimal as λ_0^2. In actuality, the violent oscillation in the main lobe of the RMSF is suppressed, especially the case with a single rectangle window function, $W(\lambda^2) = 1$ for observed wavelength otherwise zero, (see the right panel in Figure 3.6). One can see the other cases, e.g. multiple rectangle window function or not rectangle window function, in Ref. [64, 70].

Then, Equations (3.39) and (3.40) are the final expression sets of Faraday tomography. Please note that the actual intrinsic polarization angle can be estimated after de-derotation, that is

$$\chi_0 = \chi(\phi, \lambda_0^2) - \phi\lambda_0^2\ , \tag{3.42}$$

where $\chi(\phi, \lambda_0^2)$ is an angle estimated by Equation (3.6) and $\phi\lambda_0^2$ is the effect by this derotation.

3.4.2 RMSF as a roll of resolution

One might be noticed that the strategy of Faraday tomography shares a lot of common features with the aperture array synthesis. For instance, the polarized intensities, FDF and RMSF correspond to visibilities, image of sky and dirty beam, respectively (Thus, Faraday tomography is called Faraday Rotation Measure Synthesis as well). That means that the full width at half maximum (FWHM) of RMSF play a roll of resolution in Faraday depth space. In the case of rectangle window function, FWHM of RMSF, $\Delta\phi_{\mathrm{FWHM}}$, can be written by

$$\Delta\phi_{\mathrm{FWHM}} = \frac{2 \times 1.89549...}{\Delta\lambda^2} \approx \frac{2\sqrt{3}}{\Delta\lambda^2}, \quad \Delta\lambda^2 = \lambda_{\mathrm{max}}^2 - \lambda_{\mathrm{min}}^2, \tag{3.43}$$

Equation (3.36) and (3.43) tell us the fact that the quality of reconstruction of FDF is completely determined by the observed wavelength range. The feature of window function does also affect quality of reconstruction. The rectangle window function, which is commonly used, mathematically maximizes resolution and minimize information losses, but some unwanted secondary peak, which is called sidelobe, are shown. Since this sidelobes encourage the appearance of dummy signals, these signals are wanted to be as small as possible. The sidelobes can be smaller by apodization using Gauss window, hann window or humming window. However, the relation between width of main lobe and amplitude

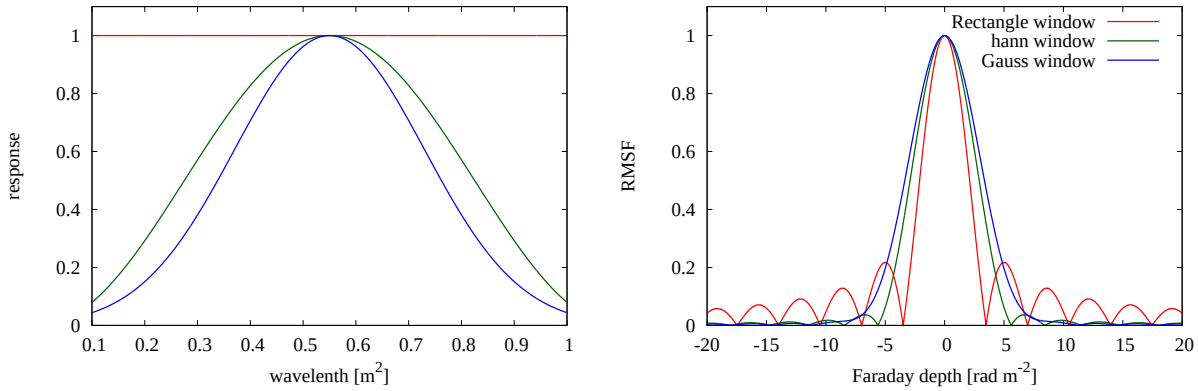

Figure 3.7: The effect of apodization by various window functions. The rectangle window (red) minimizes the FWHM of RMSF, while maximizes the amplitude of sidelobes. On the contrary, Gauss window (blue) minimized the amplitude of sidelobes, while increases the FWHM. hann window function (green) is intermediate.

of sidelobes is trade-off (see Figure 3.7). Therefore, one should select an optimal window function. In this thesis, we select rectangle window function, though amplitude of sidelobes are maximized. We discuss about deconvolution methods for elimination of sidelobes at next chapter.

There are more two quantities which describe the quality of Faraday tomography.

3.4.3 Maximum Faraday thickness

This quantity is motivated by the Faraday depolarization. As we mentioned before, the effect of depolarization would be crucial for longer wavelength and the typical depolarization scale depends on thickness of FDF. Therefore the detectability of the Faraday thick source is limited by observed wavelength. The limit of detectable thickness is called maximum Faraday thickness σ_ϕ. If the thickness of the source is larger than this value, we just observe less than 50% of the intrinsic polarized intensity at $\lambda^2_{\rm min}$. The value is

$$\sigma_\phi \sim \frac{\pi}{\lambda^2_{\rm min}} \ . \tag{3.44}$$

From this point of view, the Faraday thick source which has smaller thickness than σ_ϕ seems to be always detected. From point of view of $\Delta\phi_{\rm FWHM}$, however, only the source which has larger thickness than $\Delta\phi_{\rm FWHM}$ is regarded as the Faraday thick source. That means that σ_ϕ has detectability for small thickness, while $\Delta\phi_{\rm FWHM}$ has detectability for large thickness. Therefore, the reconstruction of Faraday thick source requires $\Delta\phi_{\rm FWHM} < \sigma_\phi$. Substituting Equations (3.43) and (3.44) to this inequality, the qualification for Faraday thick source reconstruction can be led as

$$\lambda^2_{\rm min} < \Delta\lambda^2 \ . \tag{3.45}$$

3.4.4 Maximum Faraday depth

This quantity is the limit of Faraday depth that we can reconstruct. For the Faraday depth larger than this limit, overtone signals can be detected. This problem is caused by discreteness of polarization intensity samples. That means that this problem is serious when the channel resolution is poor. Maximum Faraday depth $|\phi_{\rm max}|$ can be written by

$$|\phi_{\rm max}| \sim \frac{\sqrt{3}}{\delta\lambda^2} \ , \tag{3.46}$$

here $\delta\lambda^2$ is the channel width. For instance, $|\phi_{\rm max}| \sim 2.6 \times 10^4$ rad m^{-2} for 1 MHz channel width.

Please note that $\Delta\phi_{\rm FWHM}$ and σ_ϕ are just rough criteria. It might be sometimes possible that larger thickness than σ_ϕ or two sources separated smaller than $\Delta\phi_{\rm FWHM}$ are detectable for certain circumstances. Thus they should not be treated serious.

Chapter 4

RM CLEAN method as deconvolution

4.1 The CLEAN algorithm

The CLEAN algorithm is one of methods giving one solution of deconvolution, which was first described by Högbom (1974) for image reconstruction using radio interferometers [71]. The aim of the CLEAN is to eliminate the effects of sidelobes due to RMSF. This method is not a mathematical approach, but a simple iterative approach. Basic idea is to find locations and strength of point sources first, then replace dirty beam having side lobe to CLEAN beam, which is usually Gaussian. All point sources detected by CLEAN are listed on CLEAN components. The final image is called CLEANed image, which is the sum of all CLEAN components convolved with CLEAN beam. As we mentioned before, Faraday tomography and aperture array synthesis share a lot of common features. Therefore, the CLEAN algorithm can be applied to Faraday tomography as well. In this case, it is generally called RM CLEAN. Hereafter, we discuss CLEAN in the context of Faraday tomography, not aperture array synthesis.

4.1.1 Högbom CLEAN

The Högbom type RM CLEAN is proceeding by absolute value, not complex value. The procedure is following:

1. Find a peak value of $|\tilde{F}(\phi)|$. The value $|\tilde{F}(\phi_p)|$ at ϕ_p is defined as a Faraday component and it is added to a list of Faraday components.

2. Subtract the shifted-scaled RMSF, $\gamma|\tilde{F}(\phi_p)||R(\phi - \phi_p)|$, from $|\tilde{F}(\phi)|$. Here γ is the gain factor that is generally less than unity.

3. Repeat the above two steps till (A) the $|\tilde{F}(\phi_p)|$ becomes below a noise level ξ, or (B) the iteration number reaches a certain number one adopts $N_{\rm itr}$.

4. Accumulate Faraday components and residuals, where each Faraday component is multiplied by the gain factor and convolve with Gaussian beam. This beam has same FWHM with the RMSF. Thus, the CLEANed FDF $\hat{F}(\phi)$ is given by

$$\hat{F}(\phi) = \sum_{i}^{N} \gamma |\tilde{F}(\phi_p^i)| G(\phi - \phi_p^i) + \text{residuals}, \tag{4.1}$$

where

$$G(\phi) = \exp\left(-\frac{4\ln 2\ \phi^2}{\text{FWHM}^2}\right), \tag{4.2}$$

ϕ_p^i and $|F(\phi_p^i)|$ indicate the i-th Faraday component, and N is the number of Faraday components.

Ideally, Equation (4.1) will be consistent to

$$\hat{F}(\phi) = G(\phi) * F(\phi)\ . \tag{4.3}$$

4.1.2 Demonstration of the RM CLEAN

Here we demonstrate the performance of the RM CLEAN. For demonstration, a reconstructed FDF before deconvolution is displayed at the top panel in Figure 4.1. We adopt CLEAN with following parameters, $\{\gamma, N_{\text{itr}}, \xi\} = \{0.1, 1000, 10^{-3}\}$. This FDF is likely to contain just a single source around $\phi = 0$. the progress of RM CLEAN algorithm is shown at middle panels. The left column displays subtracted FDFs at 10th, 15th, 25th and 100th iteration from top to bottom. Until 10th iteration, main lobe and sidelobes are equally subtracted, however, unsubrtacted peak are likely to be appeared around $\phi = 40$ at 15th iteration. After 15th iteration, both peaks are listed in a Faraday components list. Finally, the RM CLEAN start to converge by 100th iteration and residual reached ξ at about 450 iterations. The right column displays CLEANed FDFs at each iteration. The progress of fine replacing dirty beam with clean beam can be seen. At 25th iteration, the signal of weaker source are appeared on CLEANed FDF as well. The final CLEANed FDF is shown at the bottom panel with model FDF. The CLEANed FDF indicates two sources with amplitude of 9.9 and 0.98 at $\phi = 1.2$ and 41.6 rad m^{-2}, respectively. This result shows a great consistency with input model with amplitude of 10.0 and 1.0 at $\phi = 1.0$ and 40.0 rad m^{-2}, respectively.

However, this method is liable to lead misunderstanding due to steep and asymmetric feature in subtracted FDF (e.g. at second peak of 15th iteration in Figure 4.1). Since RM CLEAN method ignores nonlinear effect in FDF, this feature would be significant for the case of Faraday thick source or multiple sources with a small separation. Discussions about this effects are following.

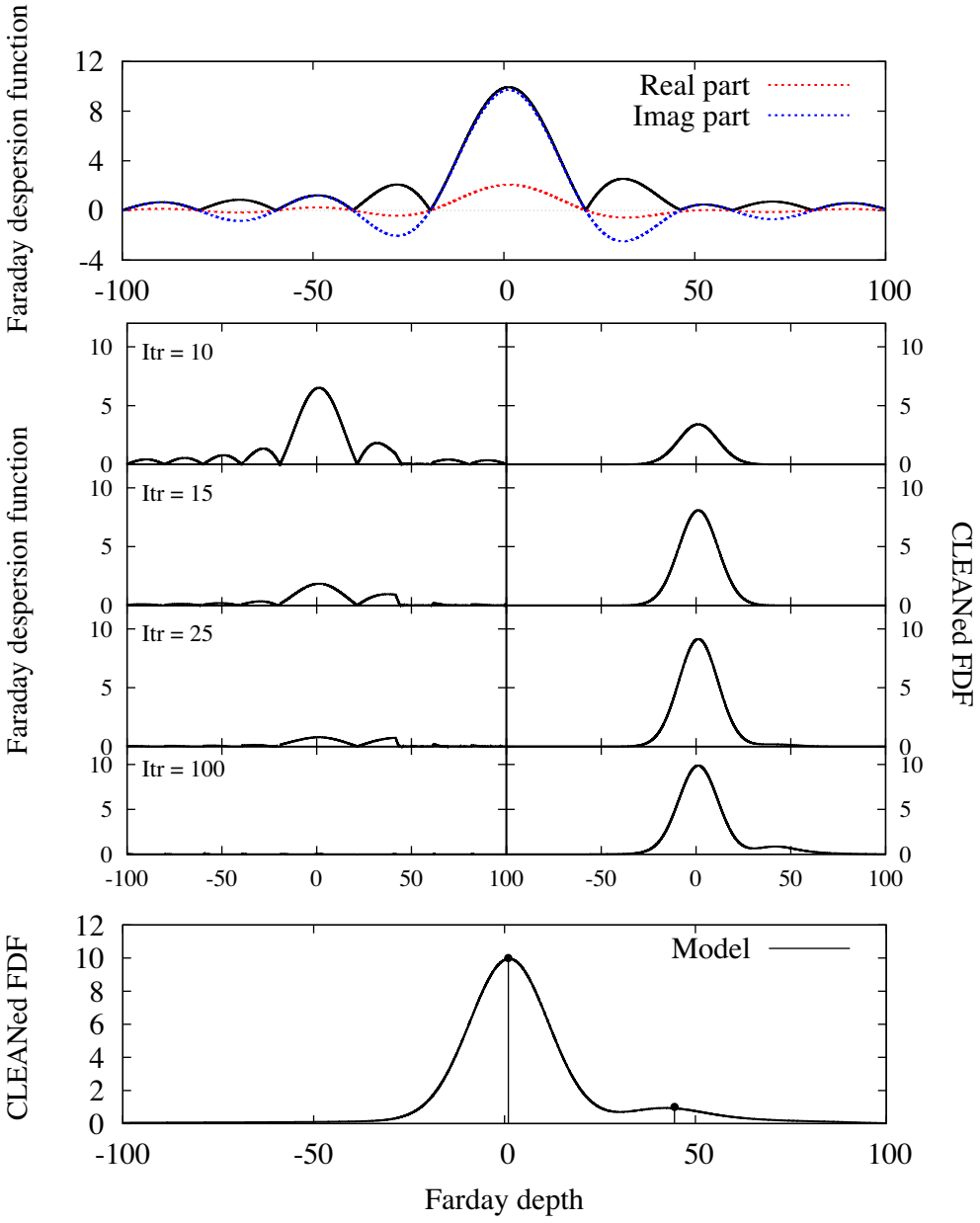

Figure 4.1: Demonstration of RM CLEAN. The top panel displays the reconstructed FDF. The bottom panel shows the CLEANed FDF. The middle panels show the process of RM CLEAN method, at 10th, 15th, 25th and 100th iteration. The left and right panels show subtracted FDFs and accumulated CLEANed FDFs.

4.2 RM ambiguity

Farnsworth et al. (2011) have reported an ambiguity associated with Faraday tomography or RM CLEAN [68]. They considered two sources which separate almost $\Delta\phi_{\rm FWHM}$ with some intrinsic polarization angles, $0°, 45°, 90°$ and $135°$. In some cases, Faraday Tomography with RM CLEAN could resolve two sources. However, in other cases, Faraday tomography with RM CLEAN provides three sources including one false signal or only one sources. This phenomenon is called RM ambiguity. Here we extend Farnsworth's work for investigating the circumstance of the appearance of false signals more systematically [59].

We consider two polarized sources within a single beam, where model sources are described by delta functions. Then the complex polarized intensity can be rewritten by summation,

$$P(\lambda_j^2) = \sum_{k=1}^{2} A_k e^{2i(\chi_{0,k}+\phi_k\lambda_j^2)}, \tag{4.4}$$

where A_k is the polarized intensity, $\chi_{0,k}$ the intrinsic polarization angle and ϕ_k is the Faraday depth of the k-th source. We fix $A_1 = 10.0$, $\phi_1 = 0.0$ and $\chi_{0,2} = 0.0$, and vary A_2, ϕ_2, and $\chi_{0,1}$ for systematically investigating properties of false signals through a number of case studies. The difference of the intrinsic polarization angles,

$$\Delta\chi_0 \equiv \chi_{0,1} - \chi_{0,2} \tag{4.5}$$

is, thus, equal to $\chi_{0,1}$. We consider $0° \leq \Delta\chi_0 < 180°$. Also, the difference of Faraday depths,

$$\Delta\phi \equiv \phi_2 - \phi_1 \tag{4.6}$$

is equal to ϕ_2. We do not take the measurement noise into account because we want to confirm that false signals are not coming from the noise effect but inherent in this method.

In Figure 4.2, we show the results of Faraday tomography and RM CLEAN for the cases with different $\Delta\chi_0$, where $A_2/A_1 = 1.0$ and $\Delta\phi = 22.26$ rad m^{-2} ($1.0\ \Delta\phi_{\rm FWHM}$) are fixed. The black dot-dashed and the solid lines represent the input and reconstructed FDFs, respectively. The shaded area in gray show the CLEANed FDF calculated by RM CLEAN algorithm. The red lines are the CLEAN components. Focusing on the red lines, the two components are correctly detected except for the cases with $110° \leq \Delta\chi_0 \leq 160°$. In the cases with $110° \leq \Delta\chi_0 \leq 160°$, the reconstructed FDFs have a single peak around the mean Faraday depth of the two mode souces.

Furnsworth et al. indicated that two sources with a close separation $\Delta\phi \leq 1.0\ \Delta\phi_{\rm FWHM}$ would be detected as a single source, which is actually confirmed with Figure 4.2. On the other hand, there has not been reported that false signals arise for the cases with sufficiently larger $\Delta\phi$ than the $\Delta\phi_{\rm FWHM}$. In order to make clear the limit of RM ambiguity appearance, we study the cases with $\Delta\phi \geq 1.0\Delta\phi_{\rm FWHM}$ and do not consider the cases with $\Delta\phi \ll 1.0\Delta\phi_{\rm FWHM}$ from the next subsection.

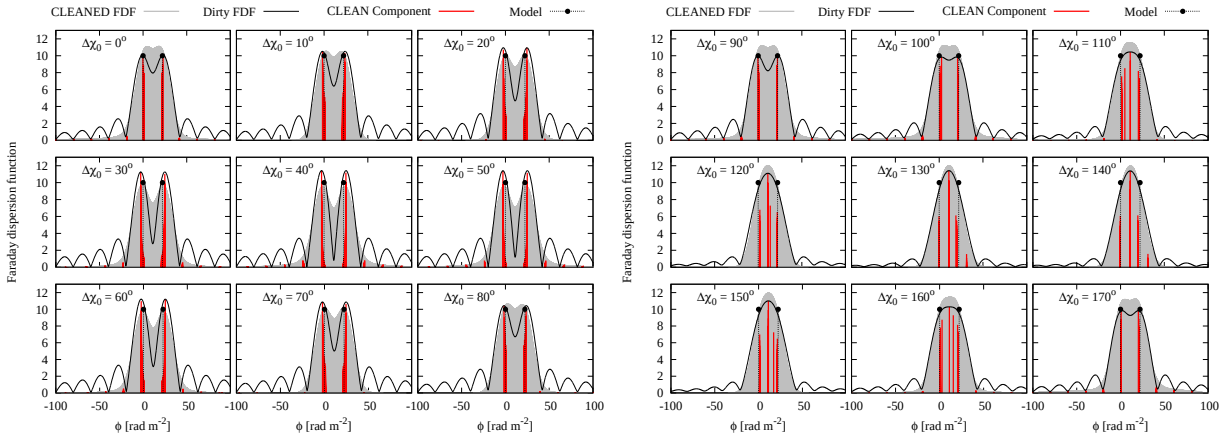

Figure 4.2: FDFs for $\Delta\chi_0 = 0$ - 170 degree, $A_2/A_1 = 1.0$, and $\Delta\phi = 22.26$ rad m^{-2} (1.0 $\Delta\phi_{\rm FWHM}$) for the case with ASKAP. The black dot-dashed and solid lines represent the model and reconstructed FDFs, respectively. The shaded area in gray shows the cleaned FDF calculated by RM CLEAN algorithm. The red lines are the accumulated CLEAN components.

4.2.1 Separation between components

Figures 4.3 shows the FDFs for the cases with $\Delta\phi = 1.4\ \Delta\phi_{\rm FWHM}$. For quantification, we define the false signals as Faraday components arisen in Faraday depth from $\Delta\phi/4$ to $3\Delta\phi/4$ with an amplitude larger than half of amplitude of the largest Faraday component. In all cases, the reconstructed FDF and CLEANed FDF have two peaks near the input Faraday depth. Furthermore the Faraday components located at the correct positions are dominant. However, false signals can be seen in the cases with $0 \leq \Delta\chi_0 \leq 20$ and $\Delta\chi_0 = 170$. Thus, false signals can be appeared even if a source separation is larger than the $\Delta\phi_{\rm FWHM}$ of the RMSF.

In order to understand how large separation is needed to avoid false signals, we investigate the appearance of false signals for the cases with various values of $\Delta\phi$ by fixing the other parameters. For systematic displays, we show the rotation angles of light emitted by the second source ($k = 2$) as a sector which is depicted with a thick line in the left panel of Figure 4.4, where $\chi_{\rm max} = \Delta\phi\lambda^2_{\rm max}$ and $\chi_{\rm min} = \Delta\phi\lambda^2_{\rm min}$ are the rotation angles for $\lambda_{\rm max}$ and $\lambda_{\rm min}$.

The right panel of Figure 4.4 summarizes the results for $\Delta\phi = 1.0 - 1.7\Delta\phi_{\rm FWHM}$. The red sectors represent the range of $\Delta\chi_0$ that false signals appear in the Faraday components. We find that false signals tend to appear when the difference of the intrinsic polarization angle corresponds to the average of the rotated angle, i.e. $\Delta\chi_0 \sim (\Delta\phi\lambda^2_{\rm min} + \Delta\phi\lambda^2_{\rm max})/2$. This would be understandable because the resultant polarizations emitted from the two sources are similar each other in this case, and thus it is rather difficult to separate the both sources correctly. We also find that the range of $\chi_{0,1}$ which induces false signals does not become narrow monotonically as $\Delta\phi$ increases.

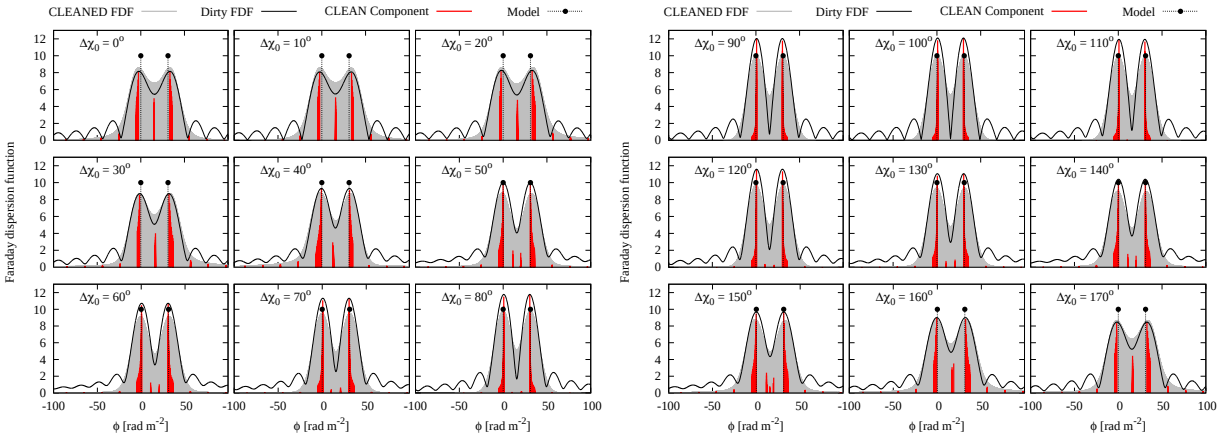

Figure 4.3: Same as Figure 4.2 but for $\Delta\phi = 31.16$ rad m^{-2} (1.4 $\Delta\phi_{\rm FWHM}$) .

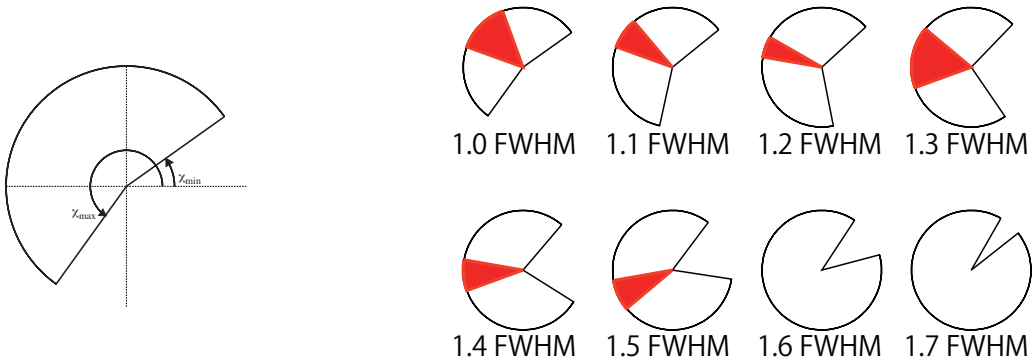

Figure 4.4: Left panel: Definition of the pie display for rotation angles of light emitted by the second source ($k = 2$). $\chi_{\rm max} = \Delta\phi\lambda^2_{\rm max}$ and $\chi_{\rm min} = \Delta\phi\lambda^2_{\rm min}$ are the rotation angles at the first source used in right panel. Right panel: Appearance of false signals. The red sectors represent the range of $\Delta\chi_0$ where false signals appear in the CLEAN components

Figure 4.5 shows the amplitude of the false signals for various $\Delta\phi$ and $\Delta\chi_0$, where we use $\delta\chi_0$ instead of $\Delta\chi_0$, which is defined as,

$$\delta\chi_0 = \begin{cases} \Delta\chi_0 & \text{for} \quad \Delta\chi_0 \leq 90^\circ \\ \Delta\chi_0 - 180^\circ & \text{for} \quad \Delta\chi_0 > 90^\circ. \end{cases} \tag{4.7}$$

We can see that the region in which we see false signals is along the black solid line, which is the track for the polarization satisfying $(\lambda^2_{\rm min} + \lambda^2_{\rm max})/2$ emitted by the second source, i.e. false signals tend to appear when $\Delta\chi_0 \sim (\Delta\phi\lambda^2_{\rm min} + \Delta\phi\lambda^2_{\rm max})/2$ as seen in right panel in Figure 4.4. We can see that the false signals are larger than the correct signals for $\Delta\phi < 1.1\Delta\phi_{\rm FWHM}$. The false signals become weaker for larger $\Delta\phi$ but continue to appear up to $\Delta\phi = 1.45\ \Delta\phi_{\rm FWHM}$. However there is a gap in $\Delta\phi = 1.2 - 1.25\ \Delta\phi_{\rm FWHM}$. The gap corresponding to the location of the second peak of the RMSF whose amplitude is about 20% of that of the main peak. Thus, this gap is considered to be generated by the sidelobe, which enhances the other source and makes the detections easier.

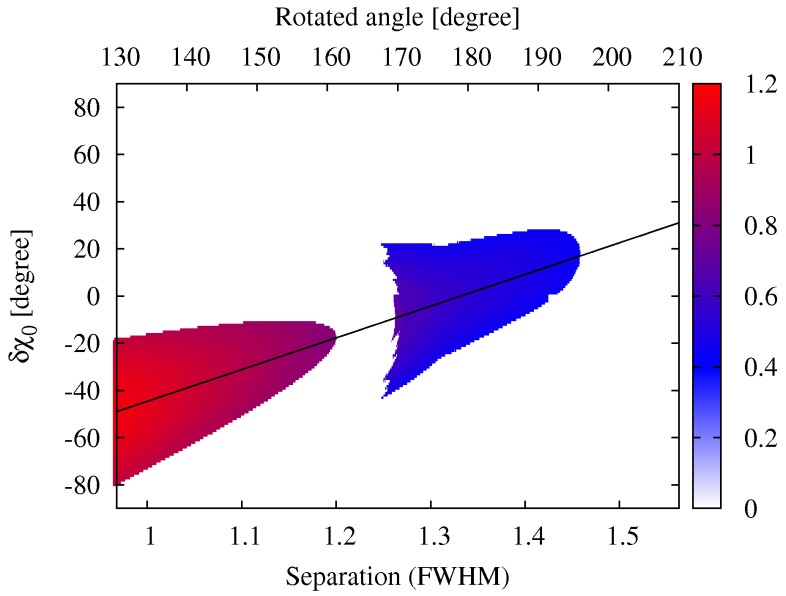

Figure 4.5: Amplitude of false signals in the CLEAN components. Colors show the amplitudes for different separations ($\Delta\phi$) and different intrinsic polarization angles ($\delta\chi_0$). Amplitude is shown as the ratio between amplitudes of the first and second largest Faraday components, and false signals with the amplitude less than 0.5 are not shown. The black solid line represents the rotation angle of polarization at the first source with the wavelength $(\lambda^2_{\rm min} + \lambda^2_{\rm max})/2$ emitted by the second source ($k = 2$)

4.2.2 Intensity ratio

We next investigate the dependence of false signals on the intensity ratio between the two sources, A_2/A_1. For each A_2/A_1, we validate the appearance of false signals in the case with $0^\circ \leq \Delta\chi_0 \leq 180^\circ$ and $0.8 \leq \Delta\phi \leq 1.5$ FWHM then pick up the worst case. The appearance of false signals can be classified into three types. Type (I) is that false signals appear for some intrinsic polarization angles and they are larger than the correct signals. Type (II) is that false signals appear for some intrinsic polarization angles and they are smaller than the correct signals. The type (III) is that there is no false signal for any intrinsic polarization angles.

Figure 4.6 shows the distribution of the three types. There is a tendency that larger A_2/A_1 reduces the generation of false signals and two sources can be successfully resolved even for a separation smaller than $\Delta\phi_{\rm FWHM}$ if $A_2/A_1 \geq 1.8$. It is seen that false signals are serious when the two sources have comparable intensities and the separation is almost $\Delta\phi_{\rm FWHM}$.

Finally, we change frequency coverage. Figure 4.7 shows the results of the same analysis in Figure 4.4 but for the proposed bandwidth of SKA. We find that the results are very similar to the case of ASKAP. Thus, false signals are unavoidable regardless of the bandwidth, if we scaled ϕ separation by $\Delta\phi_{\rm FWHM}$. We expect that false signals appear

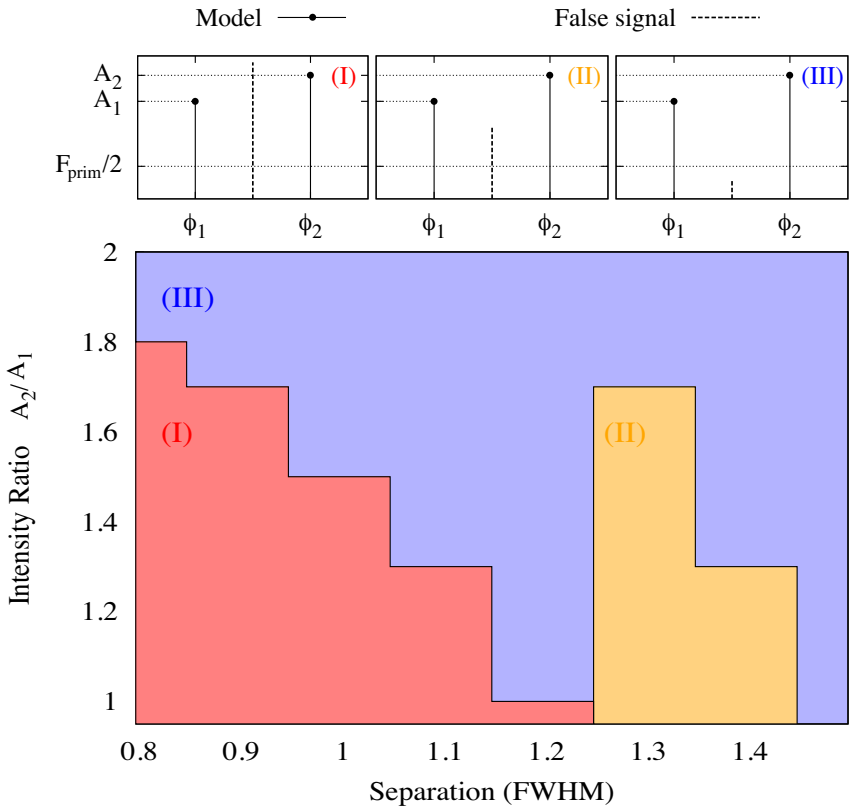

Figure 4.6: Appearance of RM ambiguity in lower panel. (I) False signals appear for some intrinsic polarization angles and they are larger than the correct signals with intensities A_1 and A_2. (II) False signals appear for some intrinsic polarization angles and they are smaller than the correct signals. (III) There is no false signals for any intrinsic polarization angle. In upper panels, we show the examples of type of False signals.

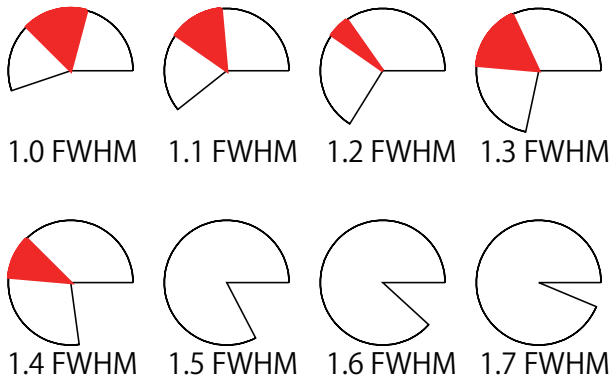

Figure 4.7: Same as Figure 4.4 but for the case of SKA.

in the cases with a certain $\Delta\chi_0$ whenever $\Delta\phi$ is less than $\sim 1.5\Delta\phi_{\rm FWHM}$.

4.3 Phase RM CLEAN

The RM CLEAN method traditionally considers only the absolute value of FDF when the shifted-scaled RMSF is subtracted from the reconstructed FDF. However the FDF is a complex variable and each real and imaginary part of the FDF should have information. Heald (2009) has utilized both parts in the clean step [70]. In his RM CLEAN method, part of procedures are improved from the traditional RM CLEAN method. That is:

1. Find the peak value of $|\tilde{F}(\phi)|$. $\tilde{F}(\phi_p)$ at ϕ_p is added to a list of **complex** Faraday components.
2. Subtract the shifted-scaled **complex** RMSF, $\gamma\tilde{F}(\phi_p)R(\phi-\phi_p)$, from $\tilde{F}(\phi)$.
3. 3rd and 4th steps are the same as Högbom type of the RM CLEAN method.

This method, named Phase RM CLEAN, can provide us not only better deconvolution results, but also ability to estimate the intrinsic polarization angle χ_0, as we will demonstrate in following subsections.

4.3.1 Demonstration of the Phase RM CLEAN

In order to compare with Högbom's CLEAN, we show the snapshots of the progress of Phase RM CLEAN in Figure 4.8. The real and imaginary part are shown by red and blue dashed line, respectively. The weaker component starts to be appeared at 15th iteration as with RM CLEAN. However, FDF is smooth at the entire Faraday depth domain. The computational cost does not change a lot. Although the subtraction step work on both real and imaginary part, residuals reaches ξ by 260 iterations, which is significantly smaller than 450 iterations of RM CLEAN algorithm. The smooth subtraction might cause small iteration number.

4.3.2 Mitigation of the RM ambiguity by Phase RM CLEAN

We revisit the simulation with two Faraday thin sources discussed at Section 4.2. In Figure 4.9, we describe comparisons between results of RM CLEAN and Phase RM CLEAN. The left panel represents the result for the case of $\Delta\phi = 1.1$ FWHM in which just one single peak can be reconstructed by Faraday tomography (gray shadow). Thus, CLEANed FDF also can have a single peak. In fact, RM CLEAN provides a single peak (blue dashed line). However, CLEANed FDF by Phase RM CLEAN method generates a volcano–shape peak (red dashed line). This feature could be an important implication that multiple sources exist within a beam, while the RM CLEAN method gives misunderstandable (an almost-Gaussian) CLEANed FDF which is hard for us to realize multiple sources within a beam.

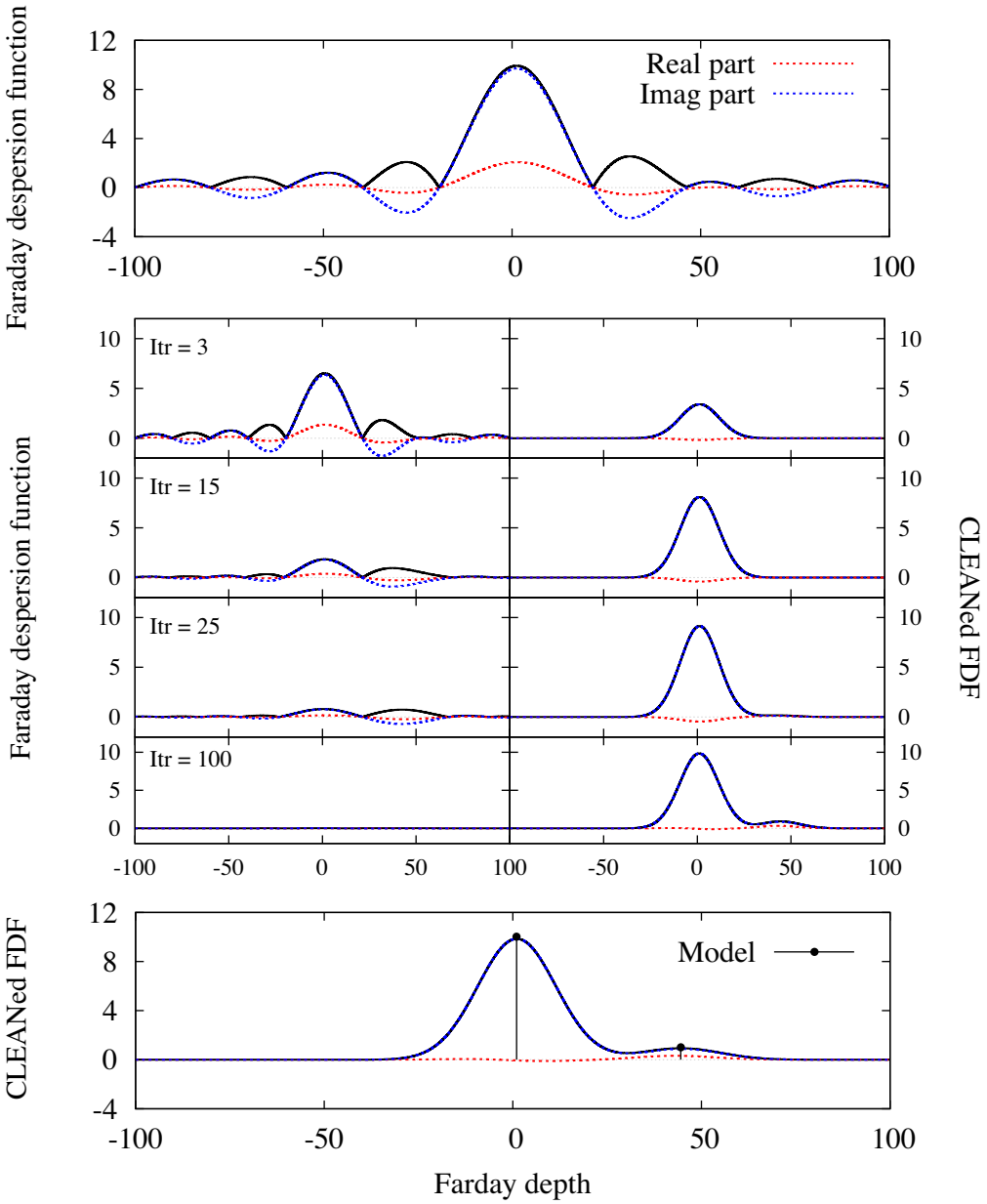

Figure 4.8: Same with Figure 4.1 but for the case of Phase RM CLEAN. Red and blue represent the real and imaginary part.

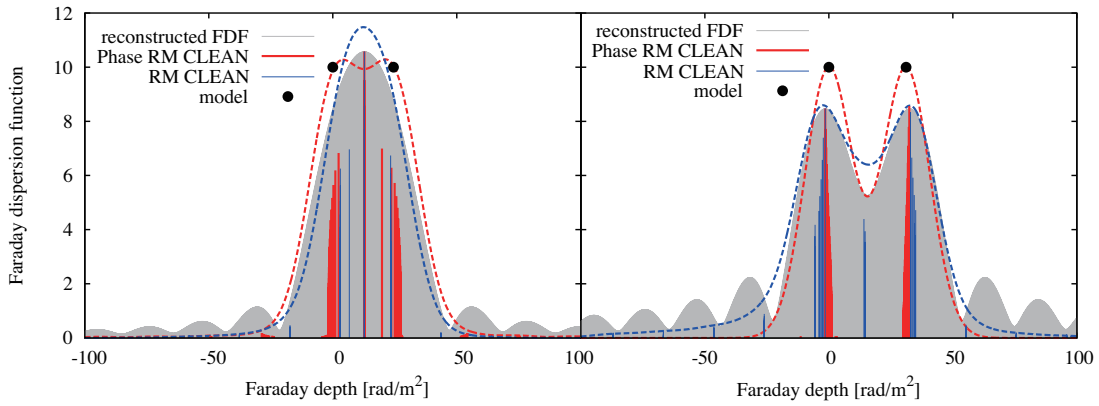

Figure 4.9: The left and right panels show the FDFs for the cases of type (I) ($\Delta\phi = 1.1$ $\Delta\phi_{\rm FWHM}$, $\Delta\chi_0 = 30°$ and $A_2/A_1 = 1.0$) and type (II) ($\Delta\phi = 1.4$ $\Delta\phi_{\rm FWHM}$, $\Delta\chi_0 = 170°$ and $A_2/A_1 = 1.0$), respectively. The black lines with marks show the input FDF, and the gray shadow show the reconstructed FDF. Solid and dashed color lines represent Faraday components and CLEANed FDF, respectively. Blue and red lines represent the results with the RM CLEAN method and the Phase RM CLEAN method, respectively.

The right panel represents the result for the case of $\Delta\phi = 1.4$ FWHM in which RM CLEAN gives false Faraday components weaker than model sources. On the other hand, Phase RM CLEAN method provides the Faraday components just around the two model sources without false signals. Furthermore, the CLEANed FDF given by the Phase RM CLEAN method has more clear two peaks.

The mitigation of RM ambiguity can be seen in Figure 4.10, which shows the false-signal appearance for the case of Phase RM CLEAN. Here, we explored the appearance for $0° \leq \Delta\chi_0 \leq 180°$, and showed the worst result. We find that the region of type (II) is disappeared by Phase RM CLEAN method. It clearly indicates that type (II) false signals are derived from the algorithm of the RM CLEAN method, and Phase RM CLEAN does not bring them. On the contrary, the region for type (I) does not change at all. It means that type (I) false signals are the matter of Faraday tomography, but not CLEAN algorithm.

4.3.3 Application for Faraday thick source

We next demonstrate the case of a Faraday thick source defined as a Gaussian function, see Equations (3.14) and (3.15). Here we set $\sigma_w = 0.3\Delta\phi_{\rm FWHM} \sim 6.7$ rad m^{-2}, $\chi_0 = 30.0°$ and the amplitude is unity.

The difference between results with the RM CLEAN method and the Phase RM CLEAN method is shown in left panel of Figure 4.11, where lines are the same with Figure 4.9. We can see that the RM CLEAN method makes up widespread false Faraday components corresponding to side lobes of the RMSF. Consequently, the CLEANed FDF

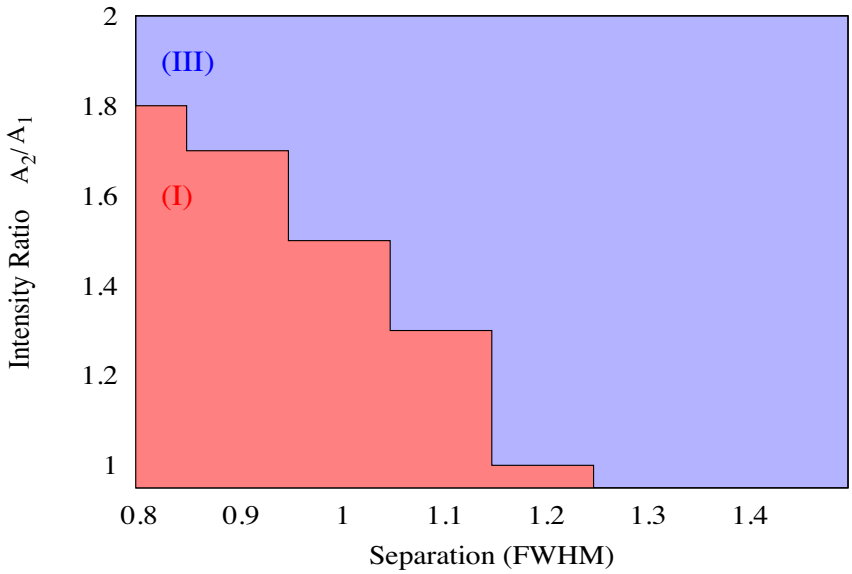

Figure 4.10: Same with Figure 4.6 but for Phase RM CLEAN

has a wide tail around the peak. Such a diffusive reconstruction can be dramatically improved by the Phase RM CLEAN. CLEANed FDF by Phase RM CLEAN has the shape like more *Gaussian*.

Looking at the process of the CLEAN algorithms, we can explain the origin of widespread false Faraday components. The right panel of Figure 4.11 shows the cleaning process in the RM CLEAN method (blue) and the Phase RM CLEAN method (red). Subtracted FDFs at the 5th, 15th and 50th iterations are shown. By around the 15th iteration, the RM CLEAN method mainly subtracts the main lobe. Then, some spiky shapes appear at large Faraday depth by around the 50th iteration. These spikes seem to be caused by the shape of the absolute value of RMSF having zero value points at $\phi = n\pi/2(\lambda^2_{\rm max} - \lambda^2_{\rm min})$ $(n = 1, 2, 3, \dots)$. At this points, the FDF is not subtracted, then residuals can become peaks and be added to the list of Faraday component. Such false signals can be also seen in the bottom panel of right panel of Figure 4.9. On the other hand, the Phase RM CLEAN can subtract FDF smoothly, hence spikes do not appear. It shows that the method does not provide the seeds of false signals or large sidelobes.

4.4 Estimation of intrinsic polarization angle

The most important point of the Phase RM CLEAN is an ability to estimate the intrinsic polarization angle of sources χ_0. The polarization angle $\chi(\phi)$ can be estimated for each Faraday component $\tilde{F}(\phi_p)$ by

$$\chi(\phi_p) = \frac{1}{2} \arctan \left(\frac{\mathcal{I}m[\tilde{F}(\phi_p)]}{\mathcal{R}e[\tilde{F}(\phi_p)]} \right), \tag{4.8}$$

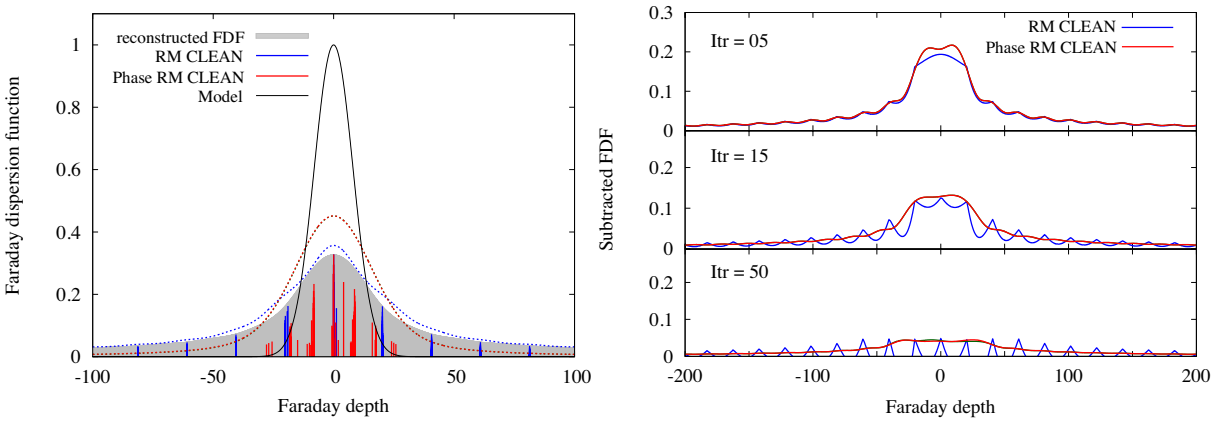

Figure 4.11: **Left panel**: Reconstructions with the RM CLEAN method and the Phase RM CLEAN method for the case of single Faraday thick source. Lines and marks are the same with Figure 4.9. **Right panel**: The progress of RM CLEAN (blue) and Phase RM CLEAN (red). The spiky shapes are appeared for the case of RM CLEAN.

then the intrinsic polarization angle $\chi_0(\phi)$ can be estimated after derotation by Equation (3.42).

First we carry out the pseudo observation of a single source then estimate the intrinsic polarization angle. Figure 4.12 shows the results. The upper four panels from the left to right show the input (x-marks) and estimated (red circles) intrinsic polarization angles for the cases with $\chi_0 = 0°$, $30°$, $60°$ and $90°$. The Phase RM CLEAN seems to achieve good estimations for the case of a single source regardless of the input intrinsic polarization angles.

Next we assume double thin sources and change both of intrinsic polarization angles, $\chi_{0,1}$ and $\chi_{0,2}$. Faraday tomography can not separate double sources when the separation is smaller then 1.3 FWHM due to the RM ambiguity. Therefore, we simulate only larger separation case ($>$ 1.4 FWHM). The left panels of Figure 4.13 show the results for the case of 1.4 (red), 1.7 (blue) and 2.0 (green) FWHM separation. Since there is a bunch of Faraday components detected around Faraday depths of each thin source, we display the averages of ϕ_p and $\chi_{0,p}$ for Faraday components for each thin source. Error bars indicate the maximum and minimum values for the Faraday components. It can be seen that the estimation is not perfect, but accuracy is satisfactorily enough.

In the right panels of Figure 4.13, we display the systematic error on the estimations of the intrinsic polarization angle (left) and Faraday depth (right) for the source 1 at $\phi = \phi_1 = 0$. The color shows the difference between the input and estimated values. As seen, the systematic error only depends on a difference between input intrinsic polarization angles of the two sources, $\Delta\chi_0$. We confirmed that the systematic error is up to ~ 6 degrees for all possible choices of $\chi_{0,1}$ and $\chi_{0,2}$ within 0 – 180 degrees. The error of Faraday depth ϕ_p has a negative correlation with the error of χ_0. Here, 5 degrees is consistent with 0.8 rad m^2 $\times \lambda_0^2$, $\lambda^2 \sim 0.1035$ m^2 for the case of ASKAP.

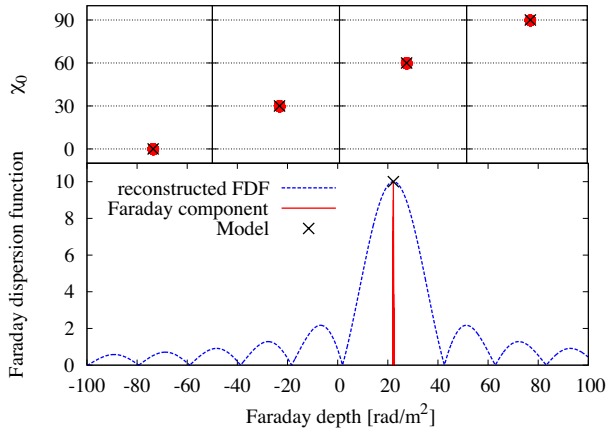

Figure 4.12: The intrinsic polarization angle estimation for the case of a single source. The upper four panels from the left to right show the input (x-marks) and estimated (red circles) intrinsic polarization angles for the cases with $\chi_0 = 0°$, $30°$, $60°$ and $90°$. The reconstructed FDF (blue dashed), Faraday components (red solid) and model value (black x-mark) are shown in the lower panel.

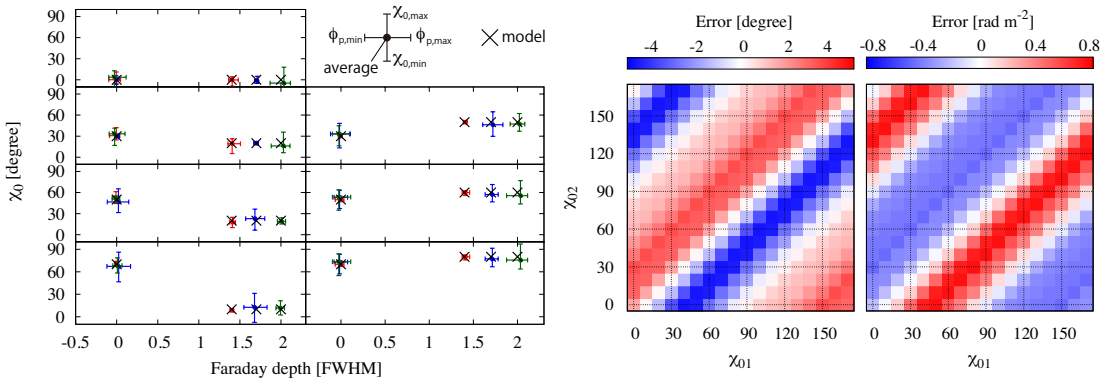

Figure 4.13: Left panel:The intrinsic polarization angle estimation in the case of double thin sources. Results for the case of 1.4, 1.7 and 2.0 $\Delta\phi_{\mathrm{FWHM}}$ separation are shown. Seven examples of the input (x-marks) and estimated (red, blue and green, respectively) intrinsic polarization angles. Input values are arbitrary selected. Points with error bars indicate the average with the minimum and maximum values for Faraday components for each thin source. Right panel: The systematic error on the estimations of intrinsic polarization angles (left) and Faraday depths (right) for the source 1 at $\phi = \phi_1 = 0$. $\chi_{0,1}$ and $\chi_{0,2}$ are the input intrinsic polarization angles for the two sources separated 1.7 $\Delta\phi_{\mathrm{FWHM}}$.

Chapter 5

Exploring the magnetic fields in the intergalactic medium

The one of the most significant advantages of Faraday tomography is an ability to individually estimate RMs for each component on a LoS. Associating with the feasibility of broadband observation by SKA or SKA pathfinders, this ability is hoped to make a great contribution to searching the intergalactic magnetic fields (IGMF). In this section, we discuss the strategy for exploring the IGMF by future and ongoing radio interferometers [60], then show the feasibility of the strategy [61].

5.1 The observational strategy

Let us start to understand the contribution of the IGMF to FDF. As we have shown before, FDF represents the intensity distribution as a function of Faraday depth on the LoS. Since the emission from intergalactic medium is quite slight, the contribution of IGMF to FDF can be seen as a shift of emitted components. This fact leads an idea that the RM due to IGMF, $\mathrm{RM_{IGMF}}$, might be measured as a gap between bright sources.

However, this gap also can be produced by RMs of discrete intervening galaxies or associated media surrounding sources, such as clouds, Hα filaments and swept IGM by jet. Therefore, LoSs which contain of such contaminations should be avoided. The RMs of intervening galaxies and associated media surrounding sources may have a strong correlation with optical absorbers, and/or could show small polarization degree due to depolarization [72, 73]. Thus, we could discard sources with such contaminations. Note that the $\mathrm{RM_{IGMF}}$ would not affect depolarization, since the IGMF is expected to be smooth enough within the beam size of $\sim$ arcsecond [74, 75]. Furthermore, RMs for associated media of distant sources could be small due to $(1+z)^{-2}$ dilution factor. Hommond et al. (2012) estimated the dilution and claimed that sources at $z = 1$ should only contribute a standard deviation of RMs $\sim$ 1.5–3.75 rad m^{-2} [73].

Hereafter, therefore, it is assumed that we can exclude the systems with significant contamination, then the shift of FDF is only caused by the $\mathrm{RM_{IGMF}}$.

5.1.1 Strategy A : Compact source behind diffuse source

Using selected sources, we first consider an observation of a background compact source B, e.g. emission from a radio galaxy or a quasar, behind a foreground diffuse source A, e.g. Galactic emission (see (a) in Figure 5.1). If emission from source B travels not only through source A but also cosmic web A between sources, the contribution by cosmic web A can be seen as a gap between source A and B in Faraday depth domain since emission from IGM is generally much weaker than the others.

The situation arises if all signs of cumulative RMs of the two sources and the comic web by chance. Otherwise, some of them would overlap each other in ϕ domain. Since the RMs are accumulated like random walk process, the possibility is 25%, which is reasonably high enough to select samples from several observations. Even if the source B is overlapped on cosmic web component by reversal of magnetic fields, the gap could still exist when the RM of the cosmic web is much larger than RM of source B. Therefore, the possibility for finding the gap can be larger than 25%.

For this strategy, foreground emissions are necessary to be detected. The intensity of Galactic diffuse emission toward high Galactic latitudes can be scaled as

$$I \sim 0.95 \left(\frac{\nu}{\mathrm{GHz}}\right)^{-1.5} \left(\frac{\Omega}{\mathrm{arcmin}^2}\right) \quad \mathrm{mJy}, \tag{5.1}$$

where ν is frequency and Ω is the beam size [76] which becomes large toward lower latitudes. The diffuse emission is thus significant, unless we observe very bright compact sources.

If the source B is a distant source, the FDF of the source B would be Faraday thin. However we keep considering small thickness for compact sources since the thickness as well as the RMSF are notable ambiguities to probe the IGMF, particularly for observations with limited bandwidths. If the source B is Faraday thin, the gap is sharpened. Then the estimation of the RM due to the IGMF is rather improved.

5.1.2 Strategy B : Pair compact sources

Second idea is the comparison of FDFs for different LoSs ((a) and (b) in Figure 5.1). If source B and C locate close enough each other, they would share the source A and cosmic web A. Therefore, the contributions from source A and cosmic web A can be canceled out by subtracting one FDF from another, then the difference of structure of FDF should be revealed. If the cosmic web B exists between source B and C, the gap might be seen between these sources. For this strategy, it should be confirmed that how much RMs will change with respect to angle separations. Figure 5.2 shows the RM difference as a function of the angular separation, $(\Delta\mathrm{RM})_{\mathrm{rms}} = \langle\sqrt{|\mathrm{RM}(\vec{x}-r) - \mathrm{RM}(\vec{x})|^2}\rangle_{\vec{x}}$, which is averaged over the direction $\vec{x}$ where r indicates the angular separation between $\vec{x}$ and the other [75, 77]. The thick line represents RM difference of the GMF. Note that the angular separation is toward low Galactic latitude. Considering 10.0 rad m^{-2} as the RM of magnetic fields in the cosmic web, the RM difference of the GMF could be only 5% (0.5

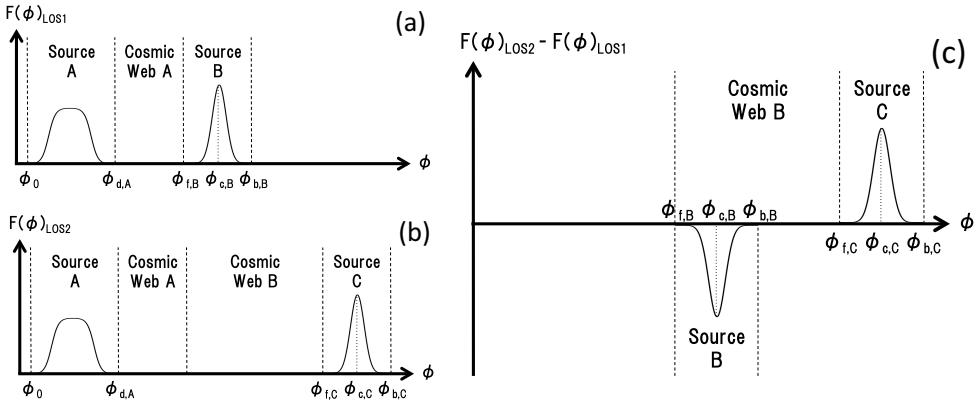

Figure 5.1: (a)Schematic picture of FDF, $F(\phi)$ for the observation of a compact source B behind as diffuse source A and cosmic web A. (b) Same as (a) but for another observation for the compact Source C close to Source A on the sky and behind a diffuse Source A and Cosmic Webs A and B. (c) Difference between two FDFs for two LOSs.

rad m^{-2}) for 1 degree angular separation. Also the thin lines show RM difference of IGMF integrated up to redshift 0.1, 0.3, 0.5 and 1.0 from bottom to top, respectively. 10% level of RM difference can be predicted for 0.1 degree angular separation when the source B is located at $z = 0.3$. Note that much smaller-scale structures have been observed toward the Galactic plane [78, 79].

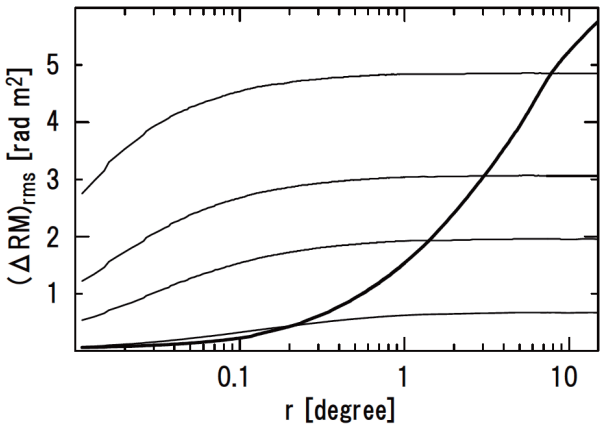

Figure 5.2: The root mean square of the RM difference. The thick line represents that of Galactic magnetic fields. The thin lines are that of IGMF integrated up to redshift 0.1, 0.3, 0.5 and 1.0.

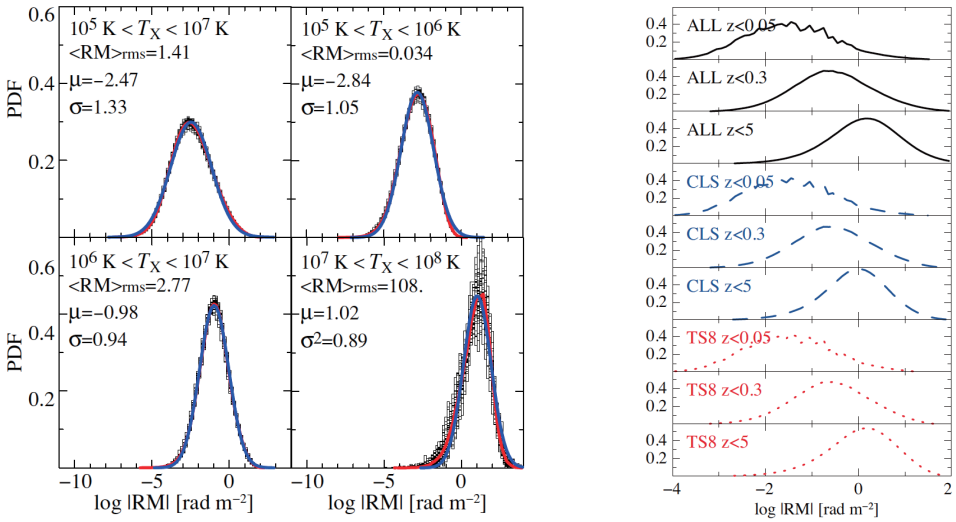

Figure 5.3: PDF of |RM| through LoSs for different temperature regions (left panels) and accumulated from high redshift (right panels) [74, 75].

5.2 Expected Rotation Measure due to the IGMF

When the coherent length of the magnetic fields in the intergalactic medium is smaller than path length of synchrotron emission, the RM accumulation along the path should be a random walk process. Akahori and Ryu have reported the probability distribution function (PDF) of accumulated RMs [74, 75]. Figure 5.3 shows PDFs calculated from simulation by Ryu et al. (2008) [44]. The left panels display the PDFs for various temperature ranges. In hot region, $10^7 < T < 10^8$K, such as ICM, $\langle \mathrm{RM} \rangle_{\mathrm{IGMF}} = 108$ rad m^{-2} is predicted. On the other hand, $\langle \mathrm{RM} \rangle_{\mathrm{IGMF}} \sim 3$ rad m^{-2} is estimated in WHIM, $10^6 < T < 10^7$K, such as filament. The right panels display the PDFs of |RM| of integrating filaments up to high redshift. Color indicates the difference of criteria to eliminate contribution from clusters. This results shows the RMS value could reach several 10 rad m^{-2} when RM is integrated up to $z = 5$. Therefore, we employ RM value from 1 rad m^{-2} to several 10 rad m^{-2} as $\mathrm{RM}_{\mathrm{IGMF}}$.

5.3 The model of the Faraday dispersion function

Instead of observational data, we use the data calculated from FDF models. We adopt the Gaussian function as the Faraday dispersion function, for both diffuse and compact sources because this simple function can analytically predict the polarized intensity via Equation (3.15). Furthermore, it is very convenient to understand the behavior or properties of the polarized intensity as well as the results of the Faraday tomography. Please note that this model would not be realistic, as we will discuss in Chapter 6. Then the

FDF model for Strategy A can be represented as,

$$F(\phi) = \frac{f_d}{\sqrt{2\pi}\delta\phi_d^2} \exp\left[-\frac{(\phi-\phi_d)}{2\delta\phi_d^2}\right] e^{2i\chi_{0d}} + \frac{f_c}{\sqrt{2\pi}\delta\phi_c^2} \exp\left[-\frac{(\phi-\phi_c)}{2\delta\phi_c^2}\right] e^{2i\chi_{0c}} \ . \tag{5.2}$$

The first term is a component of the diffuse source, where ϕ_d is Faraday depth up to the center of the source, $\delta\phi_d$ is the typical Faraday thickness of the source and χ_{0d} is the intrinsic polarization angle. Finally, f_d is the total polarized intensity of the source in unit of Jy. The second term is that of the compact source, where the parameters for the compact source are showed with subscript c instead of d in the first term.

Figure 5.4 shows the polarized intensities. The black line represents the case of the strategy A with parameters $f_d = f_c = 0.1$, $\phi_d = 9.0$ rad m^{-2}, $\delta\phi_d = 3.0$ rad m^{-2}, $\chi_{0d} = 0$ rad, $\phi_c = 22.2$ rad m^{-2}, $\delta\phi_c = 0.4$ rad m^{-2} and $\chi_{0c} = \pi/4$. For the sake of explanation of the behavior, we plot the polarized intensities of the case with only the diffuse or the compact source, which are described by the blue and red line, respectively. Additionally, the sum of the blue and red lines is also shown by the green line. The effect of Faraday depolarization can be clearly seen on the blue and red lines. Because the polarized intensity of diffuse source drops at shorter wavelength due to its larger Faraday thickness, polarized intensity of compact source is dominated at longer wavelength ≥ 1 m^2. Thus it can be predicted that the observatory which covers just longer wavelength, such as LOFAR, would be able to detect only the compact source. The reason why the green and black line do not correspond each other is because of the effect of multiple component depolarization (see Section 3.3.4). This wavelength range which covers oscillating structure allows us to obtain the information of both of diffuse and compact source. Therefore, wide band observation of this range would be important for the FDF reconstruction.

In order to quantify the IGMF, the edge of the source should be defined. Although this should be validated from the distribution of relativistic and thermal electrons as well as the property of magnetic fields in the source, they have huge uncertainties. Therefore, we assume that the edges are located at 3–σ distance from the center. Then, the RM of IGMF can be defined by

$$\mathrm{RM_{IGMF}} = (\phi_c - 3\delta\phi_c) - (\phi_d - 3\delta\phi_d) \ . \tag{5.3}$$

With above parameters, $\mathrm{RM_{IGMF}}$ corresponds to ~ 3 rad m^{-2}.

5.4 Specification of Radio Observatories

We assume observations by ongoing radio observatories, e.g. ASKAP, GMRT and LOFAR HBA, and their combinations. The wavelength ranges covered by them are summarized in Table 5.1 and the right panel in Figure 5.4. Unfortunately, no ongoing observatory covers oscillating region, such as 0.1 to 1 m^2. Furthermore, we inspect the ability of the future observation, SKA. The SKA covers very wide wavelength ranges including oscillating region. Then, the parameters showing the basic processing capability of Faraday tomography, i.e. $\Delta\phi_{\mathrm{FWHM}}$, σ_ϕ and $|\phi_{\mathrm{max}}|$, are summarized in Table 5.2 for each observatory and their combination.

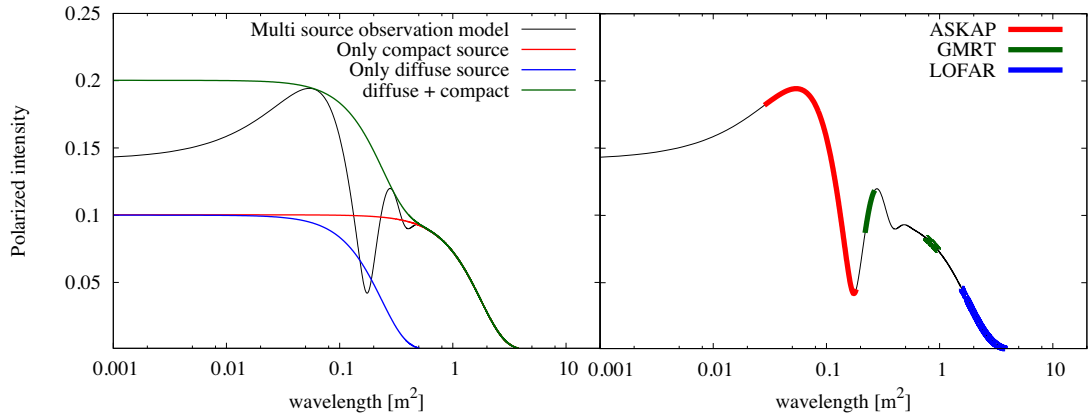

Figure 5.4: The plots of polarized intensities. The black line represents the case of the strategy A. The blue and red lines show the case with only a diffuse or a compact source, respectively. Finally, the green line represents the sum of polarized intensity of both cases.

Table 5.1: Specifications of radio observatories

Observatory	Frequency (GHz)	λ^2 (m^2)	Channel
LOFAR LBA[1]	0.030–0.080	14.00–99.00	62,000
LOFAR HBA[1]	0.120–0.240	1.600–6.200	156,000
GMRT 327[2]	0.305–0.345	0.760–0.970	256
GMRT 610[2]	0.580–0.640	0.220–0.270	256
ASKAP[3]	0.700–1.800	0.027–0.180	60,000
SKA$_2$ low[4]	0.070–0.450	0.444–18.37	380,000
SKA$_2$ mid[4]	0.450–10.00	0.0009–0.444	67,000

[1] LOFAR page; http://www.astron.nl/radio-observatory/astronomers/lofar-astronomers
[2] [80]
[3] ASKAP page; http://www.atnf.csiro.au/projects/askap/
[4] SKA memo 130; http://www.skatelescope.org/pages/ page_memos.html

5.5 The performance of the Faraday Tomography

We first investigate the performance of the Faraday tomography. The most important point is that we do not need to assume any model for FDF. Here we do not take measurement noise into consideration in order to focus on the performance of Faraday tomography itself. The parameters for the FDF model are fixed as $f_d = f_c = 0.1$, $\phi_d = 9.0$

Table 5.2: Parameters of basic processing capability

Observatory	$\Delta\phi_{\rm FWHM}$ rad m^{-2}	σ_ϕ rad m^{-2}	$\lvert\phi_{\rm max}\rvert$ rad m^{-2}
ASKAP	2.44×10^{1}	116.35	6.79×10^{5}
GMRT	1.36×10^{1}	14.28	8.89×10^{3}
LOFAR	8.20×10^{-1}	1.96	5.87×10^{4}
ASKAP + GMRT	2.88×10^{0}	116.35	6.79×10^{5}
ASKAP + LOFAR	7.80×10^{-1}	116.35	6.79×10^{5}
GMRT + LOFAR	7.60×10^{-1}	14.28	6.79×10^{5}
ASKAP + GMRT + LOFAR	7.20×10^{-1}	116.35	6.79×10^{5}
SKA_2 low	2.11×10^{-1}	7.08	3.67×10^{5}
SKA_2 mid	8.61×10^{0}	3490.66	2.61×10^{5}
SKA_2	2.06×10^{-1}	3490.66	4.21×10^{5}

rad m^{-2}, $\delta\phi_d = 3.0$ rad m^{-2}, $\chi_{0d} = 0$ rad, $\delta\phi_c = 0.4$ rad m^{-2} and $\chi_{0c} = \pi/4$ and Faraday depth of the compact sources ϕ_c is changed from 22.2 to 82.2 rad m^{-2}. For $\phi_c = 22.2$ rad m^{-2}, the $\rm RM_{IGMF}$ corresponds to 3 rad m^{-2}. The CLEAN parameters are $\{\gamma, N_{\rm itr}, \xi\} = \{0.1, 10000, 10^{-4}\}$, then all cases are terminated by ξ in this case.

5.5.1 Strategy A

We first investigate the strategy A. This strategy does not require special situation, but requires only a source behind the Galaxy. Hence, the huge number of radio emitters can be observed by near future observations, then statistical discussions can be easily applied.

Figure 5.6 shows the polarized intensities (left) and polarization angles (right) for $\rm RM_{IGMF} = 6.0$, 18.0, 33.0, 48.0, 63.0 rad m^{-2} from the top to bottom. The color shadows in the left panels indicate the wavelength coverage of ASKAP (red), GMRT (green) and LOFAR (blue). The wavelength range between $0.05 \leq \lambda^2 \leq 1$ m^2 dramatically changes as $\rm RM_{IGMF}$ changes because of multiple RM component depolarization. This range is covered by ASKAP and GMRT, while LOFAR only covers Faraday depolarization scale of the compact source. Looking at polarization angles (right panels), the long wavelength shows the linear relation between the polarization angle and λ^2 because this range only contain the compact source contribution. Actually, the slope $d\chi/d\lambda^2$ corresponds to the Faraday depth of the compact source. On the other hand, the short wavelength does not show simple features. Thus, Faraday depth can not be estimated from the slope.

Figure 5.7 shows results of the Faraday tomography (gray shadow) and Phase RM CLEAN (black line). The top panels plot the results by ongoing telescopes. The separation between two sources are smaller than $\Delta\phi_{\rm FWHM}$ of both ASKAP and GMRT for the case of top panels. Indeed, the reconstructed FDFs have only a single peak in result of GMRT. (However, one can notice that ASKAP resolves two peak in spite of poor resolution. It is just a coincidence (see Section 4.2)). Please note that many peaks in the FDF

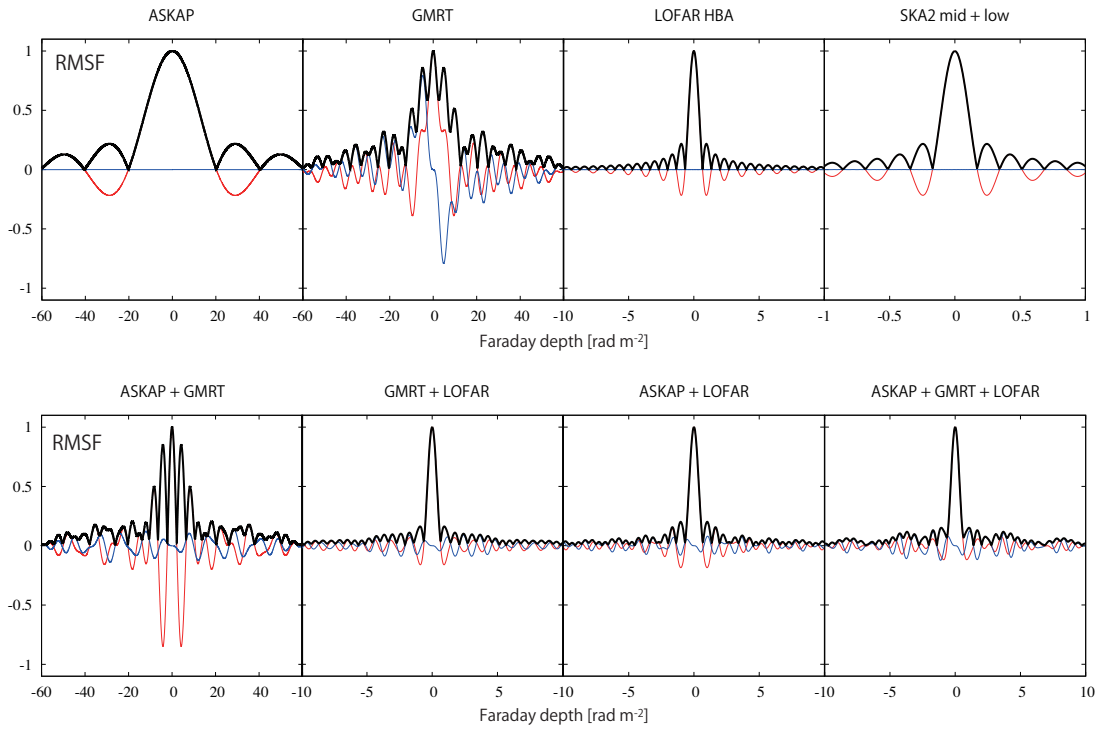

Figure 5.5: The RMSFs for adopted and combined observatories.

of ASKAP and GMRT are caused by RMSF, thus they are eliminated by RM CLEAN. GMRT can not measure the shift due to their poor resolution. Smaller resolution than separation between sources is indispensable for detection of the shift. On the other hand, the LOFAR has adequate $\Delta\phi_{\rm FWHM}$. However, as we mentioned before, the σ_ϕ for LOFAR is smaller than Faraday thickness of the diffuse source, thus LOFAR can detect only the compact source.

The middle panels and bottom center panels show the results by combined observations. We expected a synergy between ASKAP and LOFAR to recover reciprocal weakness. Indeed, reconstructed FDF likely to contain the diffuse and compact sources (see right panels). However, difficulty can be seen in the result of the RM CLEAN. Because of complexity of RMSF, RM CLEAN does not eliminate sidelobes completely. It must cause misinterpretation of the source distribution on the LoS. Other combinations also suffer the difficulty of RM CLEAN. Although we have expected that the wide wavelength coverage absolutely improves the results of Faraday tomography, that is not necessarily so. The improvement of results of Faraday tomography would require *continuous* wide band coverage which produces simple RMSF or improvement of deconvolution method. Finally, the bottom right panels displays the result by SKA2, which achieves continuous wide band coverage. As we expected, the result eliminates sidelobes completely and shows sufficiently resolved two peaks.

In Figure 5.8, we show detected sources as a function of $\rm RM_{IGMF}$. The gray boxes show

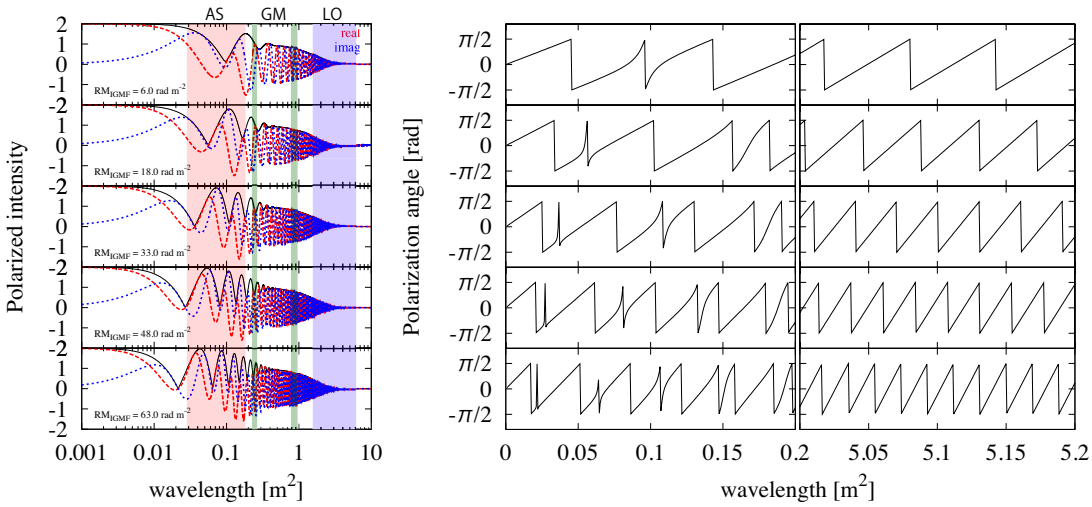

Figure 5.6: The polarized intensities (left) and polarization angles (right) for $\mathrm{RM_{IGMF}}$ = 6.0, 18.0, 33.0, 48.0, 63.0 rad $\mathrm{m^{-2}}$ from top to bottom. The color shadows in left panels indicate the wavelength coverage of ASKAP (red), GMRT (green) and LOFAR (blue).

the emitting regions and black points indicate the peak of this regions. Model is shown by blue dotted lines. Looking at ASKAP case, the CLEANed FDF is regarded as a single diffuse source at smaller $\mathrm{RM_{IGMF}}$, even if it has two peaks (compare with left top panels in Figure 5.7). At larger $\mathrm{RM_{IGMF}}$, however, two diffuse sources are detected and a *gap* between these sources also appeared. The smallest $\mathrm{RM_{IGMF}}$ at which the *gap* is appeared can be regarded as a detection limit of $\mathrm{RM_{IGMF}}$ for Strategy A. The CLEANed FDFs by GMRT+LOFAR (GL) are not stable and reproduce several sources at even large $\mathrm{RM_{IGMF}}$. Furthermore, ASKAP+LOFAR (AL) shows underestimation of thickness of the diffuse source. It could lead overestimation of $\mathrm{RM_{IGMF}}$. The poor reconstructions for both cases are caused by complexity of RMSF and difficulty of RM CLEAN. At the right bottom panel in Figure 5.8, the difference between estimated $\mathrm{RM_{IGMF}}$ and modeled $\mathrm{RM_{IGMF}}$ are plotted, $\Delta\mathrm{RM_{IGMF}} = \mathrm{RM^{model}_{IGMF}} - \mathrm{RM^{est}_{IGMF}}$. The case of the complete estimation, $\Delta\mathrm{RM_{IGMF}} = 0$, is shown by the black dotted line. Thus, data point above this line indicates overestimation and vice versa. We do not plot the case of ASKAP, GMRT, LOFAR and GL because $|\Delta\mathrm{RM_{IGMF}}|$ is too large for clear description for ASKAP and Faraday tomogrpahy can not estimate $\mathrm{RM_{IGMF}}$ for other cases. Thus, we just show AG (red), AL (green), AGL (blue) and SKA (magenta). AL and AGL can overestimate at smaller $\mathrm{RM_{IGMF}}$. The difficulty of Faraday thick source reconstruction can be seen. On the other hand, AG and SKA stably estimate reliable value at entire $\mathrm{RM_{IGMF}}$.

5.5.2 Strategy B

Next we move to discussion of strategy B. Basically, two situations for applying the strategy B can be considered, (1) source B and C are in a single beam or (2) they are

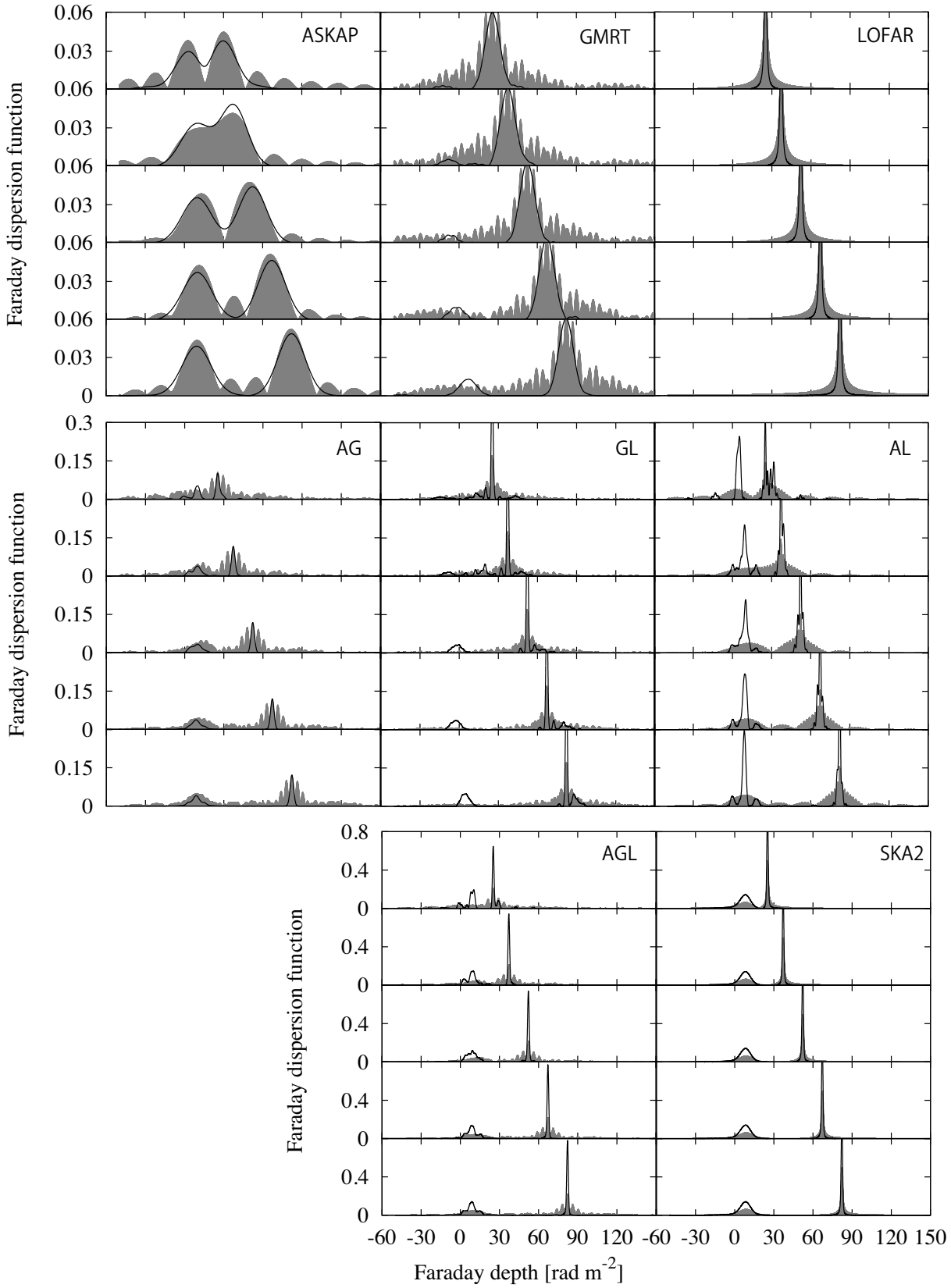

Figure 5.7: The result of the Faraday tomography (gray shadow) and RM CLEAN (black line).

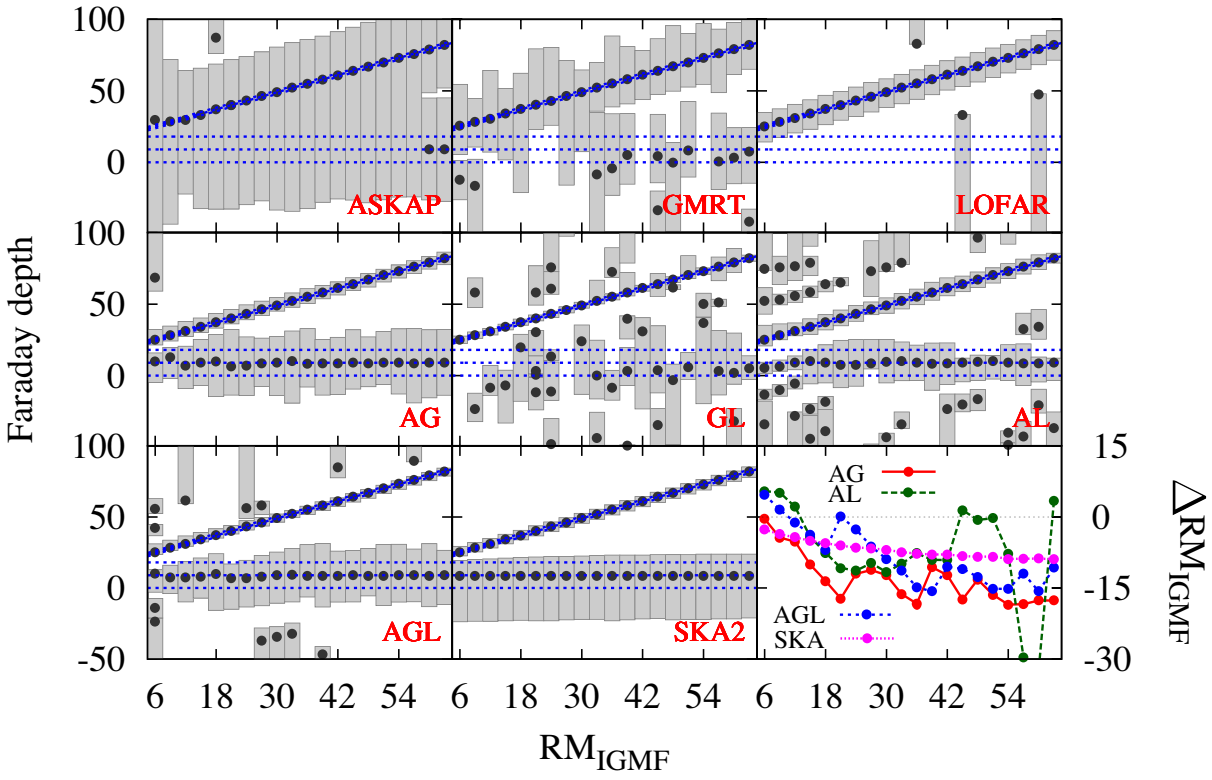

Figure 5.8: Detected peaks and edges of CLEANed FDFs. The emit regions are shown by gray boxes and peak is shown by black dot. Edges and peak of model is represented by blue dotted lines.

separated within ∼0.1 degrees. By former case, FDF has three peaks, which show source A, B and C. Then, RM_{IGMF} is estimated from the gap between source B and C. Of course, it should be confirmed that both source B and C are extragalactic sources. By latter case, RM_{IGMF} is also estimated from the gap between source B and C, but after subtraction of FDFs between LoSs for B and C. In this case, however, if one of LoSs has detectable RM_{IGMF} by Strategy A, it does not need to apply Strategy B anymore. Therefore, in this subsection, we just consider the cases with overlapped FDF. In this cases, RM_{IGMF} can not be detected by Strategy A.

We show the result of Strategy B. In the center panels of Figure 5.9, models of FDF are described. Also corresponding polarized intensities as shown in the left panels. As the compact source approaches to the diffuse source, amplitude of polarized intensity (black line) becomes smooth and losses unique feature because multiple RM component depolarization is suppressed. In the right panel, we show the ideal case of Strategy B. The top panels describe FDFs on the each LoS which observes source B and C, respectively. Both cases can not detect RM_{IGMF} by Strategy A. However, after the subtraction of one FDF from another, RM_{IGMF} between the compact sources is revealed by the subtraction

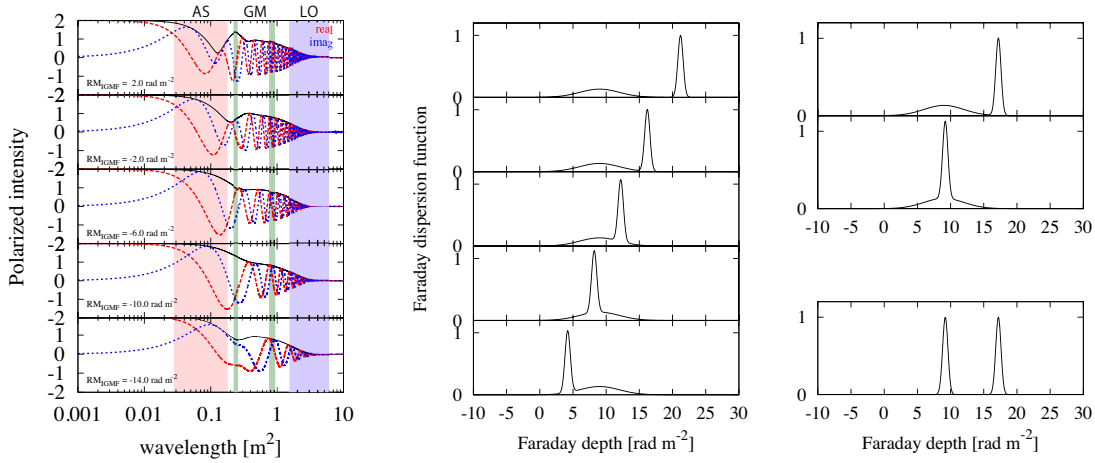

Figure 5.9: The polarized intensities (left) and Faraday dispersion function (center) overlapped cases. The color shadows in left panels are same with Figure 5.6. Right panel shows ideal case of Strategy B, difference between two top panels reveals $\mathrm{RM_{IGMF}}$ between compact sources (lower panel).

of only the diffuse source (lower panel).

The results of Faraday tomography are shown in Figure 5.10, the gray shadow and the black line indicate reconstructed FDFs and CLEANed FDFs, respectively. Then Figure 5.11 plots CLEANed FDFs after the subtraction. We fixed pivot LoS, in which both FDFs of the diffuse and the compact source have almost the same Faraday depth $\phi_c \sim \phi_d$. Then we subtract FDF having different ϕ_s from pivot LoS. We should mention that the subtraction can be done by two patterns, after CLEAN or before CLEAN. We carry out both patterns and compare each other. The gray shadows and the black lines indicate subtracted FDFs and CLEANed subtracted FDFs, respectively. The red lines represent the subtracted CLEANed FDFs. ASKAP and GMRT do not have enough resolution to resolve overlapped sources, thus FDFs having similar ϕ_c are almost canceled out. AG is also suffered by its poor resolution. Focusing on the observation providing small $\Delta\phi_{\mathrm{FWHM}}$, GL and AL are suffered by complex RMSF when CLEAN is carried out. Thus, the gap between compact sources is buried. Even if we adopt AGL or SKA, the detection of the gap seems to be quite difficult with this strategy (see the bottom panels in Figure 5.11) because of poor reconstruction of the Faraday thick source.

5.6 The Fisher analysis

In previous section, we investigated the detectable limit by Faraday tomography only. Unfortunately, detection limit for ongoing observatories and their combinations could not reach to expected RM of IGMF. However, some of observatories can estimate the number or type of sources. Therefore, we can construct the models of FDFs from results of

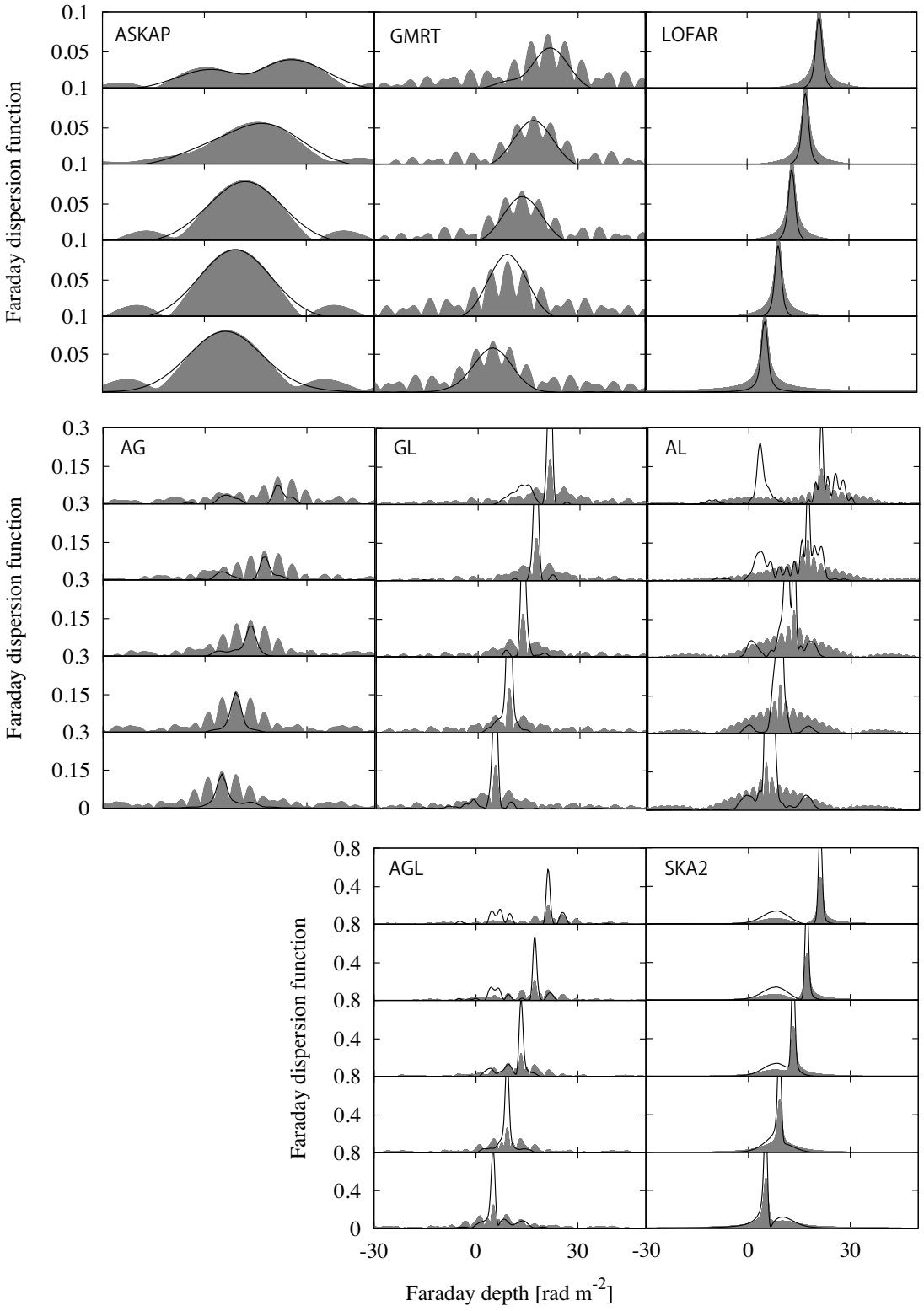

Figure 5.10: Same with Figure 5.7, but for overlapped cases.

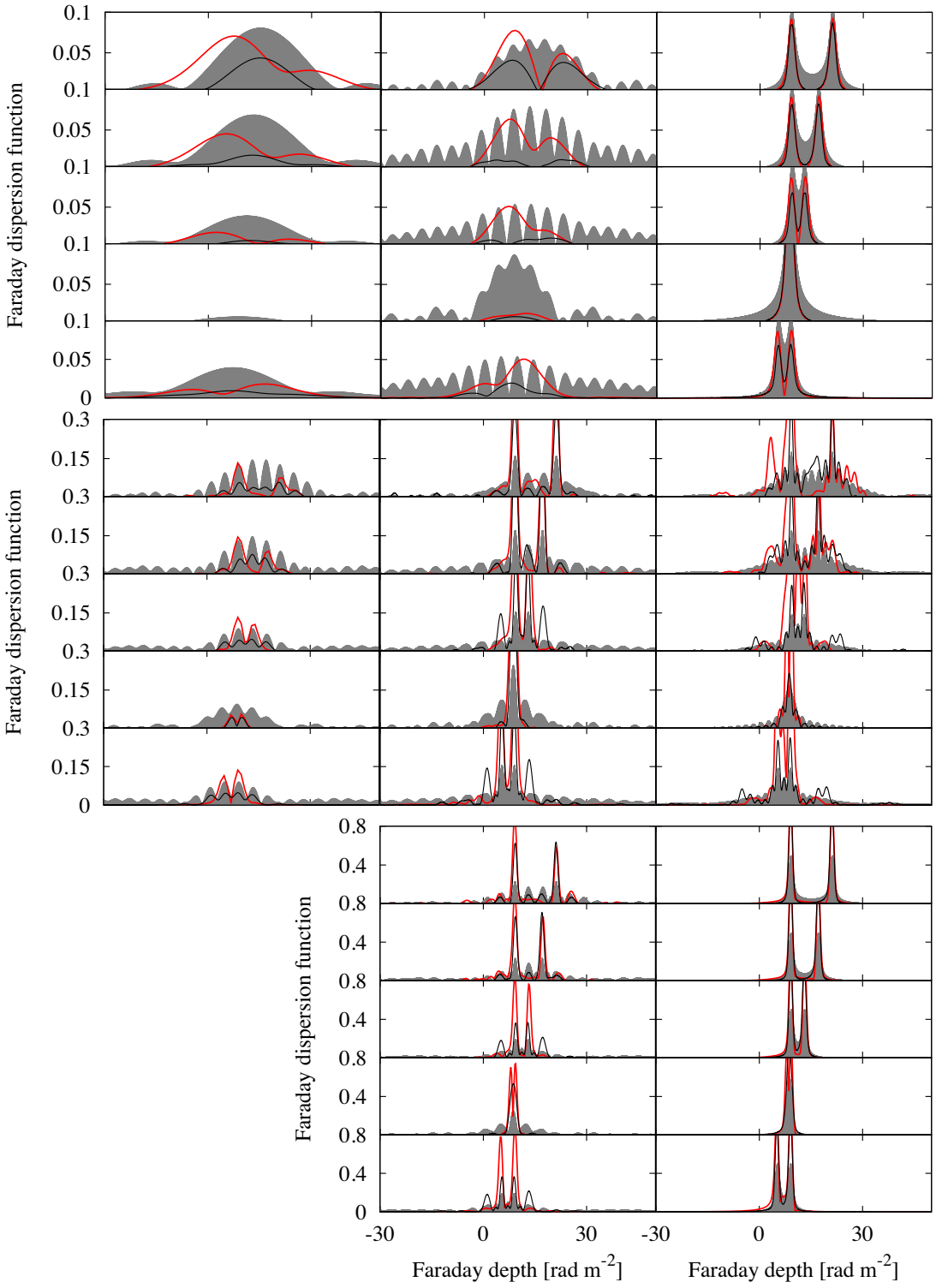

Figure 5.11: The results after subtraction. The black and red lines show CLEANed subtracted FDFs and subtracted CLEANed FDF, respectively.

Faraday tomography, then model fitting can be adopted to the IGMF detection. As we have seen in previous section, Strategy A is more efficient way rather than Strategy B. Thus, we inspect the detection possibility of RM caused by IGMF ~ 3 rad m^{-2} by only Strategy A.

Here, we validate how accuracy can be expected by sensitivities of each observatory when we adopt the model fitting. This estimate must be under a hypothesis that we did estimate the model function which well describes feature of FDFs on the LoS by Faraday tomography. The accuracy is calculated by variations of likelihood function $L(\vec{\theta})$ along each parameter θ_i, where i is index of parameters. This method is called the Fisher analysis. The Fisher matrix, $\mathcal{F}_{ij}$, contains this variations as elements

$$\mathcal{F}_{ij} \equiv -\left.\frac{\partial \mathcal{L}(\vec{\theta})}{\partial\theta_i \partial\theta_j}\right|_{\vec{\theta}=\vec{\theta}_{\rm true}} , \tag{5.4}$$

where $\mathcal{L}(\vec{\theta}) = -\ln L(\vec{\theta})$ is the log likelihood function.

From here, we estimate the likelihood function. The observed quantities $\tilde{Q}(\lambda^2)$ and $\tilde{U}(\lambda^2)$ can be written as,

$$\tilde{Q}(\lambda^2) = Q(\lambda^2) + n_Q(\lambda^2), \quad \tilde{U}(\lambda^2) = U(\lambda^2) + n_U(\lambda^2) , \tag{5.5}$$

where $Q(\lambda^2)$ and $U(\lambda^2)$ represent the true quantities and $n_Q(\lambda^2)$ and $n_U(\lambda^2)$ indicate the measurement noise on each channel. The measurement noise generally obeys a Gaussian probability function,

$$\mathrm{PDF}(n_i) = \frac{1}{\sqrt{2\pi}\sigma_{n_i}} \exp\left(-\frac{n_i^2}{2\sigma_{n_i}^2}\right) \quad \text{for} \quad i = Q,\, U , \tag{5.6}$$

where σ_{n_i} represents the root mean square (rms) of noise and now we assume $\sigma_{n_Q} = \sigma_{n_U} = \sigma_n$. Thus, the probability that we obtain the value $\tilde{Q}(\lambda^2)$ and $\tilde{U}(\lambda^2)$ does also obey the Gaussian probability function. It corresponds to the probability that we obtain the parameters $\vec{\theta'}$ describing $\tilde{Q}(\lambda^2)$ and $\tilde{U}(\lambda^2)$. Then,

$$\mathrm{PDF}(\vec{\theta'}) = \exp\left(-\frac{1}{2}\chi^2\right) \tag{5.7}$$

$$\chi^2 = \frac{\left(\tilde{Q}(\lambda^2;\vec{\theta'}) - Q(\lambda^2;\vec{\theta}_{\rm true})\right)^2 + \left(\tilde{U}(\lambda^2;\vec{\theta'}) - U(\lambda^2;\vec{\theta}_{\rm true})\right)^2}{\sigma_n^2} . \tag{5.8}$$

The Bayes' theorem can be adopted when the probability function can be described by a Gaussian function, thus likelihood function would be proportional to the probability giving the best fit parameters, i.e. $L(\theta) \propto \mathrm{PDF}(\theta)$. Thus, Equation (5.4) reduces

$$\mathcal{F}_{ij} \equiv -\left.\frac{\partial \mathcal{L}(\vec{\theta})}{\partial\theta_i \partial\theta_j}\right|_{\vec{\theta}=\vec{\theta}_{\rm true}} = \frac{1}{2}\left.\frac{\partial \chi^2}{\partial\theta_i \partial\theta_j}\right|_{\vec{\theta}=\vec{\theta}_{\rm true}} . \tag{5.9}$$

Table 5.3: Parameters related to sensitivity

Observatory	Frequency (GHz)	$T_{\rm sys}$ (K)	$A_{\rm eff}$ (m^2)
LOFAR HBA[1]	0.120–0.240	–	–
GMRT 327[2]	0.305–0.345	106	30,000
GMRT 610[2]	0.580–0.640	102	30,000
ASKAP[3]	0.700–1.800	50	4,072

[1] LOFAR page; http://www.astron.nl/radio-observatory/astronomers/lofar-astronomers
[2] http://www.ncra.tifr.res.in/ncra/gmrt/gmrt-users/observing-help-for-gmrt-users/manual-2012.pdf/at_download/file and [80]
[3] ASKAP page; http://www.atnf.csiro.au/projects/askap/

The rms of measurement noise, σ_n, corresponds to the sensitivity of observatories. For ASKAP and GMRT, the sensitivity at each channel is calculated by

$$\sigma_n^2 = \frac{k_B T_{\rm sys}}{A_{\rm eff}\sqrt{t_{\rm obs}\delta\nu}} \ , \tag{5.10}$$

where k_B is the Boltzmann constant and $t_{\rm obs}$ is the integrated time in unit of second. The band width $\delta\nu$ in Hz, effective area $A_{\rm eff}$ in m^2 and system temperature $T_{\rm sys}$ in K for each observatory is shown in Table 5.3. For LOFAR, the sensitivities for each channel are given by LOFAR website [1].

5.6.1 Results with ongoing observatories

Figure 5.12 shows the 95% confidence regions assuming GMRT (green) and ASKAP (red). From the top to bottom panels, y–axes are set with $\delta\phi_c$, f_c, χ_{0c}, ϕ_d, $\delta\phi_d$, f_d and χ_{0d}, respectively. From the left to right, x–axes are set with ϕ_c, $\delta\phi_c$, f_c, χ_{0c}, ϕ_d, $\delta\phi_d$, and f_d, respectively. For example, the left top panel shows the projected inverse Fisher matrix to ϕ_c–$\delta\phi_c$ plane. The case of LOFAR could not be estimated confidence regions because LOFAR is insensitive of the diffuse source due to Faraday depolarization. As we expected, no observatory can estimate parameters very well. Most of parameters estimation require over 100% error. As error for estimation of $\rm RM_{IGMF}$, 10.23 and 57.26 rad m^{-2} (95% C.L.) is estimated by ASKAP and GMRT, respectively. That means that several 10 rad m^{-2} as $\rm RM_{IGMF}$ is required to detect by ongoing observatories at least. However, for the sake of forecast of combined observations, we here refer to just trends of each observatory.

[1] http://www.astron.nl/radio-observatory/astronomers/lofar-imaging-capabilities-sensitivity/sensitivity-lofar-array/sensiti

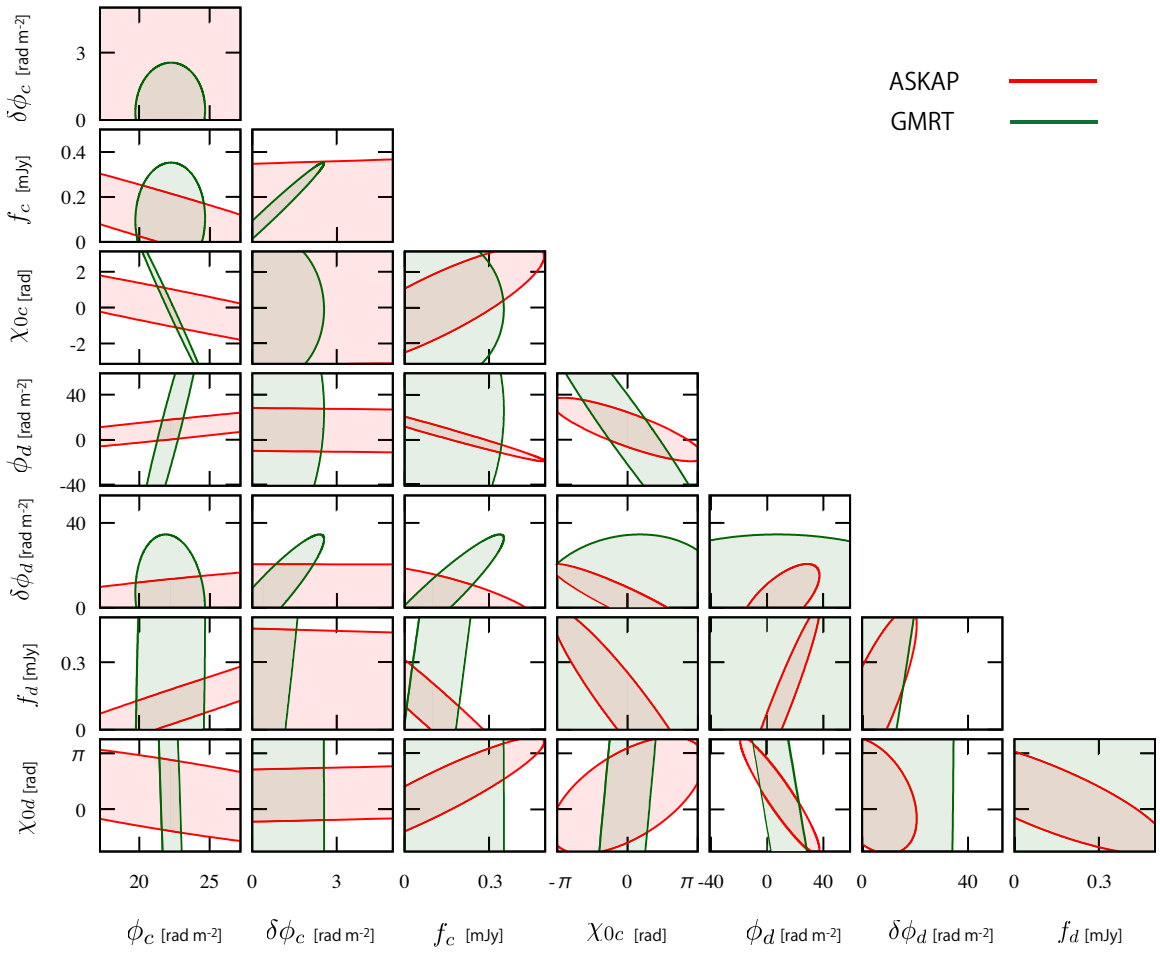

Figure 5.12: The 95% confidence regions estimated by the Fisher information matrix with ASKAP (red) and GMRT (green).

ASKAP is able to estimate parameters of the diffuse source relatively (see right bottom 6 panels). Since it just covers depolarization scale of the diffuse source ($\lambda^2 \sim 0.1$ m^2, see Figure 5.4), parameters for the diffuse source are determined. However, dumped feature due to oscillation by multi component depolarization (see left and right panels in Figure 5.4) causes overestimation of Faraday thickness $\delta\phi_d$, since ASKAP can not determined whether this dumping feature comes from Faraday depolarization or multi component depolarization due to lack of long wavelength range. This lack of long wavelength range causes poor parameter estimation of the compact source, see the left top 6 panels. Therefore, combinations with observatory covering long wavelength range, e.g. LOFAR, would be a significant synergy and be expected to provide good parameter estimation of both the diffuse and compact sources as well as $\mathrm{RM_{IGMF}}$.

In spite of narrow coverage, GMRT is able to estimate the compact source parameters.

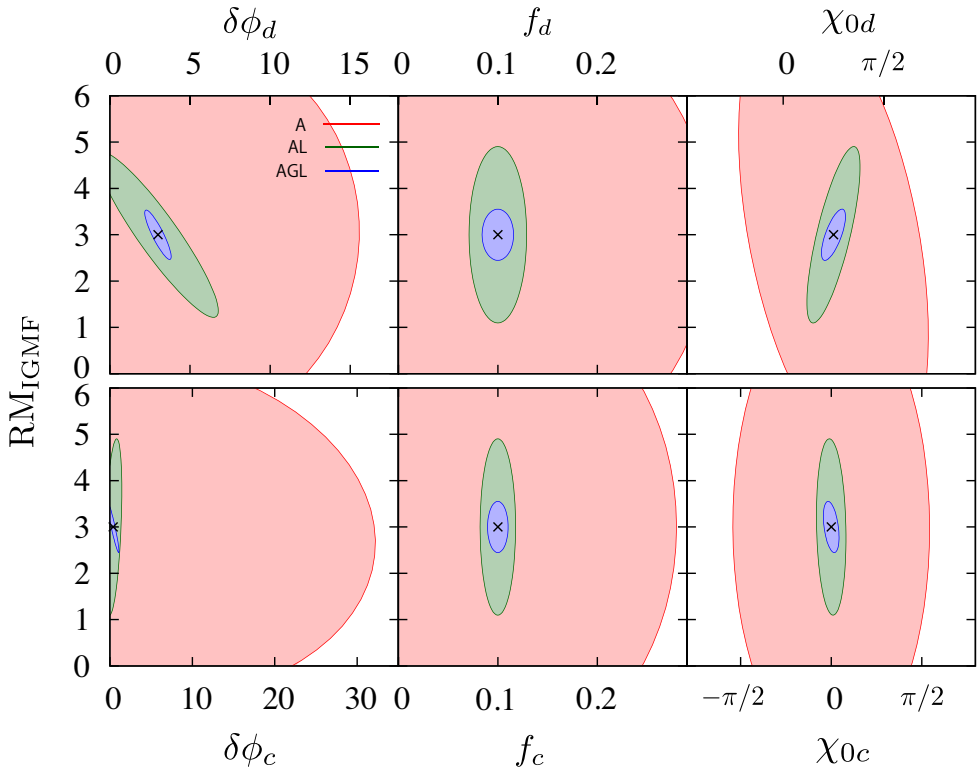

Figure 5.13: The 95% confidence regions estimated by Fisher information matrix with ASKAP (red), ASKAP+LOFAR (green) and ASKAP+GMRT+LOFAR (blue).

GMRT 327 just covers depolarization scale of the compact source, $\lambda^2 \sim 1$ m^2, where mainly contains component of the compact source because one of the diffuse source is already depolarized at $\lambda^2 > 1$ m^2. Also, GMRT 610 covers wavelength which still contains the diffuse component and allows us to estimate the $\mathrm{RM_{IGMF}}$. The expected huge error on $\mathrm{RM_{IGMF}}$ is mainly caused by narrowness of coverage and lack of short wavelength coverage, thus combinations with both ASKAP and LOFAR are required for dramatical improvement of the estimation.

A reason of the worst result by LOFAR is obvious. That is because that the diffuse source is invisible for LOFAR and it is impossible to identify the edges of the diffuse source. The wide coverage of λ^2 domain by LOFAR allows us to identify parameters of the compact source, thus a synergy with ASKAP must be extremely efficient.

5.6.2 Improvement of results by combined observations

In order to see how much RM due to IGMF is constrained, we take $\mathrm{RM_{IGMF}}$ as an independent variable instead of Faraday depths. Figure 5.13 shows the 2–σ confidence ellipses. The y axis denotes the $\mathrm{RM_{IGMF}}$ and x axes denote Faraday thicknesses, amplitudes and the intrinsic polarization angles for the diffuse (top panels) and the compact source (bot-

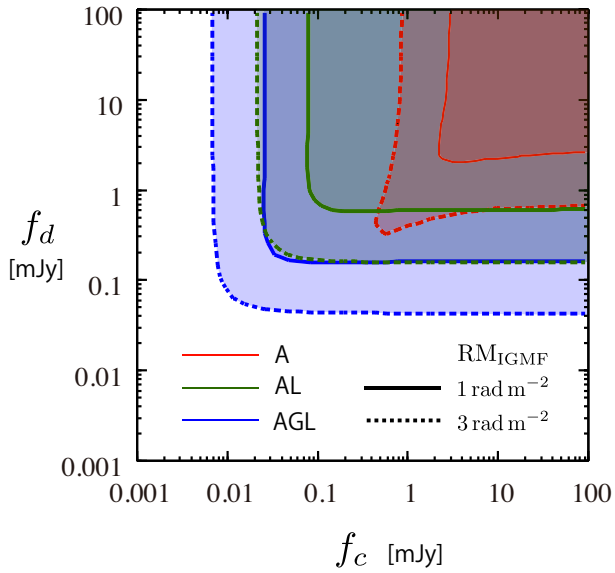

Figure 5.14: Intensities of source for the IGMF to be detected with 3–σ significance. Two cases with $\mathrm{RM_{IGMF}} = 1.0$ rad m^{-2} (solid lines) and 3 rad m^{-2} are shown. In shaded areas, the IGMF is detected more than 3–σ significance.

tom panels), respectively. The red, green and blue represent the result of ASKAP only (A), ASKAP+LOFAR (AL) and ASKAP+GMRT+LOFAR (AGL), respectively.

We saw that pairs of parameters are more or less correlated each other in Figure 5.12, and the confidence region is improved when we consider combined observations. For example, $\delta\phi_c$ is hardly determined by the observation with ASKAP alone. Because $\delta\phi_c$ is one of the parameters which defines the IGMF, it implies that ASKAP itself cannot well constrain $\mathrm{RM_{IGMF}}$. This weak constraint by ASKAP is ascribed to the fact that short wavelength observations cannot resolve small scale structures in ϕ space. Actually, the parameter degeneracy and the constraint on $\delta\phi_c$ are dramatically improved by the additions of longer wavelength observations such as GMRT and LOFAR.

For ASKAP alone, the error is so large that zero IGMF ($\mathrm{RM_{IGMF}} = 0$) is not excluded at 1–σ significance. When we combine LOFAR with ASKAP, the situation drastically improves and zero IGMF can be excluded with about 2–σ significance. By the full combination of ASKAP, LOFAR and GMRT, the significance increases up to about 6–σ. Thus, combinations of these telescopes are very effective to probe the IGMF. Other parameters are also well determined by the combination of the observatories, within 20% for most of them. Only $\delta\phi_c$ can not be determined well even by the combination. This is because of the lack of the sensitivity at long wavelengths where both sources become very dim due to the Faraday depolarization.

5.6.3 Required intensities to detect the IGMF

We next consider general cases for various FDF models. We focus on some essential parameters to study the possibility of detecting the IGMF. Specifically, we examine the condition on the source intensities that the IGMF can be detected by our method. We vary the three parameters, f_d, f_c and ϕ_c, and fix the other five parameters, $\phi_d = 9.0$ rad m^{-2}, $\delta\phi_{\rm d} = 3.0$ rad m^{-2}, $\chi_{0d} = 0$ rad, $\delta\phi_c = 0.4$ rad m^{-2}, and $\chi_{0c} = \pi/4$ rad (same as the previous section). Varying ϕ_c is equivalent to varying $\mathrm{RM_{IGMF}}$ for the fixed ϕ_d, $\delta\phi_d$, and $\delta\phi_c$, according to Equation (5.3).

Figure 5.14 shows the regions on f_c-f_d plane where non-zero IGMF is detected by 3-σ significance for a given $\mathrm{RM_{IGMF}}$ value, that is, 3-σ error in $\mathrm{RM_{IGMF}}$ is smaller than the value of $RM_{\rm IGMF}$ itself. Two cases with $\mathrm{RM_{IGMF}} = 1.0$ and 3.0 rad m^{-2} are plotted for each combination of the telescopes. In general, brighter sources are necessary for a smaller value of $\mathrm{RM_{IGMF}}$. In the case with $\mathrm{RM_{IGMF}} = 1.0$ rad m^{-2}, we need much brighter (by a factor of ten) sources compared with the case with $\mathrm{RM_{IGMF}} = 3.0$ rad m^{-2} and the combination of the telescopes are very effective. On the other hand, in the case with $\mathrm{RM_{IGMF}} = 3.0$ rad m^{-2}, even ASKAP alone can detect IGMF with relatively faint sources (~ 1 mJy).

Chapter 6

Discussion

In this chapter, we summarize the arguments and future works that we could not state in each chapter.

6.1 Faraday Tomography and RM CLEAN

6.1.1 Interpretation of multiple signals

We first start to discuss about Faraday tomography and RM CLEAN themselves. For the case with Faraday thin sources, we can estimate not only the Faraday depth, but also the intrinsic polarization angle of sources. Since the Faraday depth reflects the strength of magnetic fields parallel to the LoS and the intrinsic polarization angle tells us the mean direction of the magnetic field (mainly the regular field) projected to the sky, we can obtain the 3–dimensional structure of magnetic fields. In particular, the estimation of intrinsic polarization angles for each signal is meaningful. When Faraday tomography resolves multiple Faraday components in Faraday depth domain from observation of a spatially single source, interpretation is needed, e.g. whether they are in a single source or different sources located at different distance. The Faraday components having almost the same intrinsic polarization angles seem to support former interpretation because the same polarization angle might be caused by the regular field in the source. Then RM between signals can be considered as contribution from magnetic fields inside of a source. On the other hand, signals having different intrinsic polarization angles seem to support latter interpretation, then RM between Faraday components can be regarded as magnetic fields between sources.

6.1.2 Poor reconstruction of Faraday thick sources

However, we could not reconstruct Faraday thick sources very well. The poor reconstruction might be caused by both problems within the Faraday tomography and the RM CLEAN. From point of view of the Faraday tomography, main differences between the Faraday thin and thick source is effect of the Faraday depolarization. Thus the observation

of depolarization scale is a key for thick source reconstruction. Therefore, incompleteness of observable wavelength and wavelength range significantly affect the quality of reconstruction. Furthermore, Faraday depolarization can not dominate when multiple RM components exist on a LoS, as we saw in Chapter 5. This fact could make reconstruction more difficult. We next move to the point of view of the CLEAN. The CLEAN method imposes some assumptions. It can be considered that Faraday thick sources do not satisfy an assumption "sources are sparse enough". The CLEAN method regards the Faraday thick source as a lump of Faraday thin sources. Therefore, convolved Faraday thin sources affect each other, and conflict when the RMSF is subtracted. This effect could be significant by complex RMSF which can be seen from poor reconstruction by combined observation in Chapter 5. Attempts for the improvement of CLEAN to Faraday thick source have been studied in radio imaging field [81, 82]. The application of these algorithms to RM CLEAN is very interesting.

6.2 Exploring the IGMFs

6.2.1 Effect of measurement noise

We here investigate the effect of measurement noise. We assume the PDF of measurement noise as a Gaussian distribution with a standard deviation σ_n^i for ith channel. Using σ_n^i, signal-to-noise ratio (S/N) can be defined as

$$\frac{S}{N} = \frac{\sqrt{(2N)^{-1}\sum_{i=1}^{N}[Q(\lambda_i^2)^2 + U(\lambda_i^2)^2]}}{\sqrt{N^{-1}\sum_{i=1}^{N}(\sigma_n^i)^2}}\ , \tag{6.1}$$

where N indicates the number of channels. Here we assume a common standard deviation σ_n for all channels for simplification. We discuss in terms of S/N instead of σ_n.

The left panels in Figure 6.1 show the polarized intensities with the measurement noise by black solid lines. The red dotted lines represent the polarized intensities without the measurement noise. From the top to bottom panels, the cases with $S/N = 4$, 16 and 64 are displayed. The right panels show the CLEANed FDFs for each S/N. From the left to right panels, ASKAP only, AGL and SKA are adopted, respectively. For comparison, the results without the measurement noise are also plotted by red dotted lines. Looking at the case of ASKAP, the effect of the measurement noise is smoothed out and it is not significant even if S/N is so small, e.g. $S/N = 4$. On the other hand, SKA suffers from the effect of noise. In particular, the effect disturbs the detection of edges of FDFs by producing small amplitude spikes which bury the gap caused by $\mathrm{RM_{IGMF}}$. The value of S/N which provides negligible effect on the CLEANed FDF seems to be larger than several dozens for SKA.

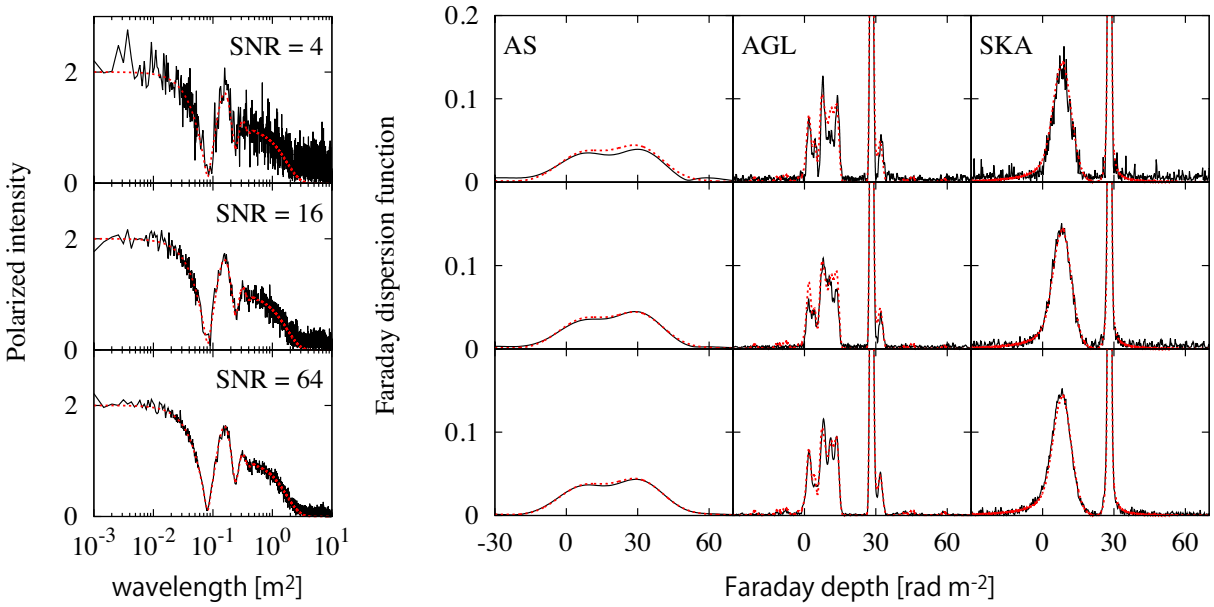

Figure 6.1: The polarization intensities with measurement noise (left panels) and CLEANed FDFs with ASKAP alone, AGL and SKA2 (right panels). From top to bottom, the cases of $S/N = 4$, 16 and 64 are plotted, respectively.

6.2.2 The definition of "edge" of sources

We assumed several simplifications for exploring the IGMF in Chapter 5, e.g. the shape of FDF of sources and definition of edges. Both are critical and difficult points for this thesis. Several definitions of edges are used by other fields, e.g. Petrosian radius or Kron radius, in order to measure the size of galaxies. However, as long as we know, both are heuristic definitions, and theoretically motivated definitions of edge of galaxies do not exist. According to the study of Galactic FDF, the FDF does not reduce smoothly but sometimes forms sharp structure at the edge [83]. Therefore, we need to understand the structure of the Galaxy and Galactic FDF in more detail. Then, re-examinations of both Strategy A and B with realistic Galactic FDF instead of simple model are very important.

6.2.3 On/Off–set observation

The Galactic FDF sometimes has several peaks. They can lead misunderstanding of the structure on the LoS, e.g. whether peaks are originated in the Galaxy or galaxies. Thus, we need to make sure the shape of the Galactic FDF on the LoS. One of ideas to distinguish the shape of Galactic FDF is the *on–set/off–set observation*. On–set means observation of a LoS including both background sources and the Galaxy, while Off–set means that including only Galaxy. If both LoSs are close enough, LoSs share FDF of the Galaxy. The shape of Galaxy, such as the number of preks or thickness, can be revealed by off–set observation, then compare with on–set observation. However, how the Galactic

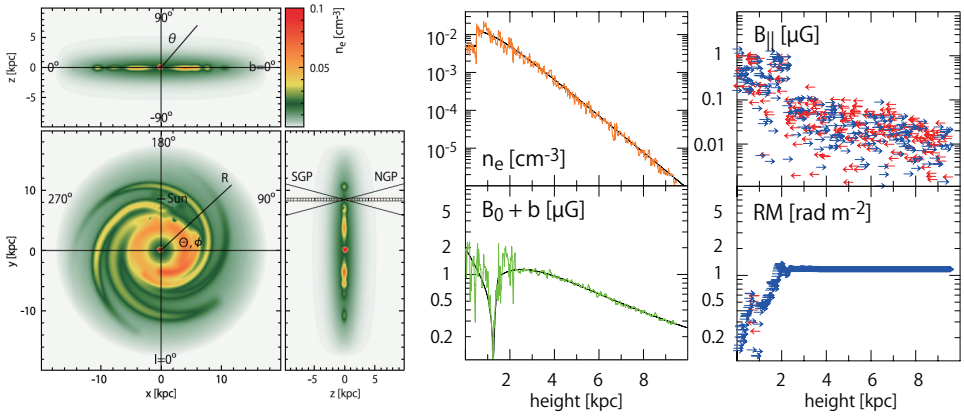

Figure 6.2: The electron density distribution of simulation (left panel) and profiles of quantities related with electron density and magnetic fields from the Sun toward Galactic pole (right panels).

FDF varies along the separation angle between LoSs is not unraveled so far (Note that Figure 5.2 shows just difference of RM). Thus, the evaluation of the on/off–set observation efficacy should be in future tasks.

6.3 Faraday dispersion function of the Galaxy

As we said many times, understanding of the shape of Galactic FDF is the most important task for our work. Ideguchi et al. (2014b) calculated the Galactic FDFs based on the simulation containing regular and turbulent magnetic fields which was carried out by Akahori et al. (2013) [83, 77]. Although they simulated only the region nearby solar system (500pc×500pc×20pc centered at solar system), it is useful enough for representing our Galaxy. As a model of the global electron density, the NE2001 model is employed [84, 85]. For the global magnetic fields, the axisymmetric spiral (ASS) or bisymmetric spiral (BSS) model were introduced by Sun et al. (2008) [86]. However Akahori et al. just assumed the ASS model. In addition, the halo dipole poloidal magnetic field near the Earth is assumed [87]. The random components are modeled by magnethydrodynamics (MHD) simulation [88]. The electron density distribution can be seen at the left panels in Figure 6.2 and profiles of magnetic fields and RMs are shown at the right panels.

The calculated FDFs are shown in Figure 6.3. All FDFs has same model parameters, e.g. scale heights of relativistic and thermal electron and the strength of the halo dipole poloidal magnetic field, but different turbulent magnetic fields. Looking at this figure, we cannot find any universal shape of the FDF, even if common model parameters are adopted. The random walk process by turbulent fields confuses the contribution from the regular field. Furthermore, this complexity of Galactic FDFs indicates that it would not be described by simple elementary functions, like Gaussian or top hat function.

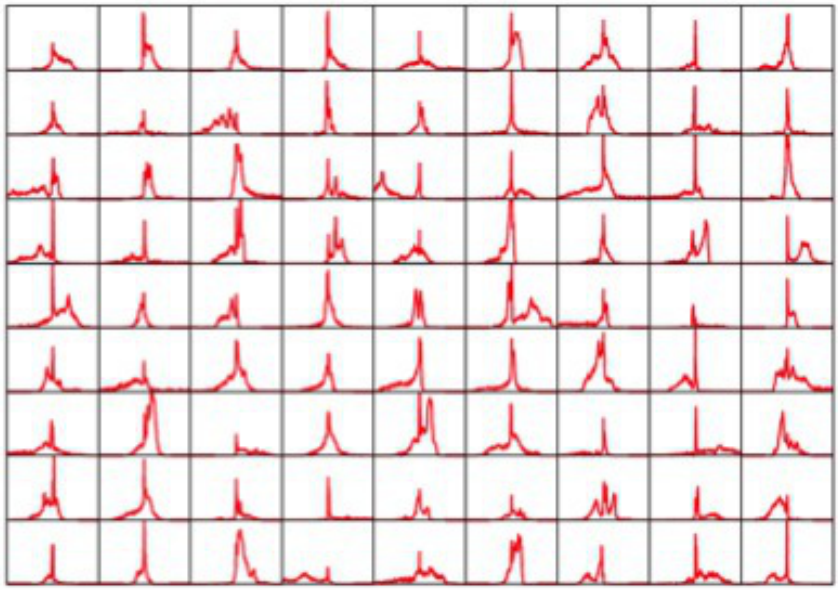

Figure 6.3: The FDFs calculated by simulation of Galaxy. x– and y–axis show the Faraday depth and amplitude of FDF, respectively. Each FDF is calculated with same model parameters, but different turbulent realization.

In order to somehow distinguish the dependences on model parameters, Ideguchi et al. introduced statistical quantities, such as variance, skewness and kurtosis. Then they calculated and compared the PDFs of all statistical quantities. It can be imagined that the variance depends on the existence of the regular field and the scale height of thermal electrons, because the regular field always piles up RMs and large scale height of thermal electrons extends the effective area to accumulate RMs. The regular field may cause asymmetry of FDF as well, then the RMs tend to be positive when the regular field points to observer and vice versa. According to their calculations, the PDF of standard deviation indeed shows the prediction, namely, larger standard deviation is expected for the case with the strong regular field or higher scale height of thermal electron (see Figure 6.4). Their results could imply an ability to refer to model parameters from statistics quantities of FDF. Furthermore, the relation between statistical parameters can be also utilized for model parameter prediction.

6.3.1 Reconstruction by the Faraday Tomogrpahy

In previous work, the authors just used true Galactic FDFs. However, we never obtain true Galactic FDFs. In this section, therefore, we investigate how the Faraday tomography can reconstruct the Galactic FDFs, especially statistic quantities of FDF, by future survey. We just demonstrate by SKA2 and employ the same model parameter sets with prior work (see Table 6.1). The statistic quantities, i.e. mean μ, standard deviation σ, skewness κ_3

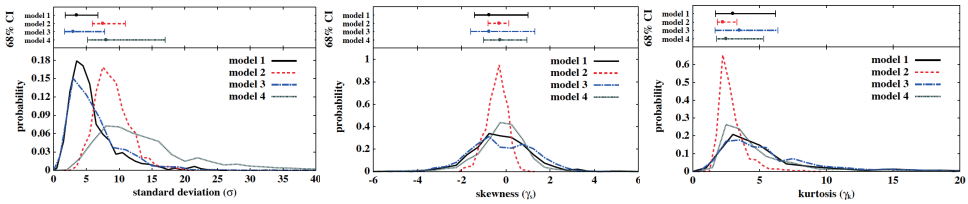

Figure 6.4: Comparison of PDFs of statistical quantity, standard deviation (left), skewness (center) and kurtosis (right), of Galactic FDFs. Model 1–4 is shown in Table 6.1. [83].

Table 6.1: Model parameters of simulation of Galaxy

	vertical magnetic field (μG)	cosmic electron scale height (kpc)	thermal electron scale height (kpc)
Model 1	0.0	1.0	1.0
Model 2	1.0	1.0	1.0
Model 3	0.0	3.0	1.0
Model 4	0.0	1.0	3.0

and kurtosis κ_4, are derived as,

$$\mu = \frac{\sum_{i=1}^{N} |F(\phi_i)|\phi_i}{\sum_{i=1}^{N} |F(\phi_i)|} \tag{6.2}$$

$$\sigma^2 = \frac{\sum_{i=1}^{N} |F(\phi_i)|(\phi_i - \mu)^2}{\sum_{i=1}^{N} |F(\phi_i)|} = \frac{\sum_{i=1}^{N} |F(\phi_i)|\phi_i^2}{\sum_{i=1}^{N} |F(\phi_i)|} - \mu^2 \tag{6.3}$$

$$\kappa_3 = \frac{\sum_{i=1}^{N} |F(\phi_i)|(\phi_i - \mu)^3}{\sigma^3 \sum_{i=1}^{N} |F(\phi_i)|} = \frac{\sum_{i=1}^{N} |F(\phi_i)|\phi_i^3}{\sigma^3 \sum_{i=1}^{N} |F(\phi_i)|} - 3\frac{\mu}{\sigma} - \left(\frac{\mu}{\sigma}\right)^3 \tag{6.4}$$

$$\kappa_4 = \frac{\sum_{i=1}^{N} |F(\phi_i)|(\phi_i - \mu)^3}{\sigma^4 \sum_{i=1}^{N} |F(\phi_i)|} = \frac{\sum_{i=1}^{N} |F(\phi_i)|\phi_i^4}{\sigma^4 \sum_{i=1}^{N} |F(\phi_i)|} - \frac{4\mu\kappa_3}{\sigma} - 6\left(\frac{\mu}{\sigma}\right)^2 - \left(\frac{\mu}{\sigma}\right)^4 , \tag{6.5}$$

respectively. The previous work did not mention about μ, but we do mention because μ, which means Faraday depth of FDF, is one of the most important quantities showing a property of the FDF. We do not take measurement noise into account, in order to investigate the capability of the Faraday tomography.

We first show the results of the Faraday tomography in Figure 6.5. The gray and color shadows represent the original and CLEANed FDFs. We show FDFs for model 1–4, from the top to bottom with different color. From the left to right, we just pick up four different turbulence realizations. Faraday tomography with SKA seems to provide good reconstructions except for Model 4 (magenta).

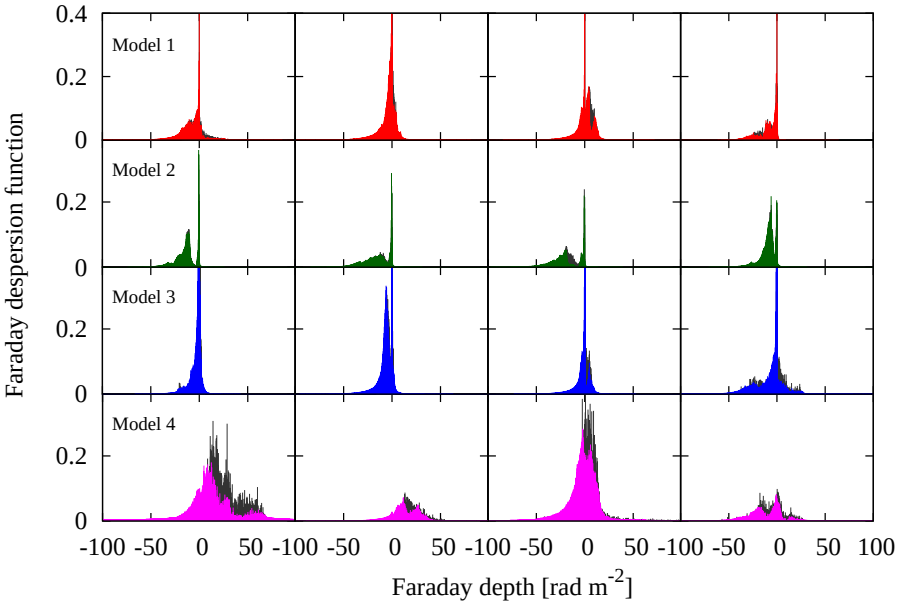

Figure 6.5: Results reconstructed by SKA. Model 1–4 are shown from the top to bottom with four different realizations. The gray and color shadows represent the original and CLEANed FDFs.

Next we focus on the reconstructions of statistical quantities. Figure 6.6 shows comparisons of histograms of statistical quantities between original and CLEANed FDFs. The gray and color histograms represent that of original and CLEANed FDF, respectively. The left top panels show histograms of μ value. All models shows good agreement with original histogram, as well as κ_3 (the left bottom panels) and κ_4 values (the right bottom panels). However, all histograms of the standard deviation of CLEANed FDFs do not correspond to that of original FDFs, which are totally shifting to large value. We think that this effect might be shown in previous chapter. FDFs would be thicker than true thickness due to convolution with RMSF. If this assumption is correct, it means that the effect of the convolution could not be negligible, even if $\Delta\phi_{\mathrm{FWHM}}$ is adequately smaller than thickness of FDF. This should be inspected by the dependency of shift on $\Delta\phi_{\mathrm{FWHM}}$, but it is out of this work.

6.3.2 Noise effect and choice of CLEAN parameters

We saw that the Faraday tomography provides reliable reconstructions of the Galactic FDFs. However, we did not take measurement noise into consideration. As we seen in Section 6.2.1, the CLEANed FDF reconstructed by SKA suffers from noise due to its high resolution. Hence, noise effect on reconstruction of statistical quantities should be clarified. Furthermore, we carried out RM CLEAN with just a set of CLEAN parameters. Because we calculate higher order moments, such as skewness or kurtosis, the effects

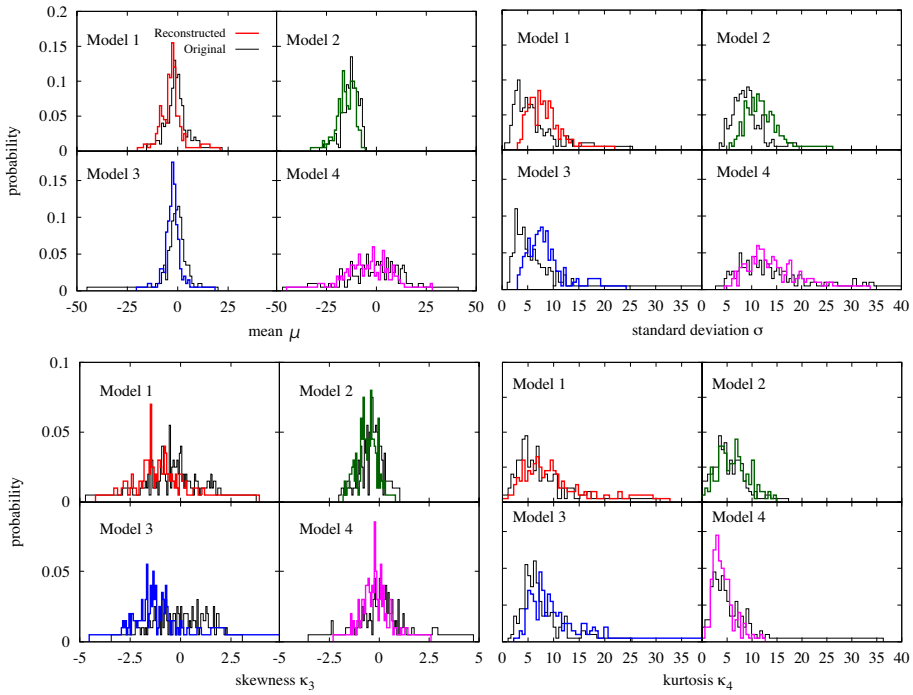

Figure 6.6: The comparisons of histogram of statistical quantities betwen original and CLEANed FDFs.

from large Faraday depth could not be negligible even if amplitude is visually small. The iteration number or threshold could affect to estimate of higher order statistical quantities. The too much iteration number causes overestimation of quantities because Faraday components are appeared at large Faraday depth. On the other hand, the too small iteration number could cause underestimation because RM CLEAN does not carry out deconvolution enough. Thus, an optimal parameter set can exist for statistical quantities estimation.

6.3.3 Extend to Magnetism Morphology

In this thesis, we just employed four Galaxy models and they have almost the same magnetism structure, such as the axisymmetric spiral field and the halo poroidal field. The classification of structures of the GMF is still an open problem. A study of the three dimensional magnetism structures is the most expected part for Faraday tomography. Therefore, the applications of Faraday tomography to more various magnetism models are very interesting. Therefore, the estimation of intrinsic polarization angles for Faraday thick source is absolutely necessary. Finally we wish to obtain the intrinsic polarization angle as a function of the Faraday depth.

Also, we used just the small region of Galaxy around solar system. In order to investigate the global structure of the GMF, global MHD simulations of galactic gaseous disk

need to be adopted, e.g. Ref. [89].

Chapter 7

Summary and Conclusion

A study of cosmic magnetism was started by discovery of magnetic fields in sunspots about a hundred years ago, then advanced with development of radio astronomy. In particular, synchrotron radiation from charged particles moving with relativistic speed in a magnetized region provide us numerous discoveries of magnetic fields associated with astronomical objects. Its intensity and direction of polarization tell us the strength and direction of magnetic fields in regions emitting synchrotron radiation. The polarization of synchrotron radiation provides not only information of direction, but also the strength of magnetic fields parallel to the line of sight (LoS) by the Faraday rotation effect. The polarization plane is rotated during traveling through the magneto-ionic media. The rotation degree is proportional to the square of the wavelength. The coefficient of this relation is called the rotation measure (RM) which includes strength of magnetic fields on the LoS. The synchrotron radiation dominates at a radio frequency, i.e., MHz $\sim$ GHz, and is significantly affected by Faraday rotation. That is why studies of cosmic magnetism have been developed with radio astronomy.

We first showed the development of a method to explore the structure of magnetic fields on the LoS, called the Faraday tomography. Generally speaking, we can only obtain integrated RM along the LoS. With RM, therefore, we cannot distinguish Galactic or extragalactic components. However, Faraday tomography allows us to obtain the RMs of each component on the LoS. Distribution of RM components on the LoS is called the Faraday dispersion function (FDF). Although it has been suggested in 1966 by Burn [66], it was not utilized very much because it requires a wide band radio observation. Recently, its potential uses are elevated by newly built radio telescopes and future projects, such as Australian SKA pathfinder (ASKAP), Low Frequency Array (LOFAR) and Square Kilometre Array (SKA), which satisfy demands of Faraday tomography, i.e., wide band radio observations.

In this thesis, we first investigated the RM ambiguity of Faraday tomography which was first time suggested by Farnsworth et al. (Ref. [68]). This ambiguity appears when there are multiple sources on the LoS within an angular resolution of the observation. If the intrinsic polarization angle and total Faraday rotation on the LoS of each source is within a certain angle, we can confound these sources. Due to this RM ambiguity, Faraday

tomography generates *false signals* which cause under/overestimate of the number of components on the LoS. Here we found that the RM ambiguity occurs when the angles of rotated polarization of the far side source and the near side is within $\sim \pm 10^{\circ}$. In this case, it seems difficult to distinguish whether the polarized emission comes from a single source or multiple sources. Thus we investigated the possibility to decompose the false signals. First we classified false signals into two types; (I) brighter or (II) weaker than the true signal. For the former case, only a bright single source appears at the mean Faraday depth of true sources. On the other hand, for the latter case, an additional signal is shown as well as true signals. We developed a robust method to deconvolve signals. In this method, we took into account the phase term of FDF during the deconvolution. Therefore we called it as Phase RM CLEAN. This method can not only eliminate the latter type false signals but also suggest the existence of multiple sources for the former type. We found that a robust deconvolution method such as Phase RM CLEAN is necessary for obtaining reliable results by Faraday tomography. Additionally, we examined the performance of Phase RM CLEAN. It allows us to estimate the intrinsic polarization angles for each signal on the LoS. If the signals on the LoS are separated farther than the resolution for Faraday tomography, Phase RM CLEAN can estimate intrinsic polarization angles with error less than a few degrees. This error on the angle estimate corresponds to the error level expected from uncertainty by Faraday tomography.

Next, we adopted the Faraday tomography (with Phase RM CLEAN) to probe magnetic fields in the intergalactic medium (IGMF). As we mentioned above, Faraday tomography allows us to obtain the RMs of each contribution. Since Faraday tomography distinguishes each contribution by intensity of signals, we utilize weak emission from the intergalactic medium. In the FDF, contributions from RMs caused by IGMFs ($\mathrm{RM_{IGMF}}$) can be seen as a shift of the signal because IGMFs do not appear as a signal but contributes to RM. We proposed two strategies for the IGMF measurement. Strategy A aims a compact extragalactic source behind bright galaxies, e.g., our Galaxy. Normally, avoidance and removal of foreground emission are serious issues for cosmic magnetism observations. However, we observe an extragalactic source with bright foreground, then identify the contribution from non-emitting regions, in which IGMFs are dominated. Strategy B aims pair sources which are located very close each other on the sky. If they are close enough on the sky and located at the different depths, the difference of FDFs between two LoSs corresponds to the contribution of IGMFs between sources.

For strategy A, we assumed two sources, i.e., a diffuse source and a compact one, on the LoS. Diffuse and compact sources are regarded as a foreground and background sources, respectively. For simplicity, we assumed a Gaussian function as both FDF models. This simple model enables us to examine the performance of Faraday tomography. First, we adopted Faraday tomography to pseudo observation data assuming ongoing telescopes, ASKAP, Giant Metrewave Radio Telescope (GMRT) and LOFAR. By ongoing telescopes, it is impossible to detect the $\mathrm{RM_{IGMF}}$, even if measurement noise is negligible. The reason why they could not detect depends on the specification of telescopes. ASKAP and GMRT, which cover wavelength shorter than 1 m, do not cover enough bandwidth to resolve two sources. Therefore, the contribution of IGMF is buried under the spread signals due to

a beam. On the other hand, LOFAR achieves an adequate resolution because it covers the wavelength longer than 1 m, at which the resolution dramatically improves. However, reduction of the polarized signal from diffuse sources, which is called depolarization, is dominated at a longer wavelength. Thus, the invisibility of diffuse sources makes detections by LOFAR impossible. In order to recover these weaknesses, we next investigated cases with combinations of ongoing observatories. As we expected, poor resolution and invisibility were recovered. However, sparse frequency sampling due to the combination makes deconvolution difficult. In particular, the diffuse source is poorly reconstructed. This fact causes poor estimations of IGMFs. Furthermore we demonstrated with SKA which covers continuous wide wavelength. We found that SKA can detect IGMFs if $\mathrm{RM_{IGMF}}$ reaches 3–6 rad $\mathrm{m^{-2}}$. According to prior theoretical predictions, $\mathrm{RM_{IGMF}}$ can reach several rad $\mathrm{m^{-2}}$. Therefore, our result indicates that the IGMF can be detected using our scheme alone.

For strategy B, we imposed relatively a violent case, that is, a diffuse source and a compact one are overlapped. This may be a common situation in real observations. In this case, the accurate reconstruction of diffuse sources is needed for complete subtraction of the contribution from the diffuse source. As we have seen in discussion of strategy A, however, the reconstruction quality of the diffuse source by the current deconvolution method is not enough even for SKA. On the other hand, reconstruction of the compact sources can work very well even for such a violent case. Through the investigation of strategy B, we realized that the improvement of the deconvolution method can dramatically increases detectability of IGMFs.

Finally, we estimated the detectable limit of ongoing telescopes. Even if Faraday tomography cannot reconstruct the FDF very well, it provides us clues for the model construction, e.g., how many sources are on the LoS or how large RMs are expected between or inside sources. Based on these hints, we can construct the corresponding model with parameters, such as $\mathrm{RM_{IGMF}}$. Parameters are estimated by fitting with the observed data. Here, we investigated the expected errors on the model fitting by Fisher analysis for ongoing telescopes. We found that the detection level for combinations of ASKAP, GMRT and LOFAR can reach 3 rad $\mathrm{m^{-2}}$ just for 1 hour observation.

The Faraday tomography is highly expected to be one of the most powerful methods for exploring the cosmic magnetism by the upcoming SKA era. Further development of this method makes it possible to not only discover the IGMFs, but also reveal the three dimensional structure of magnetic fields in our Universe.

Appendix A

Other algorithms for FDF reconstruction

A.1 Compressive Sampling

The compressive sampling/sensing (CS) was proposed by E. J. Candès and M. B. Wakin in 2008 [90], which is a signal processing technique for reconstructing a signal or finding solution under some assumptions. This technique is well applied to photography, the Magnetic Resonance Imaging (MRI) or compression/decompression of images. F. Li et al (2011) [91, 92] have applied the CS to radio astronomy, i.e. not only the image reconstruction from observation by interferometers, but also Faraday tomography. The CS reconstructs signals under two fundamental premises, i.e. **sparsity** and **incoherence**. Before we review the CS, the Fourier relationship between the polarized intensity and FDF should be rewritten by matrix format,

$$\tilde{P}(\lambda^2) = \int_{-\infty}^{\infty} F(\phi) e^{2i\phi\lambda^2} d\phi \;\longrightarrow\; \tilde{\mathbf{P}} = \mathbf{YF} \;, \tag{A.1}$$

where $\mathbf{P} = [P(\lambda_1^2), P(\lambda_2^2), \ldots, P(\lambda_M^2)]^T$ and $\mathbf{F} = [F(\phi_1), F(\phi_2), \ldots, F(\phi_N)]^T$ are the observed polarized intensity and the FDF. $\mathbf{Y}^{(mn)} = e^{2i\phi_n\lambda_m^2}$ represents Fourier transform matrix which is $M \times N$ matrix.

A.1.1 Sparsity

A FDF would be sparse when it is constructed by only a few elements having non-zero value with respect to a basis function, such as Fourier transform function or Wavelet transform function. FDF is sparse and satisfies a premise that the CS can work, when $\mathbf{F}$ can be rewritten by

$$\mathbf{F} = \Theta f, \tag{A.2}$$

where Θ is a certain basis function represented by $N \times N$ matrix. f is called the sparse representation of FDF. For the case with a few Faraday thin sources, it can be easily understood that FDF is sparse and Θ can be a identity matrix.

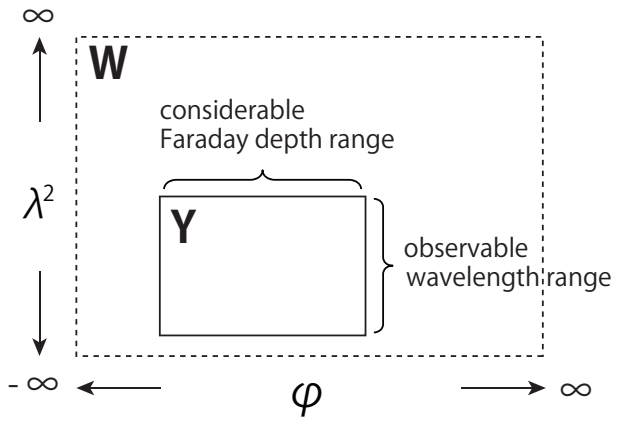

Figure A.1: The relation between **W** and **Y**.

A.1.2 Incoherence

Here coherence means the orthogonality between **W** and Θ, where **W** is the sensing system. Please note that **Y** is a part of **W**. In the process of the CS, **W** and Θ are used for sensing and representing the signal **F**, respectively. The incoherence between **W** and Θ does not restrict the formulation of Θ, but it does merely make its treatment easier. The coherence is defined by

$$\mu(\mathbf{W}, \Theta) = \sqrt{N} \max_{1 \leq k,j \leq N} |\langle \mathbf{W}_k, \Theta_j \rangle| \ , \tag{A.3}$$

where $|\langle \mathbf{W}_k, \Theta_j \rangle|$ is the inner product between kth row of **W** and jth column of Θ. The coherence calculates the largest correlation between any two rows of **W** and Θ. If Θ contains correlated elements with **W**, coherence would be large, otherwise small. This coherence is related to the smallest number of observed data points M that the CS can correctly reconstruct the signal. For given observation $\tilde{\mathbf{P}}$ selected randomly from **W** domain, signals can be exactly reconstructed with high probability when the number of data points M satisfies

$$M \geq C\, \mu(\mathbf{W}, \Theta)^2\, S\, \log N \ , \tag{A.4}$$

where C is a certain positive constant and S is the number of non-zero elements in f. Therefore, fewer data points are enough when the coherence is small.

A.1.3 Solution ambiguity and incompleteness of sparsity

We briefly mentioned the concept of the CS under ideal situation. For the application of the CS to real observations, however, mainly two issues can be considered.

First is the *incompleteness* of sparsity. It means that normally most of the elements have just approximately zero values in real cases due to measurement noise or complex structure of FDF. Thus, Equation (A.1) can be rewritten by adding noise vector **n**, then

combined with Equation (A.2),

$$\tilde{\mathbf{P}} = \Phi f + \mathbf{n} \quad \text{for} \quad \Phi \equiv \mathbf{Y}\Theta \ . \tag{A.5}$$

The CS is applicable for such case as well, but a new conception should be introduced, that is the restricted isometry property (RIP). In Equation (A.5), Φ is a new sensing matrix and f is approximately sparse representation. If there exists a constant ζ_s, which is called the isometry constant and satisfies

$$(1-\zeta_s)\,\|f\|_{\ell_2}^2 \ \le \ \|\Phi f\|_{\ell_2}^2 \ \le \ (1+\zeta_s)\,\|f\|_{\ell_2}^2 \tag{A.6}$$

for any f, f would be said to be s–sparse, where

$$\|A\|_{\ell_n} \equiv \sum_{i=1}^{N} |A|^n \tag{A.7}$$

for a vector $A = [A_1, A_2, \ldots, A_N]$. s is the smallest number satisfying Equation (A.6) and corresponds to the number of large elements in f. Furthermore, when sub-matrix Φ_s satisfies Equation (A.6) replaced Φ with Φ_s, it can be said that Φ satisfies sth order RIP.

If Φ satisfies $2s$th order RIP and $\zeta_{2s} < \sqrt{2}-1$ is assumed, the solution $\tilde{f}$ would obey

$$\|\tilde{f} - f\|_{\ell_2} \le C_0 \frac{\|f - f_s\|_{\ell_1}}{\sqrt{s}} + C_1 \|n\|_{\ell_2}^2 \ , \tag{A.8}$$

where f_s corresponds to the vector f but the largest s elements is set to zero, and

$$C_0 = \frac{2(1+\beta)}{1-\beta}, \quad C_1 = \frac{2\alpha}{1-\beta} \quad \text{for} \quad \alpha \equiv \frac{2\sqrt{1+\zeta_{2s}}}{1-\zeta_{2s}}, \quad \beta \equiv \frac{\sqrt{2}\zeta_{2s}}{1-\zeta_{2s}} \ . \tag{A.9}$$

If f is completely s–sparse and noiseless, the solution is exactly same with f. The proof is shown by E. J. Candès[1].

Second issue is the limitation of observable channels. If $M \ll N$, abundant candidates of FDF can be consistent with observed data. In order to resolve this ambiguity, prior information should be utilized, for instance, the FDF is sparse in the Faraday depth space or has sparse representation with respect to a basis function. Under this assumption, the CS recommends FDF minimizing L1 norm since minimum L1 norm optimizes the sparsity [93]. Therefore, the estimated FDF can be defined by

$$\min \|\tilde{f}\|_{\ell_1} \quad \text{subject to} \quad \|\Phi f - \tilde{\mathbf{P}}\|_{\ell_2} \le \|n\|_{\ell_2} \ . \tag{A.10}$$

Finally, we emphasize that the CS is not a symmetric process. For normal compression process, there is a decompression process and it is just inverse of the compression. However, decompression process for the CS has many paths due to choices of Θ. It means that the solution depends on choice of basis function. Also, a new sensing matrix Φ constructed by basis function should satisfy the RIP. Therefore it should be noted that the understanding of both of the structure of FDF and basis functions is required.

[1] www.statweb.stanford.edu/c̃andes/papers/RIP.pdf

A.1.4 CS-based Faraday Tomography

F. Li et al. (2011) have numerically examined the performance of CS-based Faraday tomography by comparing with RM CLEAN [91]. They designed three kinds of algorithms, CS–RM–Thin, CS–RM–Thick and CS–RM–Mix. Before going for the detail of examination, we briefly introduce these algorithms.

CS–RM–Thin

This algorithm is designed under assumption that FDF is Faraday thin. It means that the basis function matrix Θ can be written by an identity matrix. Since the FDF is a complex function, the reconstructed FDF, $\tilde{\mathbf{F}}$, minimizing L1 norm, can be rewritten as

$$\min \left\{ \left\| \mathrm{Re}\left(\tilde{\mathbf{F}}\right) \right\|_{\ell_1} + \left\| \mathrm{Im}\left(\tilde{\mathbf{F}}\right) \right\|_{\ell_1} \right\} \quad s.t. \quad \|\mathbf{Y}\tilde{\mathbf{F}} - \tilde{\mathbf{P}}\|_{\ell_2} \leq \|n\|_{\ell_2} \ . \tag{A.11}$$

The idea for this algorithm is similar to RM CLEAN because RM CLEAN does also assume that the FDF is constructed only by signals described by delta functions.

CS–RM–Thick

Next algorithm is based on assumption that FDF is Faraday thick. The authors adopted the Daubechies 8 wavelet transform function D_8 as the basis function [94]. If the sparse representation can be written by wavelet coefficient of FDF $f = D_8\mathbf{F}$, the new sensing matrix would be $\Phi = \mathbf{Y}D_8^{-1}$ using inverse of D_8. Therefore, the measurement equation and the solution $\tilde{\mathbf{F}}$ can be estimated by

$$\mathbf{Y}D_8^{-1}f = \tilde{\mathbf{P}} \ , \tag{A.12}$$

$$\min \left\{ \left\| D_8\,\mathrm{Re}\left(\tilde{\mathbf{F}}\right) \right\|_{\ell_1} + \left\| D_8\,\mathrm{Im}\left(\tilde{\mathbf{F}}\right) \right\|_{\ell_1} \right\} \ s.t. \ \|\mathbf{Y}\tilde{\mathbf{F}} - \tilde{\mathbf{P}}\|_{\ell_2} \leq \|n\|_{\ell_2} \ . \tag{A.13}$$

Of course, other wavelet function can be adopted and the choice depends on the shape of FDF. The authors selected this function, because sinc–like function is assumed in their work.

CS–RM–Mix

These two algorithms introduced above are proposed for reconstructing only the Faraday thin or thick source. However, it can be considered that we have no prior information in terms of FDF. For the most of real cases, it could happen that there exist both Faraday thin and thick sources on the LoS. For such cases, if we adopt both algorithm independently, neither of them would provide reasonable results, obviously. Therefore authors proposed a hybrid algorithm. First they divide FDF into two subsets, $\mathbf{F} = \mathbf{F}_{\mathrm{thin}} + \mathbf{F}_{\mathrm{thick}}$.

	RM CLEAN	CS-RM-Thin	CS-RM-Thick	CS-RM-Mix
Thin sources	0.78	0.00	0.84	0.76
Thick sources	0.91	1.07	0.72	0.77
Mix sources	1.03	0.95	0.81	0.80

Table A.1: The RMSEs for comparison between algorithms (inspired by Table 1 of [92]).

As seen above, $\mathbf{F}_{\rm thin}$ and $\mathbf{F}_{\rm thick}$ have sparse representation in the Faraday depth domain and D8 wavelet domain, respectively. Then measurement equation can be rewritten as

$$\mathbf{Y}\mathbf{F}_{\rm thin} + \mathbf{Y}\mathbf{F}_{\rm thick} = \mathbf{Y}\mathbf{F}_{\rm thin} + \mathbf{Y}D_8^{-1} f_{\rm thick} = \tilde{\mathbf{P}} \ . \tag{A.14}$$

Furthermore, using the identity matrix $\mathbf{I}$ and the zero matrix $\mathbf{O}$ that all elements has zero value, the Equation (A.14) can be written by

$$[\mathbf{Y}\ \mathbf{Y}] \begin{bmatrix} \mathbf{I} & \mathbf{O} \\ \mathbf{O} & D_8^{-1} \end{bmatrix} \begin{bmatrix} \mathbf{F}_{\rm thin} \\ f_{\rm thick} \end{bmatrix} = \tilde{\mathbf{P}} \ . \tag{A.15}$$

Then, the solution can be estimated by

$$\min \left\{ \|\mathrm{Re}\ (\tilde{\mathbf{c}})\|_{\ell_1} + \|\mathrm{Im}\ (\tilde{\mathbf{c}})\|_{\ell_1} \right\} \qquad s.t.\ \|\mathbf{Y}_{\rm mix}\mathbf{T}\tilde{\mathbf{c}} - \tilde{\mathbf{P}}\|_{\ell_2} \leq \|n\|_{\ell_2} \ , \tag{A.16}$$

where

$$\mathbf{Y}_{\rm mix} \equiv [\mathbf{Y}\ \mathbf{Y}], \quad \mathbf{T} \equiv \begin{bmatrix} \mathbf{I} & \mathbf{O} \\ \mathbf{O} & D_8^{-1} \end{bmatrix}, \quad \mathbf{c} \equiv \begin{bmatrix} \mathbf{F}_{\rm thin} \\ f_{\rm thick} \end{bmatrix} \ . \tag{A.17}$$

A.1.5 Performance of the CS-based Faraday tomography

The authors assumed 126 observing channels between 0.036 to 0.5m, which is distributed evenly in λ^2 domain. The FWHM of RMSF is almost 14 rad m^{-2}. In order to search solution which minimized L1 norm, they have developed a algorithm[2] based on iterative shrinkage thresholding algorithm (ISTA) [95] which is implemented in MATLAB.

They prepared three cases, (a) Faraday thin sources, (b) Faraday thick sources and (c) mixed sources. The results for all cases is displayed in Figure A.2 from left to right, respectively. For comparison, they used the root mean square error (RMSE) defined by

$$\mathrm{RMSE} = \sqrt{\frac{\sum_i (\mathbf{F}_{\rm input}^{(i)} - \tilde{\mathbf{F}}^{(i)})^2}{N}} \ , \tag{A.18}$$

which is summarized in Table A.1.

[2]http://code.google.com/p/csra/downloads

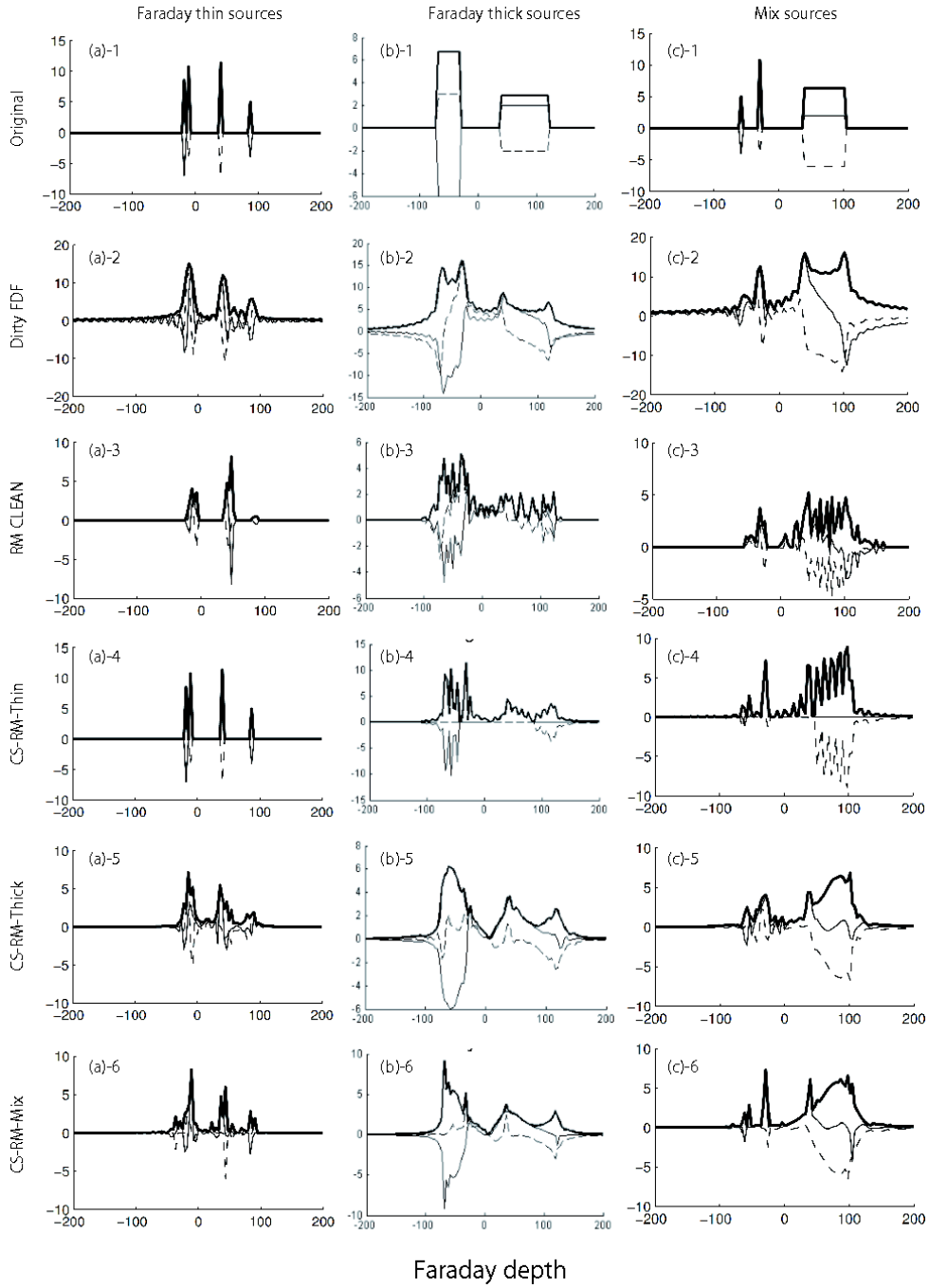

Figure A.2: The comparison between results of RM CLEAN and that of CS-based Faraday tomography. From left to right, the case with Faraday thin, thick and mix sources are described and from top to bottom, the original FDF, dirty FDF, the result of RM CLEAN, that of CS-RM-Thin, Thick and Mix are shown, respectively. The thick solid lines describe the absolute value of FDF, thin solid and dashed lines show the real and imaginary part of FDF, respectively.

Faraday thin sources The left panels in Figure A.2 represent the results with Faraday thin sources. The authors simulated four Faraday thin sources. Two of them are separated just 7.0 rad m^{-2} which is a half of FWHM of RMSF (see (a)-1). Therefore, these two sources could not be separated by Faraday tomography and RM CLEAN (see (a)-2 and (a)-3). The results using CS can be seen at (a)-4, 5 and 6. It should be emphasized that the CS-RM-Thin completely reconstructs the FDF (see (a)-4) even the sources which mutually separate smaller separation than the FWHM of RMSF. The CS-RM-Thick provides the worst result, which is worse than RM CLEAN, because there are no Faraday thick source which can have sparse representation in wavelet domain. CS-RM-Mix algorithm relatively reconstruct better results than CS-RM-Thick algorithm, but it cannot be said good enough.

Faraday thick sources The results with Faraday thick sources are shown at the center panels in Figure A.2. Here two Faraday thick sources are simulated. Both of two has wider thickness than the FWHM of RMSF, 80.0 and 40.0 rad m^{-2}. The separation is also wider than the FWHM of RMSF (see (b)-1). In this case, both RM CLEAN and CS-RM-Thin algorithm do not work well, because the FDF is not sparse in Faraday depth space any more (see (b)-3 and 4). As expected, CS-RM-Thick behaves better performance, although it is not perfect unlike CS-RM-Thin for Faraday thin case. Also the CS-RM-Mix provides similar RMSE. However, especially regarding the estimation of amplitude and phase, CS-RM-Thick algorithm provides better results. If the other basis function is applied, the results of CS-RM-Thick might be improved.

Mix sources We finally show the case of mixed situation which includes two Faraday thin sources and a thick source which separate larger than FWHM of RMSF each others (see (c)-1). Although the dirty FDF indicates two thin sources and a thick sources, RM CLEAN badly performed. The CS-RM-Thin algorithm can reconstruct Faraday thin sources well, but reconstructed Faraday thick source is constructed by many spiky signals like the result of RM CLEAN and it causes huge RMSE (see (c)-4). On the contrary, CS-RM-Thick nicely reconstructs the Faraday thick source, but Faraday thin sources extend comparatively (see (c)-5). The result of CS-RM-Mix takes merits of both CS-RM-Thin and CS-RM-Thick, thus the reconstruction of the Faraday thick source resembles that of CS-RM-Thick and Faraday thick sources are well separated like the result of CS-RM-Thin (see (c)-6). From the aspect of RMSE, CS-RM-Mix algorithm minimizes RMSE.

As we saw above, the algorithm which does greatly perform for any circumstances does not exist. Also the results by CS-based Faraday tomography remarkably depend on the choice of algorithms or basis functions. It means that the prior information would be a key for success of reliable reconstructions. If there is no prior information, CS-RM-Mix should be applied because it relatively provides moderate results for any cases. Apart from that, either CS-RM-Thin with large Faraday depth step or CS-RM-Thick with small Faraday depth step can be selected. Because, for large Faraday depth step, FDF can be deemed to be thin sources and vice versa.

A.2 Wavelet based Faraday Tomography

The wavelet-based Faraday tomography was suggested by P. Frick et al. (2010) [96]. The original motivation of this work is to solve the problem that we are able to use data for only positive λ^2. They first revealed that Faraday tomography can not reconstruct the phase of Faraday thick sources even if all wavelength range is observed. The estimation of phases is quite important for determination of the orientation of the regular magnetic fields of galaxies. They started to consider the properties of the physical phenomenon in galaxies, then they assume that the FDF can be symmetric with respect to the Faraday depth of FDF ϕ_0 that FDF has maximum amplitude. Then, the polarized intensity for negative λ^2 can be written as

$$P(-\lambda^2) = e^{-4i\phi_0\lambda^2} P(\lambda^2) \ . \tag{A.19}$$

Using the predicted polarized intensity for negative λ^2 as well, the result of Faraday tomography is dramatically improved, especially the estimation of phases. However, the behavior of $P(-\lambda^2)$ depends on the Faraday depth of galaxies. That means Faraday depth should be estimated first, or FDF can be reconstructed by changing Faraday depth. It leads the idea using wavelet.

The authors defined the wavelet transform of FDF as,

$$w_F(a,b) = \frac{1}{|a|} \int_{-\infty}^{\infty} F(\phi) \psi^* \left(\frac{\phi - b}{a} \right) d\phi \ , \tag{A.20}$$

where a denotes the scale of wavelet window, b defines the position of wavelet window which corresponds to ϕ_0 and $\psi(\phi)$ represents the wavelet, here it is defined as

$$\psi(\phi) = (1 - \phi^2) \exp\left(-\frac{\phi}{2} \right) \ . \tag{A.21}$$

The FDF can be written by the inverse transform,

$$F(\phi) = \frac{1}{C_\psi} \int_{-\infty}^{\infty} \int_{-\infty}^{\infty} \psi \left(\frac{\phi - b}{a} \right) w_F(a,b) \frac{da\, db}{a^2} \ , \tag{A.22}$$

$$C_\psi = \frac{1}{2} \int_{-\infty}^{\infty} \frac{|\hat{\psi}(k)|^2}{|k|} dk \ , \tag{A.23}$$

if C_ψ does not diverge. Here,

$$\hat{\psi}(k) = \int_{-\infty}^{\infty} \psi(\phi) e^{-ik\phi} d\phi \ . \tag{A.24}$$

is the Fourier transform of $\psi(\phi)$.

By Equation (A.20), the wavelet expression of FDF with the polarized intensity can be directly defined as

$$w_F(a,b) = \frac{1}{2\pi|a|}\int_{-\infty}^{\infty}\int_{-\infty}^{\infty} P(\lambda^2)e^{-2i\phi\lambda^2}d\lambda^2\psi^*\left(\frac{\phi-b}{a}\right)d\phi \tag{A.25}$$

$$= \frac{1}{2\pi}\int_{-\infty}^{\infty} P(\lambda^2)e^{-2ib\lambda^2}\hat{\psi}^*(-2a\lambda^2)d\lambda^2 \ . \tag{A.26}$$

The authors suggested that the wavelet coefficient can be divided into two parts $w_f(a,b) = w_+(a,b) + w_-(a,b)$, which describe positive λ^2 or negative λ^2,

$$w_+(a,b) = \int_{0}^{\infty} P(\lambda^2)e^{-2ib\lambda^2}\hat{\psi}^*(-2a\lambda^2)d\lambda^2 \ , \tag{A.27}$$

$$w_-(a,b) = \int_{-\infty}^{0} P(\lambda^2)e^{-2ib\lambda^2}\hat{\psi}^*(-2a\lambda^2)d\lambda^2 \ , \tag{A.28}$$

$$= w_+(a, 2\phi_0(a,b) - b) \ , \tag{A.29}$$

by cooperating Equation (A.19) and (A.28) for (A.29). $\phi_0(a,b)$ has a value of b that $w_+(a,b)$ has a peak around (a,b).

A.2.1 RM CLEAN for Wavelet-based Faraday tomography

By interpolation of the polarized intensities at negative λ^2, the window function should be reformed. Then RMSF should be rewritten as well. Equation (A.19) brings the RMSF for this reformation $R_w(\phi)$,

$$R_w(\phi) = 2K\frac{\sin(2\phi\,\Delta\lambda^2)}{\phi}\cos(2\phi\lambda_0^2), \tag{A.30}$$

then convolution representation of reconstructed FDF can be written by

$$\tilde{F}(\phi) = e^{-4i\phi_0\lambda_0^2}F(\phi) * R_w(\phi) \ . \tag{A.31}$$

If one use $R_w(\phi)$ instead of $R(\phi)$, the RM CLEAN for this reformation would be easily implemented.

A.2.2 Performance of the Wavelet-based Faraday tomography

As we saw above, this algorithm is highly motivated for more robust estimation of phase of Faraday thick sources. Furthermore, it is developed based on the idea that FDF is symmetric in terms of Faraday depth of source, ϕ_0. Thus both Faraday thin and thick sources can be adopted. In particular, it should be highlighted that this has the advantage not only for the phase estimation, but also the Faraday thickness estimation using parameter

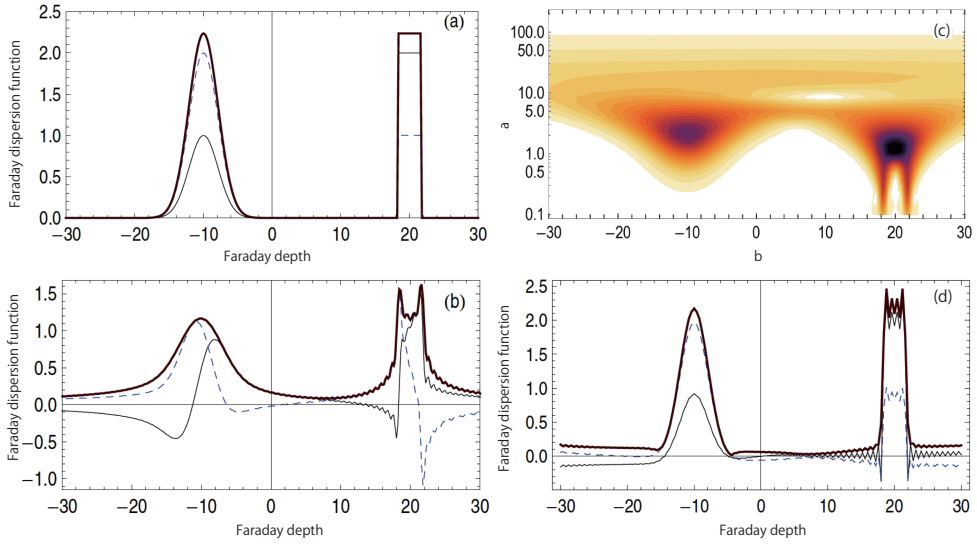

Figure A.3: The comparison between test with standard Faraday tomography and wavelet based Faraday tomography. (a) The model of FDF for this examination. (b)The result by standard Faraday tomography. (c)The wavelet coefficients $|w(a,b)|$ on the (a,b) plane. (d) The reconstructed FDF by Wavelet based Faraday tomography. For (a), (b) and (d), the thick solid line represents the amplitude, thin solid and dashed line show the real and imaginary part, respectively.

a. For investigating the performance of this algorithm, the authors prepared two Faraday thick sources, which includes Gaussian and top hat function. First, they reconstructed using entire positive λ^2 domain. The result is displayed in Figure A.3. Looking at the (b) in Figure A.3, the standard Faraday tomography successfully reconstructs the FDF but some extends are appeared. However, it cannot reproduce the phase even if entire wavelength is available. The reconstructed FDF by wavelet based Faraday tomography and estimated polarized intensity at negative λ^2 can be seen at (d). The phase is estimated quite well. Furthermore, the extends around FDF are also suppressed.

They demonstrated not only such ideal cases, but also the cases with limited wavelength, $0.6 < \lambda^2 < 0.78$ and $0.6 < \lambda^2 < 2.5$. The results can be seen in Figure A.4. It should be noticed that the wavelet coefficients do not have any value at $a > 2$. This is caused by minimum wavelength and shows the limit of thickness estimation like maximum Faraday thickness that we introduced at Section 3.4. Both wavelength ranges, neither algorithms can reconstruct FDF correctly, because lack of information is significant. The wavelet based Faraday tomography generates oscillations, especially the case of $0.6 < \lambda^2 < 0.78$. The shape of RMSF seems to cause this oscillations. However, it should be highlighted that the phase around peaks are correctly estimated by the Wavelet based Faraday tomography even if only limited wavelength is available. The effect of observation at long wavelength range can be seen in reconstruction of small scale structures. For $0.6 < \lambda^2 < 2.5$, the horn–like structures are appeared at top hat sources. This property

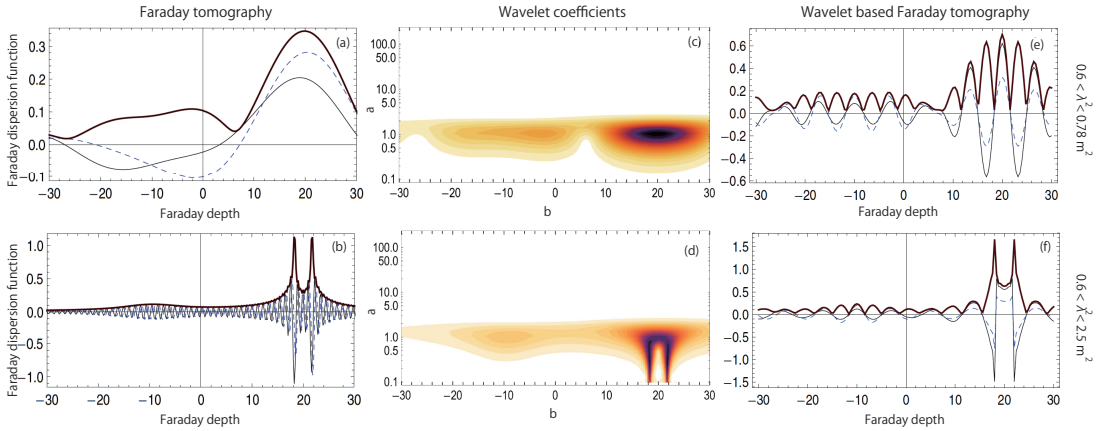

Figure A.4: The results of reconstruction with limited wavelength range, $0.6 < \lambda^2 < 0.78$ (top panels) and $0.6 < \lambda^2 < 2.5$ (bottom panels).

could not depend on reconstruction algorithm because it just reflects the property of the polarization intensity.

A.3 Multiple Signal Classification

M. Andrecut proposed a new deconvolution method. It is an application of the MUltiple SIgnal Classification algorithm (MUSIC) [97], which is based on the eigen-deconvolution proposed by M. Cheney 2001 [98]. This algorithm is mostly applied for identifying frequencies or incoming direction of observed signals, or extracting desired wave from diffraction or interference wave.

In their approach, a model $F(\phi)$ is assumed that it contains K Faraday thin sources which is adequately smaller than the number of frequency channel N, i.e.

$$F(\phi) = \sum_{k=1}^{K} F_k \delta(\phi - \phi_k) \ . \tag{A.32}$$

Then the sampled polarized intensity at wavelength channels λ_n^2 can be written as,

$$P_n = \sum_{k=1}^{K} F_k e^{2i\phi_k(\lambda_n^2 - \lambda_0^2)} + n_n \ , \tag{A.33}$$

here we assume the rectangle window function and n_n indicates the complex measurement noise at sampled channel. The covariance matrix of observed polarized intensity $\mathbf{R}$ can be estimated after divided into $M = N - L$ segments, L is the number of elements and selectable parameter. $L = 2N/3$ shows a good results by their experiments [97]. Then,

covariance matrix can be written as

$$\mathbf{R} = \frac{1}{M}\sum_{m=1}^{M} \mathbf{P}^{(m)}(\mathbf{P}^{(m)})^H \ , \tag{A.34}$$

where $\mathbf{P}^{(m)} = [P_m, P_{m+1}, \ldots, P_{m+L}]$ and H represents the conjugate transpose operation. Using sorted eigenvalues, $\mu_1 \geq \mu_2 \geq \ldots \geq \mu_L$, and eigenvectors of $\mathbf{R}$, $\mathbf{v}^{(1)} \geq \mathbf{v}^{(2)} \geq \ldots \geq \mathbf{v}^{(L)}$, the covariance matrix can be rewritten as,

$$\mathbf{R}\mathbf{v}^{(\ell)} = \mu_\ell \mathbf{v}^{(\ell)} \quad \text{or} \quad \mathbf{R} = \sum_{\ell=1}^{L} \mu_\ell \mathbf{v}^{(\ell)}(\mathbf{v}^{(\ell)})^H \ . \tag{A.35}$$

Since FDF contains just K sources, the smaller $L-K$ eigenvalues should be small and below the noise level. Therefore, $\mathbf{R}$ can be separated two subsets,

$$\mathbf{R} = \sum_{\ell=1}^{K} \mu_\ell \mathbf{v}^{(\ell)}(\mathbf{v}^{(\ell)})^H + \sum_{\ell=K+1}^{L} \mu_\ell \mathbf{v}^{(\ell)}(\mathbf{v}^{(\ell)})^H \ , \tag{A.36}$$

first and second term are called signal subset and noise subset, respectively. Here, the projection operator to the noise subset $\mathbf{R}_{\mathbf{v}}^{(\mathrm{noise})}$ and signal subset sampling vector $f(\phi)$ can be defined by

$$\mathbf{R}_{\mathbf{v}}^{(\mathrm{noise})} = \sum_{\ell=K+1}^{L} \mathbf{v}^{(\ell)}(\mathbf{v}^{(\ell)})^H \ , \tag{A.37}$$

$$f(\phi) = \left[e^{2i\phi\lambda_1^2}, e^{2i\phi\lambda_2^2}, \ldots, e^{2i\phi\lambda_L^2}\right]^T \ , \tag{A.38}$$

respectively. If the $f(\phi)$ represents the signal, its projection would be close to zero since signal and noise do not have correlation. On the contrary, if the $f(\phi)$ is not the signal, projection would have relatively large value. Hence, the MUSIC pseudo-spectrum defined by

$$S(\phi) = \frac{1}{\left|\mathbf{R}_{\mathbf{v}}^{(\mathrm{noise})} f(\phi)\right|^2} \tag{A.39}$$

has large value at ϕ_k $(k = 1, 2, \ldots, K)$. After determination of Faraday depth, amplitude of sources F_k can be easily estimated by least–square fitting approach. This is the basic strategy of the MUSIC algorithm.

A.3.1 Performance of the MUSIC

Next we review the numerical experiment and comparison with traditional Faraday tomography reported by M. Andrecut (2013) [97]. The author examined four cases with

observed frequency	1100–1400 MHz
$\delta\nu$	2 MHz
$\lambda^2_{\rm min}$	4.6×10^{-2} m^2
$\lambda^2_{\rm max}$	7.4×10^{-2} m^2
FWHM of RMSF	122 rad m^{-2}

Table A.2: Setting for numerical experiment of MUSIC.

two Faraday thin sources. For comparison the author also prepared dirty FDF and Faraday components resulted by RM CLEAN. We summarized conditions of the numerical experiment in Table A.2 and displayed the comparisons in Figure A.5.

First, the author considered the case that separation between sources is 1.0 FWHM ($\phi_1 = 0.0$ rad m^{-2}, $\phi_2 = 122.0$ rad m^{-2}; Case I). The comparison is on the left top panel. Since separation would be the limit for RM CLEAN, the Faraday depth estimated by RM CLEAN is not very good, $\tilde{\phi}_i = 2.01$ rad m^{-2}, $\tilde{\phi}_2 = 142.95$ rad m^{-2}. On the other hand, the MUSIC can recover the almost exactly Faraday depth, $\tilde{\phi}_i = 1.05$ rad m^{-2}, $\tilde{\phi}_2 = 122.81$ rad m^{-2}.

Next, separation smaller than FWHM is considered, such as 0.5 FWHM (Case Ⅱ, see the right top panel) and 0.25 FWHM (Case Ⅲ, see the left bottom panel). Surprisingly, the MUSIC can estimate Faraday depth correctly even the source separation is a half of the theoretical resolution of Faraday tomography. This super-resolution is the most significantly improved point by the MUSIC. In the case with separation of 0.25 FWHM, the MUSIC algorithm can not resolve two sources anymore. However, the MUSIC pseudo-spectrum has a peak at averaged Faraday depth of two model sources, while RM CLEAN provides a peak at outside of range. Moreover, when low SNR case is assumed (Case Ⅳ, see the right bottom panel), the condition is same with Case Ⅲ. In this case, the MUSIC algorithm provides very similar performance with RM CLEAN.

Finally, the computational cost should be referred. It depends on covariance matrix size L and would be relatively larger than RM CLEAN, but the case with the order of hundreds L is comparable with that of RM CLEAN.

A.4 Comparison of algorithms

The Polarisation Sky Survey of the Universe's Magnetism (POSSUM) group has organized the data challenge assuming observation by ASKAP, then compared the results obtaining by various algorithms for determination of rotation measure and Faraday structure [99]. Here we review this work. They prepared 17 data sets covering three types of models, e.g. a single Faraday thin source, two Faraday thin sources and single Faraday thick source. 3 of 17 data sets include both of single Faraday thin and thick source. The detail

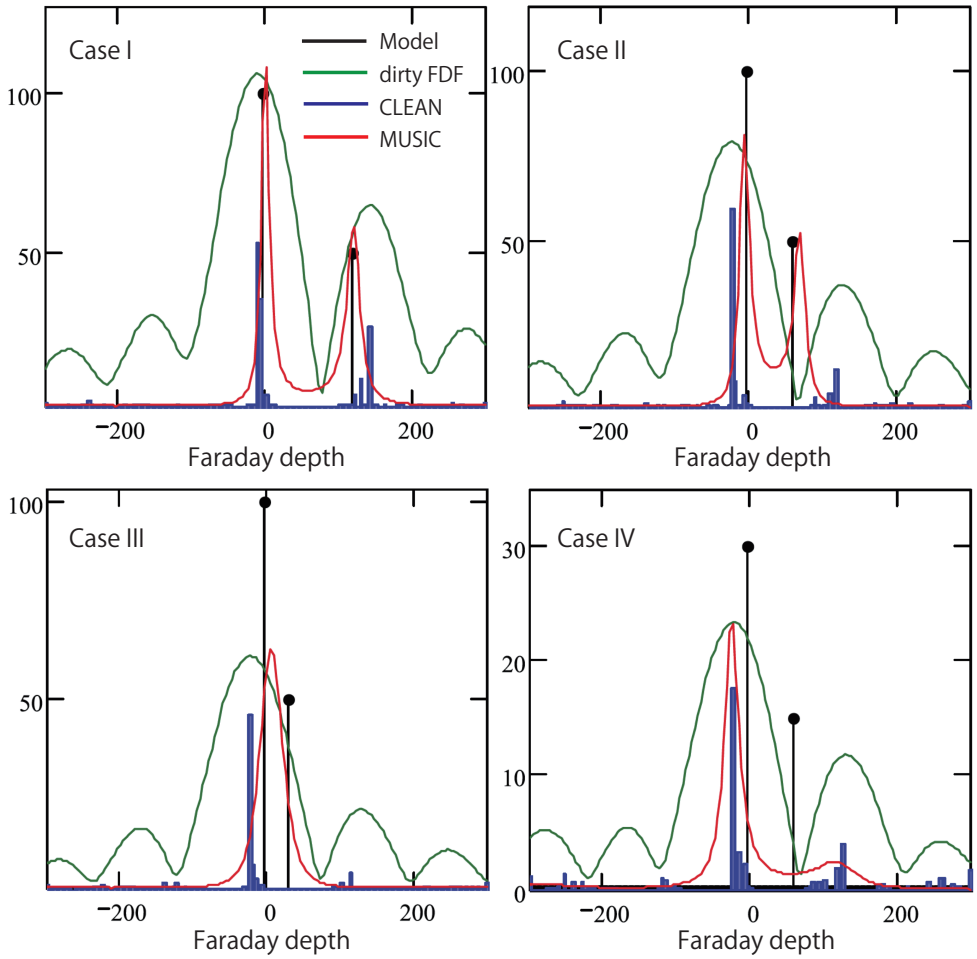

Figure A.5: The comparison between the MUSIC and traditional algorithms [97].

of FDF models are following.

Single Faraday thin source A model of FDF is simply a delta-function, $F(\phi) = F_0\delta(\phi - \phi_0)$, where ϕ_0 is the Faraday depth of the source which is selected randomly.

Two Faraday thin sources A FDF is just sum of two delta-functions, $F(\phi) = F_1\delta(\phi - \phi_1) + F_2\delta(\phi - \phi_2)$. The separation of two sources is taken both smaller and greater than the FWHM of RMSF. Also, the authors did not choose the situations which the RM ambiguities could happen.

Single Faraday thick source A FDF is a top-hat function, i.e. $F(\phi) = F_0$ for $\phi_c - \phi_w/2 < \phi < \phi_c + \phi_w/2$, otherwise $F(\phi) = 0$. Here ϕ_c is the central Faraday depth of the source and ϕ_w is the Faraday thickness of the source. The Faraday thickness is less than maximum scale, 25 rad m^{-2} and 50 rad m^{-2}.

observed frequency	1100–1300 MHz
$\delta\nu$	1 MHz
$\lambda^2_{\rm min}$	4.6×10^{-2} m^2
$\lambda^2_{\rm max}$	7.4×10^{-2} m^2
$\delta\lambda^2$	6.6×10^{-5} m^2
FWHM of RMSF	122 rad m^{-2}
Maximum depth	26319 rad m^{-2}
Maximum thickness	68 rad m^{-2}
SNR	32

Table A.3: Several key parameters for data challenge (X. H. Sun et al. 2014). [99]

Furthermore, several key parameters for data challenge can be seen in Table A.3.

A.4.1 Figure of merit

For this data challenge, 13 challengers (including us as FS–KK) participated. They cover four algorithms, such as Faraday Tomography with CLEAN (7 challengers), compressive sampling (2), Wavelet based tomography (1) and Model fitting (3).

Before comparisons, three figures of merit are defined. The first is difference between weighted average of estimated Faraday depth and that of input model, $|\mathrm{RM_{wtd}}(\mathrm{est.} - \mathrm{model})|$, where weighted average value is defined by

$$\mathrm{RM_{wtd}} = \frac{\sum_i |F_i| \phi_i}{\sum_i |F_i|} \ , \tag{A.40}$$

where i indicates the index of source. For the case of single thin source, $\mathrm{RM_{wtd}}$ should be just same with Faraday depth of source ϕ_0. Also the theoretical error should be confirmed. In this work, $\sigma_{\rm RM} = 0.5$ FWHM/SNR is applied. In current work, $\sigma_{\rm RM} \sim 1.9$ rad m^{-2}.

Second is the separation of two Faraday thin sources or the Faraday thickness of a Faraday thick source, $|\Delta\phi(\mathrm{est.} - \mathrm{input})|$. $\Delta\phi$ is defined by

$$\Delta\phi = |\phi_1 - \phi_2| \ . \tag{A.41}$$

For the case with single Faraday thin source, $\Delta\phi = 0$ is defined. If there are two Faraday thin sources, $\Delta\phi$ is defined as difference between these two sources. This value would indicate the environment of the intergalactic medium between sources, or inside of source since two Faraday thin sources assume just two independent radio galaxies within same beam or a galaxy with two lobes or one core and one jet. Therefore, the ability to measure

$\Delta\phi$ is important for exploring magnetic fields in the intergalactic medium (we mentioned in detail at Sec. 5). For the case of Faraday thick source, $\Delta\phi$ is defined as ϕ_w, which can indicate the structure of magnetic fields inside of galaxies. Furthermore, $\Delta\phi$ can avoid the complexity of FDF like RM ambiguity. The theoretical error is estimated as $\sigma_{\Delta\phi} = \sqrt{2}\sigma_{\rm RM} \sim 2.7$ rad m^{-2} under assumption that sources do not affect each other in Faraday depth domain.

The last is the reduced chi square χ^2_r defined as

$$\chi^2_r = \frac{1}{2N - 3N_s} \sum_{i=1}^{N} \frac{(\tilde{Q}_i - Q_i)^2 + (\tilde{U}_i - U_i)^2}{\sigma_i^2} \ , \tag{A.42}$$

where $N = 300$ is the number of data points, N_s is the number of sources, $\tilde{Q}$ and $\tilde{U}$ are model Stokes parameters and σ_i is the rms noise for each data point. This figure of merit mainly represents whether intensities and intrinsic polarization angle are estimated properly. In particular, the intrinsic polarization angle is important for investigating the orthogonal components of magnetic fields in the sources.

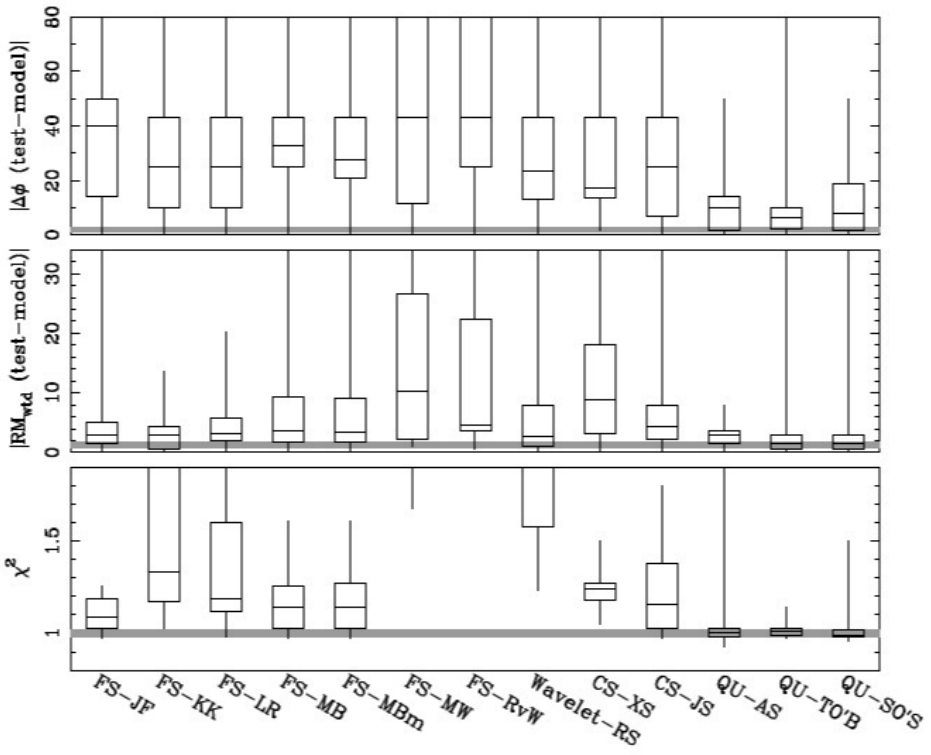

Figure A.6: Three figures of merit overall 17 data sets for each challengers. (Fig. 3 of X. H. Sun et al. 2014) [99]

A.4.2 Overall results

Figure A.6 describes all figures of merit over all 17 data sets. 13 challengers are on x-axis. FS, Wavelet, CS and QU represent the method which each challenger used, i.e. Faraday tomography (Faraday synthesis) with CLEAN, Wavelet based tomography, compressive sampling and model fitting, respectively. Boxes show the first, second (median) and third quartile and the lines represent the maximum and minimum values. The gray shaded area represents the theoretical 1σ error range of median.

They found clear trends. All model fitting methods provide $\chi^2_r \sim 1$ and all the other methods provide significantly larger χ^2_r. The authors concluded that non model fitting methods reconstructed several Faraday components, but they just produce just the brightest 1 or 2 components. That seems to cause large χ^2_r. Somewhat, the model fitting method can reach consistent with theoretical values in terms of $|\mathrm{RM_{wtd}}(\mathrm{est.} - \mathrm{model})|$ and $|\Delta\phi(\mathrm{est.} - \mathrm{model})|$, relatively.

A.4.3 Different models

Here, we review the discussion for results of each type of FDF models. For the case of single Faraday thin source model, most of the algorithms can reconstruct the model very well. Therefore, we do not mention about this case in detail.

The results of cases for two Faraday thin source and thick source are shown in Figure A.7. We just focus on the second figure of merit, $\Delta\phi$, in order to see whether model can be correctly reconstructed. The left and right panel represent the second figure of merit versus model $\Delta\phi$ for the case of two Faraday thin sources and a thick source, respectively.

For the case of two Faraday thin sources model, results completely depend on the situation. In particular, in the case of $\Delta\phi$ much less than FWHM, all methods including model fitting could not indicate existence of two sources (larger than 100% error in Figure. A.7). This should be a limit by bandwidth. At larger $\Delta\phi$ but still less than FWHM, model fitting is able to identify the existence of two sources, although they separate smaller than resolution. At $\Delta\phi$ larger than FWHM, other methods can recognize the two sources, but they still provide large error.

We move to the case of a Faraday thick source. For the case of $\Delta\phi = 25$ rad m^{-2}, all methods could not succeed to recognize the Faraday thick source. Since it is much smaller than FWHM, the source can be seen like a point source. For the case of $\Delta\phi = 50$ rad m^{-2}, on the other hand, some of methods are able to identify the thick source, but estimation of $\Delta\phi$ is not adequate.

A.4.4 Summary of performance

Here, we just summarize the what we understood from this benchmark. This benchmark shows that most algorithms can be successful just when FDF is a single Faraday thin source. However, two sources can be found occasionally. For the case of two Faraday thin sources, only model fitting method succeeds to indicate the existence of two sources, even separation between two sources are smaller than the FWHM. Also, only model fitting

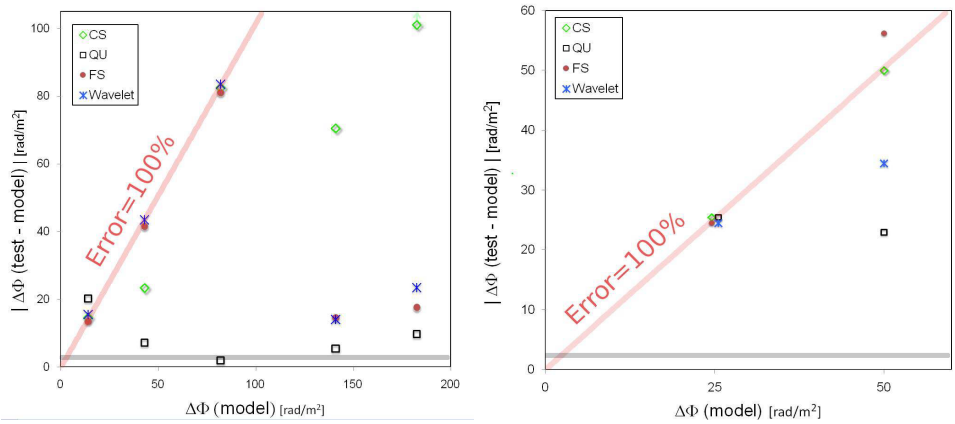

Figure A.7: Second figure of merit, $\Delta\phi$, of the case with two Faraday thin sources (left) and single Faraday thick source (right) (Fig. 4 and 5 of X. H. Sun et al. 2014 [99]).

can provide estimation error which is approximately consistent with theoretical prediction. Furthermore, no methods proposed by now are able to reconstruct Faraday thick source well, even though Faraday thickness is smaller than maximum Faraday thickness determined by minimum observable wavelength.

According to the observation of galaxies, e.g. Ref. [100, 101], a large majority shows depolarization behavior. This fact indicates that Faraday thick source is common on real sky. Furthermore, the FDF calculated from simulation of our Galaxy contains random turbulent magnetic fields which produce the complex Faraday thick source which could not be written by simple function like top-hat or Gaussian (as we mentioned at Chapter 6). That means that the model fitting can not be applied to such FDFs anymore. Therefore, development of algorithms or new ideas for reproducing Faraday thick source are required.

Bibliography

[1] G. Hinshaw, D. Larson, E. Komatsu, D. N. Spergel, C. L. Bennett, J. Dunkley, M. R. Nolta, M. Halpern, R. S. Hill, N. Odegard, L. Page, K. M. Smith, J. L. Weiland, B. Gold, N. Jarosik, A. Kogut, M. Limon, S. S. Meyer, G. S. Tucker, E. Wollack, and E. L. Wright. Nine-year Wilkinson Microwave Anisotropy Probe (WMAP) Observations: Cosmological Parameter Results. *APJS*, 208:19, October 2013.

[2] Planck Collaboration, P. A. R. Ade, N. Aghanim, C. Armitage-Caplan, M. Arnaud, M. Ashdown, F. Atrio-Barandela, J. Aumont, C. Baccigalupi, A. J. Banday, and et al. Planck 2013 results. XVI. Cosmological parameters. *A&A*, 571:A16, November 2014.

[3] V. Springel, C. S. Frenk, and S. D. M. White. The large-scale structure of the Universe. *NATURE*, 440:1137–1144, April 2006.

[4] L. Biermann. Über den Ursprung der Magnetfelder auf Sternen und im interstellaren Raum (miteinem Anhang von A. Schlüter). *Zeitschrift Naturforschung Teil A*, 5:65, 1950.

[5] O. D. Miranda, M. Opher, and R. Opher. Seed magnetic Fields Generated by Primordial Supernova Explosions. *MNRAS*, 301:547–550, December 1998.

[6] H. Hanayama, K. Takahashi, K. Kotake, M. Oguri, K. Ichiki, and H. Ohno. Biermann Mechanism in Primordial Supernova Remnant and Seed Magnetic Fields. *APJ*, 633:941–945, November 2005.

[7] R. S. de Souza and R. Opher. Origin of 10^{15}-10^{16} G magnetic fields in the central engine of gamma ray bursts. *JCAP*, 2:22, February 2010.

[8] T. F. Laganá, R. S. de Souza, and G. R. Keller. On the influence of non-thermal pressure on the mass determination of galaxy clusters. *A&A*, 510:A76, February 2010.

[9] P. J. E. Peebles. The Gravitational Instability of the Universe. *APJ*, 147:859, March 1967.

[10] M. J. Rees and M. Reinhardt. Some Remarks on Intergalactic Magnetic Fields. *A&A*, 19:189, July 1972.

[11] I. Wasserman. On the origins of galaxies, galactic angular momenta, and galactic magnetic fields. *APJ*, 224:337–343, September 1978.

[12] K. Ichiki, K. Takahashi, H. Ohno, H. Hanayama, and N. Sugiyama. Cosmological Magnetic Field: A Fossil of Density Perturbations in the Early Universe. *Science*, 311:827–829, February 2006.

[13] K. Takahashi, K. Ichiki, H. Ohno, H. Hanayama, and N. Sugiyama. Magnetic field generation from cosmological perturbations. *Astronomische Nachrichten*, 327:410, June 2006.

[14] S. Maeda, S. Kitagawa, T. Kobayashi, and T. Shiromizu. Primordial magnetic fields from second-order cosmological perturbations: tight coupling approximation. *Classical and Quantum Gravity*, 26(13):135014, July 2009.

[15] H. Tashiro and N. Sugiyama. Early reionization with primordial magnetic fields. *MNRAS*, 368:965–970, May 2006.

[16] L. F. S. Rodrigues, R. S. de Souza, and R. Opher. Suppression of small baryonic structures due to a primordial magnetic field. *MNRAS*, 406:482–485, July 2010.

[17] F. Govoni and L. Feretti. Magnetic Fields in Clusters of Galaxies. *International Journal of Modern Physics D*, 13:1549–1594, 2004.

[18] C. L. Carilli and G. B. Taylor. Cluster Magnetic Fields. *ARA&A*, 40:319–348, 2002.

[19] M. I. Large, D. S. Mathewson, and C. G. T. Haslam. A High-Resolution Survey of the Coma Cluster of Galaxies at 408 Mc./s. *NATURE*, 183:1663–1664, June 1959.

[20] M. A. G. Willson. Radio observations of the cluster of galaxies in Coma Berenices - the 5C4 survey. *NMRAS*, 151:1–44, 1970.

[21] J. J. Condon, W. D. Cotton, E. W. Greisen, Q. F. Yin, R. A. Perley, G. B. Taylor, and J. J. Broderick. The NRAO VLA Sky Survey. *AJ*, 115:1693–1716, May 1998.

[22] J. C. Kempner and C. L. Sarazin. Radio Halo and Relic Candidates from the Westerbork Northern Sky Survey. *APJ*, 548:639–651, February 2001.

[23] D. Guidetti, M. Murgia, F. Govoni, P. Parma, L. Gregorini, H. R. de Ruiter, R. A. Cameron, and R. Fanti. The intracluster magnetic field power spectrum in Abell 2382. *A&A*, 483:699–713, June 2008.

[24] A. Bonafede, L. Feretti, M. Murgia, F. Govoni, G. Giovannini, D. Dallacasa, K. Dolag, and G. B. Taylor. The Coma cluster magnetic field from Faraday rotation measures. *A&A*, 513:A30, April 2010.

[25] A. H. Bridle and E. B. Fomalont. Complex radio emission from the X-ray cluster Abell 2256. *A&A*, 52:107–113, October 1976.

[26] B. Ballarati, L. Feretti, A. Ficarra, G. Giovannini, M. Nanni, M. C. Olori, and G. Gavazzi. 408 MHz observations of clusters of galaxies. I - Halo sources in the Coma-A 1367 supercluster. *A&A*, 100:323–325, July 1981.

[27] G. Giovannini, L. Feretti, and C. Stanghellini. The Coma cluster radio source 1253 + 275, revisited. *A&A*, 252:528–537, December 1991.

[28] H. Rottgering, I. Snellen, G. Miley, J. P. de Jong, R. J. Hanisch, and R. Perley. VLA observations of the rich X-ray cluster Abell 2256. *APJ*, 436:654–668, December 1994.

[29] T. A. Enßlin, R. Lieu, and P. L. Biermann. Non-thermal origin of the EUV and HEX excess emission of the Coma cluster - the nature of the energetic electrons. *A&A*, 344:409–420, April 1999.

[30] K. Roettiger, J. O. Burns, and J. M. Stone. A Cluster Merger and the Origin of the Extended Radio Emission in Abell 3667. *APJ*, 518:603–612, June 1999.

[31] T. A. Enßlin and Gopal-Krishna. Reviving fossil radio plasma in clusters of galaxies by adiabatic compression in environmental shock waves. *A&A*, 366:26–34, January 2001.

[32] K.-T. Kim, P. P. Kronberg, G. Giovannini, and T. Venturi. Discovery of intergalactic radio emission in the Coma-A1367 supercluster. *NATURE*, 341:720–723, October 1989.

[33] E. Carretti, S. Brown, L. Staveley-Smith, J. M. Malarecki, G. Bernardi, B. M. Gaensler, M. Haverkorn, M. J. Kesteven, and S. Poppi. Detection of a radio bridge in Abell 3667. *MNRAS*, 430:1414–1422, April 2013.

[34] E. Waxman and J. Miralda-Escude. Images of Bursting Sources of High-Energy Cosmic Rays: Effects of Magnetic Fields. *APJL*, 472:L89, December 1996.

[35] J. Aleksić, L. A. Antonelli, P. Antoranz, M. Backes, C. Baixeras, J. A. Barrio, D. Bastieri, J. Becerra González, W. Bednarek, A. Berdyugin, K. Berger, E. Bernardini, A. Biland, O. Blanch, R. K. Bock, G. Bonnoli, P. Bordas, D. Borla Tridon, V. Bosch-Ramon, D. Bose, I. Braun, T. Bretz, D. Britzger, M. Camara, E. Carmona, A. Carosi, P. Colin, S. Commichau, J. L. Contreras, J. Cortina, M. T. Costado, S. Covino, F. Dazzi, A. de Angelis, E. de Cea Del Pozo, R. de Los Reyes, B. de Lotto, M. de Maria, F. de Sabata, C. Delgado Mendez, M. Doert, A. Domínguez, D. Dominis Prester, D. Dorner, M. Doro, D. Elsaesser, M. Errando, D. Ferenc, M. V. Fonseca, L. Font, R. J. García López, M. Garczarczyk, M. Gaug, N. Godinovic, D. Hadasch, A. Herrero, D. Hildebrand, D. Höhne-Mönch, J. Hose, D. Hrupec, C. C. Hsu, T. Jogler, S. Klepser, T. Krähenbühl, D. Kranich, A. La Barbera,

A. Laille, E. Leonardo, E. Lindfors, S. Lombardi, F. Longo, M. López, E. Lorenz, P. Majumdar, G. Maneva, N. Mankuzhiyil, K. Mannheim, L. Maraschi, M. Mariotti, M. Martínez, D. Mazin, M. Meucci, J. M. Miranda, R. Mirzoyan, H. Miyamoto, J. Moldón, M. Moles, A. Moralejo, D. Nieto, K. Nilsson, J. Ninkovic, R. Orito, I. Oya, S. Paiano, R. Paoletti, J. M. Paredes, S. Partini, M. Pasanen, D. Pascoli, F. Pauss, R. G. Pegna, M. A. Perez-Torres, M. Persic, L. Peruzzo, F. Prada, E. Prandini, N. Puchades, I. Puljak, I. Reichardt, W. Rhode, M. Ribó, J. Rico, M. Rissi, S. Rügamer, A. Saggion, T. Y. Saito, M. Salvati, M. Sánchez-Conde, K. Satalecka, V. Scalzotto, V. Scapin, C. Schultz, T. Schweizer, M. Shayduk, S. N. Shore, A. Sierpowska-Bartosik, A. Sillanpää, J. Sitarek, D. Sobczynska, F. Spanier, S. Spiro, A. Stamerra, B. Steinke, J. C. Struebig, T. Suric, L. Takalo, F. Tavecchio, P. Temnikov, T. Terzic, D. Tescaro, M. Teshima, D. F. Torres, H. Vankov, R. M. Wagner, Q. Weitzel, V. Zabalza, F. Zandanel, R. Zanin, A. Neronov, and D. V. Semikoz. Search for an extended VHE γ-ray emission from Mrk 421 and Mrk 501 with the MAGIC Telescope. *A&A*, 524:A77, December 2010.

[36] A. Neronov and I. Vovk. Evidence for Strong Extragalactic Magnetic Fields from Fermi Observations of TeV Blazars. *Science*, 328:73–, April 2010.

[37] K. Takahashi, K. Murase, K. Ichiki, S. Inoue, and S. Nagataki. Detectability of Pair Echoes from Gamma-Ray Bursts and Intergalactic Magnetic Fields. *APJL*, 687:L5–L8, November 2008.

[38] C. D. Dermer, M. Cavadini, S. Razzaque, J. D. Finke, J. Chiang, and B. Lott. Time Delay of Cascade Radiation for TeV Blazars and the Measurement of the Intergalactic Magnetic Field. *APJL*, 733:L21, June 2011.

[39] K. Takahashi, M. Mori, K. Ichiki, S. Inoue, and H. Takami. Lower Bounds on Magnetic Fields in Intergalactic Voids from Long-term GeV-TeV Light Curves of the Blazar Mrk 421. *APJL*, 771:L42, July 2013.

[40] K. Takahashi, M. Mori, K. Ichiki, and S. Inoue. Lower Bounds on Intergalactic Magnetic Fields from Simultaneously Observed GeV-TeV Light Curves of the Blazar Mrk 501. *APJL*, 744:L7, January 2012.

[41] H. J. Völk and A. M. Atoyan. Clusters of galaxies: magnetic fields and nonthermal emission. *Astroparticle Physics*, 11:73–82, June 1999.

[42] P. P. Kronberg, Q. W. Dufton, H. Li, and S. A. Colgate. Magnetic Energy of the Intergalactic Medium from Galactic Black Holes. *APJ*, 560:178–186, October 2001.

[43] K. Subramanian, A. Shukurov, and N. E. L. Haugen. Evolving turbulence and magnetic fields in galaxy clusters. *MNRAS*, 366:1437–1454, March 2006.

[44] D. Ryu, H. Kang, J. Cho, and S. Das. Turbulence and Magnetic Fields in the Large-Scale Structure of the Universe. *Science*, 320:909–, May 2008.

[45] D. Ryu, H. Kang, E. Hallman, and T. W. Jones. Cosmological Shock Waves and Their Role in the Large-Scale Structure of the Universe. *APJ*, 593:599–610, August 2003.

[46] M. S. Madsen. Magnetic fields in cosmology. *MNRAS*, 237:109–117, March 1989.

[47] J. D. Barrow, P. G. Ferreira, and J. Silk. Constraints on a Primordial Magnetic Field. *Physical Review Letters*, 78:3610–3613, May 1997.

[48] R. F. O'Connell and J. J. Matese. Effect of a Constant Magnetic Field on the Neutron Beta Decay Rate and its Astrophysical Implications. *NATURE*, 222:649–650, May 1969.

[49] P. J. Kernan, G. D. Starkman, and T. Vachaspati. Big bang nucleosynthesis constraints on primordial magnetic fields. *PRD*, 54:7207–7214, December 1996.

[50] G. Greenstein. Primordial Helium Production in "Magnetic" Cosmologies. *NATURE*, 223:938–939, August 1969.

[51] Y. Sofue, M. Fujimoto, and K. Kawabata. Faraday Rotation by Metagalactic Magnetic Field. *PASJ*, 20:388, 1968.

[52] K. Brecher and G. R. Blumenthal. On the Origin of Cosmic Magnetic Fields. *APL*, 6:169, July 1970.

[53] P. P. Kronberg and M. Simard-Normandin. New evidence on the origin of rotation measures in extragalactic radio sources. *NATURE*, 263:653–656, October 1976.

[54] J. P. Vallee. Detecting the largest magnets - The universe and the clusters of galaxies. *APJ*, 360:1–6, September 1990.

[55] R. Beck and B. M. Gaensler. Observations of magnetic fields in the Milky Way and in nearby galaxies with a Square Kilometre Array. *New Astronomy Reviews*, 48:1289–1304, December 2004.

[56] A. M. Hopkins, J. Afonso, B. Chan, L. E. Cram, A. Georgakakis, and B. Mobasher. The Phoenix Deep Survey: The 1.4 GHz Microjansky Catalog. *Astronomical Journal*, 125:465–477, February 2003.

[57] A. R. Taylor, J. M. Stil, and C. Sunstrum. A Rotation Measure Image of the Sky. *APJ*, 702:1230–1236, September 2009.

[58] L. Rudnick and F. N. Owen. The Distribution of Polarized Radio Sources >15 μJy in GOODS-N. *APJ*, 785:45, April 2014.

[59] K. Kumazaki, T. Akahori, S. Ideguchi, T. Kurayama, and K. Takahashi. Properties of intrinsic polarization angle ambiguities in Faraday tomography. *PASJ*, 66:61, June 2014.

[60] T. Akahori, K. Kumazaki, K. Takahashi, and D. Ryu. Exploring the intergalactic magnetic field by means of Faraday tomography. *PASJ*, 66:65, June 2014.

[61] S. Ideguchi, K. Takahashi, T. Akahori, K. Kumazaki, and D. Ryu. Fisher analysis on wide-band polarimetry for probing the intergalactic magnetic field. *PASJ*, 66:5, February 2014.

[62] K. C. Westfold. The Polarization of Synchrotron Radiation. *APJ*, 130:241, July 1959.

[63] R. J. Rand and A. G. Lyne. New Rotation Measures of Distant Pulsars in the Inner Galaxy and Magnetic Field Reversals. *MNRAS*, 268:497, May 1994.

[64] M. A. Brentjens and A. G. de Bruyn. Faraday rotation measure synthesis. *A&A*, 441:1217–1228, October 2005.

[65] S. P. O'Sullivan, S. Brown, T. Robishaw, D. H. F. M. Schnitzeler, N. M. McClure-Griffiths, I. J. Feain, A. R. Taylor, B. M. Gaensler, T. L. Landecker, L. Harvey-Smith, and E. Carretti. Complex Faraday depth structure of active galactic nuclei as revealed by broad-band radio polarimetry. *MNRAS*, 421:3300–3315, April 2012.

[66] B. J. Burn. On the depolarization of discrete radio sources by Faraday dispersion. *MNRAS*, 133:67, 1966.

[67] S. P. O'Sullivan, N. M. McClure-Griffiths, I. J. Feain, B. M. Gaensler, and R. J. Sault. Broad-band radio circular polarization spectrum of the relativistic jet in PKS B2126-158. *MNRAS*, 435:311–319, October 2013.

[68] D. Farnsworth, L. Rudnick, and S. Brown. Integrated Polarization of Sources at $\lambda \tilde{} 1$ m and New Rotation Measure Ambiguities. *The Astronomical Journal*, 141:191, June 2011.

[69] D. D. Sokoloff, A. A. Bykov, A. Shukurov, E. M. Berkhuijsen, R. Beck, and A. D. Poezd. Depolarization and Faraday effects in galaxies. *MNRAS*, 299:189–206, August 1998.

[70] G. Heald. The Faraday rotation measure synthesis technique. In K. G. Strassmeier, A. G. Kosovichev, and J. E. Beckman, editors, *IAU Symposium*, volume 259 of *IAU Symposium*, pages 591–602, April 2009.

[71] J. A. Högbom. Aperture Synthesis with a Non-Regular Distribution of Interferometer Baselines. *A&A*, 15:417, June 1974.

[72] M. L. Bernet, F. Miniati, and S. J. Lilly. The Interpretation of Rotation Measures in the Presence of Inhomogeneous Foreground Screens. *APJ*, 761:144, December 2012.

[73] A. M. Hammond, T. Robishaw, and B. M. Gaensler. A New Catalog of Faraday Rotation Measures and Redshifts for Extragalactic Radio Sources. *ArXiv e-prints*, September 2012.

[74] T. Akahori and D. Ryu. Faraday Rotation Measure Due to the Intergalactic Magnetic Field. *APJ*, 723:476–481, November 2010.

[75] T. Akahori and D. Ryu. Faraday Rotation Measure due to the Intergalactic Magnetic Field. II. The Cosmological Contribution. *APJ*, 738:134, September 2011.

[76] B. Gold, N. Odegard, J. L. Weiland, R. S. Hill, A. Kogut, C. L. Bennett, G. Hinshaw, X. Chen, J. Dunkley, M. Halpern, N. Jarosik, E. Komatsu, D. Larson, M. Limon, S. S. Meyer, M. R. Nolta, L. Page, K. M. Smith, D. N. Spergel, G. S. Tucker, E. Wollack, and E. L. Wright. Seven-year Wilkinson Microwave Anisotropy Probe (WMAP) Observations: Galactic Foreground Emission. *APJS*, 192:15, February 2011.

[77] T. Akahori, D. Ryu, J. Kim, and B. M. Gaensler. Simulated Faraday Rotation Measures toward High Galactic Latitudes. *APJ*, 767:150, April 2013.

[78] M. Haverkorn, B. M. Gaensler, J. C. Brown, N. S. Bizunok, N. M. McClure-Griffiths, J. M. Dickey, and A. J. Green. Enhanced Small-Scale Faraday Rotation in the Galactic Spiral Arms. *APJL*, 637:L33–L35, January 2006.

[79] M. Haverkorn, J. C. Brown, B. M. Gaensler, and N. M. McClure-Griffiths. The Outer Scale of Turbulence in the Magnetoionized Galactic Interstellar Medium. *APJ*, 680:362–370, June 2008.

[80] S. Ananthakrishnan. The giant meterwave radio telescope. *JApAS*, 16:427, 1995.

[81] D. G. Steer, P. E. Dewdney, and M. R. Ito. Enhancements to the deconvolution algorithm 'CLEAN'. *A&A*, 137:159–165, August 1984.

[82] B. P. Wakker and U. J. Schwarz. The Multi-Resolution CLEAN and its application to the short-spacing problem in interferometry. *A&A*, 200:312–322, July 1988.

[83] S. Ideguchi, Y. Tashiro, T. Akahori, K. Takahashi, and D. Ryu. Faraday Dispersion Functions of Galaxies. *The Astrophysical Journal*, 792:51, September 2014.

[84] J. M. Cordes and T. J. W. Lazio. NE2001.I. A New Model for the Galactic Distribution of Free Electrons and its Fluctuations. *ArXiv Astrophysics e-prints*, July 2002.

[85] J. M. Cordes and T. J. W. Lazio. NE2001. II. Using Radio Propagation Data to Construct a Model for the Galactic Distribution of Free Electrons. *ArXiv Astrophysics e-prints*, January 2003.

[86] X. H. Sun, W. Reich, A. Waelkens, and T. A. Enßlin. Radio observational constraints on Galactic 3D-emission models. *A&A*, 477:573–592, January 2008.

[87] G. Giacinti, M. Kachelrieß, D. V. Semikoz, and G. Sigl. Ultrahigh energy nuclei in the galactic magnetic field. *JCAP*, 8:36, August 2010.

[88] J. Kim, D. Ryu, T. W. Jones, and S. S. Hong. A Multidimensional Code for Isothermal Magnetohydrodynamic Flows in Astrophysics. *APJ*, 514:506–519, March 1999.

[89] M. Machida, K. E. Nakamura, T. Kudoh, T. Akahori, Y. Sofue, and R. Matsumoto. Dynamo Activities Driven by Magnetorotational Instability and the Parker Instability in Galactic Gaseous Disks. *APJ*, 764:81, February 2013.

[90] E. J. Candes and M. B. Wakin. An Introduction To Compressive Sampling. *IEEE Signal Processing Magazine*, 25:21–30, March 2008.

[91] F. Li, T. J. Cornwell, and F. de Hoog. The application of compressive sampling to radio astronomy. I. Deconvolution. *A&A*, 528:A31, April 2011.

[92] F. Li, S. Brown, T. J. Cornwell, and F. de Hoog. The application of compressive sampling to radio astronomy. II. Faraday rotation measure synthesis. *A&A*, 531:A126, July 2011.

[93] E. Candes and T. Tao. Decoding by Linear Programming. *ArXiv Mathematics e-prints*, February 2005.

[94] I. Daubechies, editor. *Ten lectures on wavelets*, 1992.

[95] Amir Beck and Marc Teboulle. A fast iterative shrinkage-thresholding algorithm for linear inverse problems. *SIAM J. Img. Sci.*, 2(1):183–202, March 2009.

[96] P. Frick, D. Sokoloff, R. Stepanov, and R. Beck. Wavelet-based Faraday rotation measure synthesis. *MNRAS*, 401:L24–L28, January 2010.

[97] M. Andrecut. MUSIC for Faraday rotation measure synthesis. *MNRAS*, 430:L15–L19, March 2013.

[98] M. Cheney. The linear sampling method and the MUSIC algorithm. *Inverse Problems*, 17:591–595, August 2001.

[99] X. H. Sun, L. Rudnick, T. Akahori, C. S. Anderson, M. R. Bell, J. D. Bray, J. S. Farnes, S. Ideguchi, K. Kumazaki, T. O'Brien, S. P. O'Sullivan, A. M. M. Scaife, R. Stepanov, J. Stil, K. Takahashi, R. J. van Weeren, and M. Wolleben. Comparison of algorithms for determination of rotation measure and Faraday structure I. 1100 - 1400 MHz. *ArXiv e-prints*, September 2014.

[100] C. J. Law, B. M. Gaensler, G. C. Bower, D. C. Backer, A. Bauermeister, S. Croft, R. Forster, C. Gutierrez-Kraybill, L. Harvey-Smith, C. Heiles, C. Hull, G. Keating, D. MacMahon, D. Whysong, P. K. G. Williams, and M. Wright. Spectropolarimetry with the Allen Telescope Array: Faraday Rotation Toward Bright Polarized Radio Galaxies. *APJ*, 728:57, February 2011.

[101] J. S. Farnes, B. M. Gaensler, and E. Carretti. A Broadband Polarization Catalog of Extragalactic Radio Sources. *APJS*, 212:15, May 2014.